On Sea Level - Ice Sheet Interactions

On Sea Level - Ice Sheet Interactions

A dissertation presented

by

Natalya Alissa Gomez

to

The Department of Earth and Planetary Sciences

in partial fulfillment of the requirements

for the degree of

Doctor of Philosophy

in the subject of

Earth and Planetary Sciences

Harvard University

Cambridge, Massachusetts

November 2013

Dissertation Advisor: Professor Jerry X. Mitrovica Natalya Alissa Gomez

On Sea Level - Ice Sheet Interactions

Abstract

This thesis focuses on the physics of static sea-level changes following variations in the distribution of grounded ice and the influence of these changes on the stability and dynamics of marine ice sheets. Gravitational, deformational and rotational effects associated with changes in grounded ice mass lead to markedly non-uniform spatial patterns of sea-level change. I outline a revised theory for computing post-glacial sea-level predictions and discuss the dominant physical effects that contribute to the patterns of sea-level change associated with surface loading on different timescales. I show, in particular, that a large sea-level fall (rise) occurs in the vicinity of a retreating (advancing) ice sheet on both short and long timescales. I also present an application of the sea-level theory in which I predict the sea-level changes associated with a new model of North American ice sheet evolution and consider the implications of the results for efforts to establish the sources of Meltwater Pulse 1A. These results demonstrate that viscous deformational effects can influence the amplitude of sea-level changes observed at far-field sea-level sites, even when the time window being considered is relatively short ($\leq$ 500 years).

Subsequently, I investigate the feedback of sea-level changes on marine ice-sheet stability and dynamics by coupling a global sea-level model to ice-sheet models of increasing complexity. To begin, I incorporate gravitationally self-consistent sea-level changes into an equilibrium marine ice-sheet stability theory to show that the sea-level changes have a stabilizing influence on ice-sheet retreat. Next, I consider the impact of the stabilizing mechanism on the timescale of ice-sheet retreat using a 1D dynamic coupled ice sheet - sea level model. Simulations with the coupled model, which

incorporate viscoelastic deformation of the solid Earth, show that local sea-level changes at the grounding line act to slow, and in some cases, halt grounding-line migration. Finally, I confirm the universality of this conclusion in a more realistic setting by coupling a 3-D, Antarctic Ice Sheet (AIS) model to a global sea-level model and simulating the evolution of the AIS over the last 40,000 years.

Contents

List of Figures

List of Tables

Acknowledgements

I am so grateful to all those who have supported me during my time in graduate school. First, I would like to thank my advisor, Jerry Mitrovica. I feel lucky to have had the support of such an incredible advisor and mentor behind me. Jerry introduced me to the field of geophysics when I first took his "Physics of the Earth" course in an undergraduate physics program at the University of Toronto. Since then, he has continually and generously provided me with more opportunities to learn and develop as a scientist than I could have hoped for. I look forward to continuing to learn from and collaborate with Jerry throughout my academic career.

As a graduate student, I have had the opportunity to collaborate and interact with many great scientists. Thank you to my committee members: Peter Huybers, Rick O'Connell, Sujoy Mukhopadhyay and Miaki Ishii for their helpful guidance. I am particularly grateful for the opportunities I have had to work David Pollard, from whom I have learned so much about ice-sheet modeling, and Peter Huybers, who has provided me with much useful advice and guidance over the years. I am also grateful to Leonard Tsuji, Peter Clark, Mark Tamisiea, Sabine Stanley and Glenn Milne for their encouragement, advice and collaborations.

The Earth and Planetary Sciences Department at Harvard University has a special sense of community and a supportive and interactive atmosphere. I would like to thank Sarah Colgan, Chenoweth Moffat, Paul Kelley, Maryorie Grande, Marisa Reilly and all the others who make the EPS Department run so smoothly and work hard to create such a great atmosphere. Thank

you, also, to all those who help to run the Harvard University Center for the Environment and the Graduate Student Consortium on Energy and the Environment. The Energy Consortium has helped me to expand my horizons, and put my research into a broader, interdisciplinary context.

I am happy that I got to enjoy and struggle through graduate school with such a great group of people. Thank you to everyone in the Mitrovica group - Carling Hay, Erik Chan, Eric Morrow, Jacky Austermann, Harriet Lau, Ken Ferrier, Jade D'Alpoim Guedes, Glenn Sterenborg and John Crowley. Carling, Erik and Eric, I could not have asked for better people to join me in migrating across the border from Canada. Everyone in the group, I feel lucky to be connected to you both as scientists and as friends. Thank you also to all of my fellow graduate students, friends and officemates, including the Mitrovica group, Helen Amos, Eileen Evans, Meredith Langstaff, Archana Dayalu, Rita Parai, Phoebe Robinson, Will Leavitt, Steve Turner, Emmy Smith, Uyanga Bold, Kristian Bergen, Kate Dennis, Sierra Peterson, Lynn McGregor, the PDDD group and everyone else who helped me to make the most of my time in graduate school.

I am also grateful for the support I received from the people in my life outside of graduate school. Thank you to the swing and blues dancing communities for providing me with an artistic, athletic and social outlet. Thank you to Shawn, for giving me confidence, inspiring me to pursue my passions and participating in adventures with me. And thank you to my amazing family, and especially my parents for being endlessly supportive of everything I do, loving me and being there for me.

Finally, I dedicate this thesis to my late granny, Lucy Nina Noel Potts. Her love of learning, determination, intelligence, and sense of adventure were so inspiring to me, and her support and love meant the world to me.

Chapter 1

Introduction

In light of the potential for continued and increased global-scale warming of the climate, there has been an increased focus on constraining the response of present-day ice reservoirs to climate change and their contribution to sea-level rise. The stability of the Antarctic Ice Sheet (AIS), with a volume that accounts for $\sim 90\%$ of all freshwater on the Earth's surface (3×10^{16} m^3, or $\sim$70 meters of equivalent globally averaged sea-level rise), is of particular concern. Much of the West Antarctic Ice Sheet (WAIS) and large sectors of the East Antarctic Ice Sheet (EAIS) are characterized by a marine-based setting, in which the base of the ice lies below the height of the sea surface. These sectors are considered to be potentially susceptible to collapse in a warming climate.

Indeed, rapid collapse of ice shelves as well as thinning, retreat and acceleration of outlet glaciers have recently been observed in marine sectors of Antarctica [e.g. Shepherd, 2001; Thomas, 2004; Rignot, 2006]. The ice-sheet modeling community is working towards understanding what drives these changes and whether or not they evolve into a large-scale collapse of the ice sheet and an associated, global-scale sea-level change. In addition to studying ongoing changes in the AIS, a better understanding of the history of the ice sheet may help to establish whether the recent evolution is within the range of natural variability and the conditions necessary to trigger large-scale collapse. The work in this thesis contributes to improving our understanding of past and

future marine ice-sheet evolution by exploring the physics of the associated sea-level changes and by coupling this physics to progressively more complex ice-sheet models.

We begin by asking the question: What is the geographic variability of sea-level change following future retreat of the AIS? One might intuitively think that meltwater will fill the oceans like a bathtub, raising sea levels everywhere by the same amount. In reality, it is now well-established that a number of physical effects will lead to a pattern of sea-level change characterized by significant geographic variability. In Chapter 2, we summarize the work of Gomez et al. [2010b], which computes the patterns of global sea-level change associated with the possible future collapse of marine-based sectors of the AIS. The chapter outlines a revised theory for sea-level projections that incorporates the gravitational, deformational and rotational effects associated with the changing surface (ice plus ocean) load. The theory allows shorelines to migrate to accommodate the onlap and offlap of water at the edges of continents and the inundation of water into marine-based sectors freed of ice. In addition to presenting the patterns, or "fingerprints", of sea-level rise that would follow the rapid collapse of the WAIS and marine sectors of the EAIS, we decompose the fingerprints into contributions from the various aforementioned physical effects.

In the case of rapid ice-sheet retreat considered in Gomez et al. [2010b] (i.e., retreat on timescales of centuries or less), the Earth deforms elastically and sea-level changes are independent of the ice-sheet history. However, large-scale ice-sheet evolution occurs over millennial timescales or longer, and on these timescales, the Earth deforms viscoelastically with a magnitude and geometry that depends on the full ice distribution history. Furthermore, the patterns of sea-level change that emerge are distinct from those that dominate on short timescales. Chapter 2 ends with a discussion of the physical effects that contribute to sea-level changes on these longer timescales using the results of a suite of illustrative ice-age sea-level simulations presented in Gomez et al. [2013]. The discussion emphasizes, in particular, that at any given time during an ice sheet's evolution, the

total predicted sea-level change will be a combination of a short timescale signal governed by active changes in the ice sheet, and a longer timescale signal associated with the past evolution of the ice sheet.

In Chapter 3, the sea-level theory is applied to investigate an issue related to Meltwater Pulse 1A (mwp-1A), a rapid (< 500 year), ~ 20 meter pulse of sea-level rise that took place at $\sim$14 ka during the Last Deglaciation. mwp-1A has been observed in relative sea-level records at Barbados, Tahiti and Sunda Shelf, however its source or sources are still uncertain [Deschamps et al., 2012]. Some have proposed that the meltwater came from the Laurentide Ice Sheet [e.g. Kennett and Shackleton, 1975; Fairbanks et al., 1992; Peltier, 2004] but an analysis of the sea-level rise observed at far field sites suggests that the AIS was a significant contributor to the event [Clark et al., 2002; Bassett, 2005; Bard et al., 2010]. Recently, Gregoire et al. [2012] modeled the deglacial retreat of ice sheets in the Northern Hemisphere and proposed that the collapse of an ice saddle between the Laurentide and Cordilleran ice sheets could have been a dominant source of mwp-1A. We model the sea-level changes associated with the ice-sheet evolution predicted by Gregoire et al. [2012] to test whether the saddle collapse source is consistent with available sea-level records.

Chapters 2 and 3 focus on the impact that ice sheets have on sea-level change. In the remaining chapters of this thesis, we investigate how sea-level changes feedback into the stability and dynamics of ice sheets. This feedback is active, in particular, in marine settings where ice interacts with the surrounding ocean. Marine ice sheets gain mass through accumulation throughout their interiors and lose mass through flux of ice across the grounding line into floating ice shelves. The grounding line is the location where the ice is just thin enough to float, dividing the grounded ice sheet from the floating ice shelves. The ice loss across the grounding line is very sensitive to the thickness of ice there, which is in turn proportional to the depth of water; a small increase in sea level at the grounding line leads to a large increase in ice loss [Schoof, 2007a].

Marine ice sheets are widely thought to be potentially unstable and prone to runaway retreat when resting upon reversed bed slopes that slope down towards the interior of the ice sheet[Weertman, 1974; Thomas and Bentley, 1978; Schoof, 2007a; Katz and Worster, 2010]. This hypothesis is based on the idea that when the grounding line retreats into deeper water, the ice loss at the grounding line increases, leading to further retreat. Past analyses of this instability mechanism have not accounted for the deformational and gravitational effects described in Chapter 2 that lead to a large sea-level fall (rise) at the margin of a rapidly shrinking (growing) ice sheet. This sea-level fall can act to compensate for some of the deepening of the bed. In Chapter 4, we present work published in Gomez et al. [2010a] in which instantaneous sea-level changes associated with a perturbation in the ice distribution are incorporated into a canonical model of equilibrium ice-sheet stability [Weertman, 1974]. The results demonstrate the potential stabilizing influence of gravitationally self-consistent sea-level changes on marine ice-sheet grounding lines.

To evaluate the impact of sea-level changes on the timescale of retreat of marine ice sheets, we must introduce the dimension of time into the analysis. Gomez et al. [2012] accomplish this by coupling a global sea-level model to a dynamic ice-sheet model. In particular, they employ a one-dimensional flow line ice-sheet model [Pollard and DeConto, 2009, 2012b] with simplified bedrock geometry to highlight the physics of the time-dependent coupling. Whereas the sea-level model in Chapter 4 only incorporated elastic deformation of the solid Earth, Gomez et al. [2012] employ the version of the sea-level theory described in Chapter 2 that includes viscoelastic deformation in order to capture the evolution of the system over longer timescales. As described in Chapter 5, results from the coupled model demonstrate that the sea-level fall associated with a retreating ice sheet acts to slow down and, in some cases, halt ice-sheet retreat down a reversed bed slope.

Finally, in Chapter 6, we extend the work in Gomez et al. [2010a, 2012] by coupling a realistic 3-D ice sheet-shelf model to a gravitationally self-consistent model of post-glacial sea-level change

[Gomez et al., 2013]. We apply the coupled model to simulate the evolution of the AIS through the last 40,000 years, focussing on the deglaciation phase of the ice sheet. Model results confirm the conclusions of Chapters 4 and 5 in a more realistic setting. That is, the feedback of sea-level changes onto ice-sheet dynamics acts to slow down grounding line migration and alter the extent of retreat and advance of the ice sheet relative to simulations in which the full coupling is not incorporated. Predicted sea-level changes associated with the realistic, 3-D ice-sheet model highlight the complex gravitational, deformational, and rotational effects that contribute to post-glacial sea-level change. The model results are shown to compare well to relative sea-level histories and GPS-derived present-day uplift rates around Antarctica.

Chapter 2

Static Sea-Level Changes: Theory and Modeling

In this Chapter, we present gravitationally self-consistent predictions of sea-level change following past and future retreat of sectors of the Antarctic Ice Sheet (AIS). Our predictions are based on a state-of-the-art pseudo-spectral sea-level algorithm that incorporates deformational, gravitational and rotational effects on sea level, as well as the migration of shorelines due to both local sea-level variations and changes in the extent of marine-based ice cover. We focus first on the future sea-level changes that would occur following the rapid disappearance of either the West Antarctic Ice Sheet (WAIS) or marine sectors of the East Antarctic Ice Sheet (EAIS). If we define the effective eustatic value (EEV) as the geographically uniform rise in sea level once all exposed marine-based sectors have been filled with water, then we find that some locations can experience a sea-level rise that is $\sim 40\%$ higher than the EEV. This enhancement is due to the migration of water away from the zone of melting in response to the loss of gravitational attraction toward the ice sheet (load self-attraction), the expulsion of water from marine areas as these regions rebound due to the unloading, and the feedback into sea level of a contemporaneous perturbation in Earth rotation. In the WAIS case, this peak enhancement is twice the value predicted in a previous projection that did not include expulsion of water from exposed marine-sectors of the West Antarctic or rotational

Portions of this chapter were published in a paper titled "A New Projection of Sea-Level Change in Response to a Collapse of the Antarctic Ice Sheet" with Jerry X. Mitrovica, Mark E. Tamisiea and Peter U. Clark in Geophysical Journal International, vol. 180, 623-634, 2010.

feedback. The peak enhancements occur over the coasts of the U.S. and in the Indian Ocean in the WAIS melt scenario, and over the south Atlantic and northwest Pacific in the EAIS scenario. We conclude that accurate projections of the sea-level hazard associated with ongoing global warming should be based on a theory that includes the complete suite of physical processes described above.

In later chapters of this thesis (3, 5 and 6), we focus on AIS evolution over longer timescales and in this case, the dominant physical effects contributing to sea-level changes differ from those that govern rapid changes (<500 year) in ice distribution. Therefore, the material in this chapter is augmented, relative to Gomez et al. [2010b], to include a discussion of ice-age sea-level physics using, as an illustrative example, predictions of post-glacial sea level following past AIS retreat.

2.1 Introduction to Future Sea-Level Predictions

As the Earth moves into a period of continued and potentially increased global-scale warming, questions regarding the stability of present-day ice reservoirs, including the polar ice caps and mountain glaciers, have become more pressing. The Antarctic Ice Sheet (AIS) is a central focus of this interest, particularly because a large fraction rests on bedrock below sea level (Figure 2.1). In this regard, most discussions of future instability are preoccupied with the possible collapse of the West Antarctic Ice Sheet (WAIS), which is separated from the East Antarctic Ice Sheet (EAIS) by the Transantarctic Mountains and the Ronne-Flichner Ice Shelf, and which is almost entirely characterized by a marine-based setting. However, large sectors of the EAIS, particularly in Wilkes Land ($\sim 120 - 150^\circ$ E) and in the vicinity of the Amery Ice Shelf and Lambert Glacier ($\sim 70^\circ$ E), have a base that also lies well below local sea level (Figure 2.1) and the impact on sea level of their destabilization has not been previously addressed.

What would the change in sea level be as a consequence to the collapse of these marine-based sectors of the AIS? The answer to this question has not yet been fully explored, and values that are

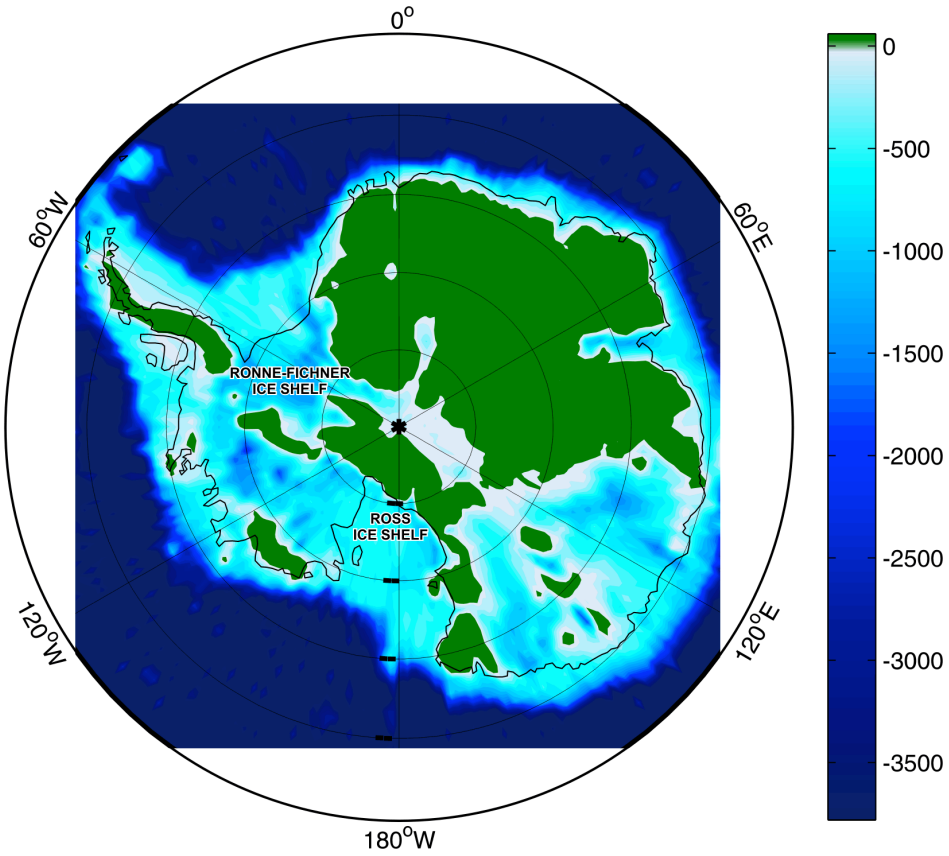

Figure 2.1: Map showing bedrock topography over the Antarctic and vicinity. Color contours are only shown over locations where this topography is less than zero in order to highlight the extent of marine-based settings. The black line shows the edge of the grounded ice sheet.

quoted within the literature - both mainstream and scientific - can vary widely depending on the level of scientific sophistication used to generate the estimate. For example, if one were to convert the grounded portion of the volume cited above into a volume of water, and then distribute this volume in a geographically uniform manner throughout the global oceans, then one would arrive at the so-called eustatic estimate of ~ 70 m. If, however, one were to take into account the negative topography of the bedrock, which would serve as accommodation space for meltwater, then the geographically uniform increase in sea level, which we will term the effective eustatic value (EEV), would be closer to $55 - 60$ m. In regard to the WAIS, the analogous eustatic and EEV are ~ 8 and ~ 5 m, respectively. The latter is a widely cited estimate [Mercer, 1978], and it is quoted, for example, in Chapter 10 of the penultimate assessment of the IPCC [Solomon et al., 2007].

However, it has been known for well over a century [Woodward, 1888] that a rapidly melting ice sheet will produce a markedly non-uniform change in sea level. This spatial variability is largely driven by the self-attraction of the surface mass (ice plus ocean) load. Specifically, an ice sheet exerts a gravitational (tidal) attraction on the surrounding ocean, which leads to a build-up of water close to the ice mass. As the ice sheet melts, the integrated mass of the oceans will certainly increase; however, the tidal attraction will decrease, leading to a migration away from the zone of melting. Woodward [1888] showed, using a simple rigid (i.e., non-deforming) Earth model, that the migration process will dominate within a region 2000 km from the ice sheet. In this "near-field" zone, sea level will fall in response to the melting event, while it will rise by progressively larger values at greater distance. The predicted migration of water is accentuated in more recent studies, which include elastic deformation of the solid surface, since the near-field of the ice sheet will also be subject to crustal uplift which adds to the local sea-level fall [Farrell and Clark, 1976; Clark and Primus, 1987; Nakiboglu and Lambeck, 1991; Conrad and Hager, 1997; Mitrovica et al., 2001; Tamisiea et al., 2001]

Since load self-attraction contributes significantly to the geographic variability, changes in the mass balance of a specific ice reservoir will produce a distinct pattern of sea-level change. Hence these patterns have come to be known as sea-level "fingerprints" [Plag and Juettner, 2001]. Mitrovica et al. [2001] showed that the geographic variation in secular trends evident in a widely distributed subset of 20th century tide gauge records can be explained by a weighted sum of fingerprints from melting of polar ice sheets and mountain glaciers. Their analysis, which demonstrated that such records could be used to constrain not only the amplitude of recent sea-level rise but also the relative contributions from various sources, has motivated renewed interest in the physics of sea-level change following rapid melting events. This interest has been further broadened by efforts to infer the source of sea-level changes that have accompanied late Quaternary, ice-age climate events [Clark et al., 2002; Kendall et al., 2008].

Many of these recent studies have calculated sea-level fingerprints associated with melting from the AIS or a sub-region, including the WAIS [Mitrovica et al., 2001; Tamisiea et al., 2001; Clark et al., 2002]. However, to our knowledge, the first fingerprint of this kind was computed by Clark and Lingle [1977] who considered the impact of a future, uniform thinning of the WAIS on sea level. We reproduce their result in Figure 2.2. The contours, as in the original publication, are normalized by the eustatic sea-level change associated with the melting event.

As discussed above, melting from the WAIS leads to a sea-level fall in the vicinity of this region, and an increase in the computed sea-level rise as one moves toward the north. The mean sea-level change is, of course, equal to 1, or the eustatic value. The maximum sea-level rise is 20% higher than the eustatic value in the north Atlantic and Indian Ocean and 26% higher in the north Pacific. The pattern of sea-level rise tends to taper toward the continental shelves, so that coastal sites experience a rise $\sim$10% higher than the eustatic value. The broad scale pattern of water migration away from the WAIS is largely due, as we have discussed, to load self-attraction, while the tapering

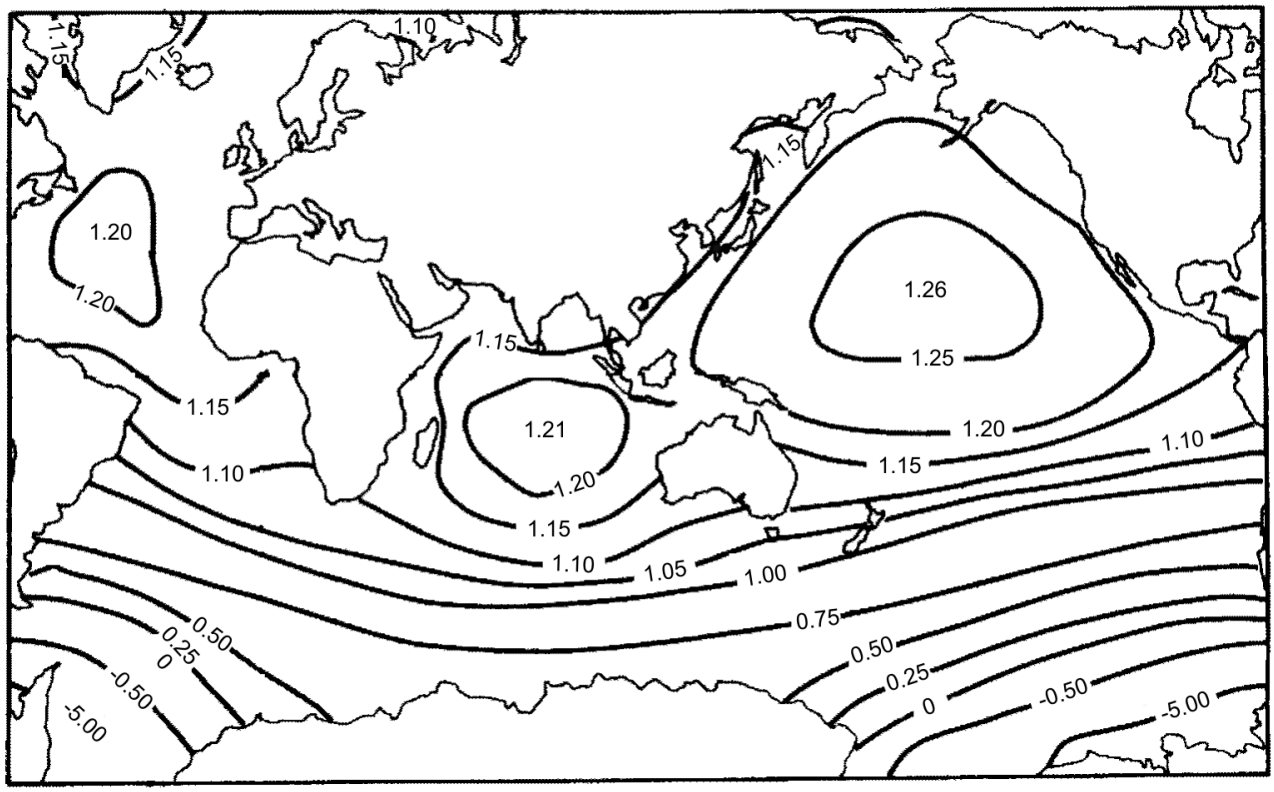

Figure 2.2: Sea-level change, normalized by the eustatic equivalent sea-level rise, in response to a uniform thinning of the West Antarctic ice sheet; the figure is reproduced, with minor modification, from Clark and Lingle [1977]. As described in the text, Clark and Lingle [1977] applied a standard sea-level theory valid for a non-rotating Earth in which all shorelines remain fixed with time. Thus, the prediction does not include inundation into the West Antarctic or perturbations in sea level associated with changes in the Earth's rotation vector.

pattern over the northern oceans is due to loading effects. Specifically, the ocean load will tend to (elastically) deform the crust of the elastic Earth model downwards in the middle of the ocean and upwards over the (unloaded) continental regions.

Clark and Lingle [1977] argued that their calculation (Figure 2.2) could be scaled to consider any uniform melting (or indeed growth) of the WAIS by multiplying the normalized prediction by the associated eustatic value (positive for melting and negative for growth). Since their calculations did not include the complete collapse of the WAIS ice sheet, and specifically the inundation of the marine-based sectors of this ice sheet, one could treat the case of a full collapse by scaling the results in Figure 2.2 by the effective eustatic value cited above (~ 5 m).

It is unclear why the Clark and Lingle [1977] paper has been largely ignored in the subsequent discussions of projected sea-level changes associated with a collapse of the WAIS, but this neglect was immediate [Mercer, 1978] and sustained [e.g., Solomon et al., 2007]. In any event, the results in Figure 2.2, and more recent studies by Mitrovica et al. [2001] and Clark et al. [2002], indicate that future sea-level changes in response to loss of marine-based ice from Antarctica will neither be the eustatic nor the effective eustatic value, but rather a highly variable geographic signal that includes areas of sea-level fall as well as zones of accentuated (relative to the effective eustatic value) sea-level rise.

The Clark and Lingle [1977] analysis is not the final word on the issue, however, because it was based on a sea-level theory [Farrell and Clark, 1976] that makes two significant assumptions. First, the results in Figure 2.2 do not include the feedback on sea level of contemporaneous perturbations in the Earth's rotation vector, a process that was included in more recent analyses of sea-level fingerprints due to ongoing or late Quaternary melting events over the Antarctic [Mitrovica et al., 2001; Clark et al., 2002]. Second, the calculation assumes that there is no marine-based ice, i.e., that the melting of the WAIS does not lead to inundation of parts of this sector. One might

partially overcome this limitation by using the effective eustatic value, rather than the eustatic value, to scale the results in Figure 2.2; however this ad-hoc correction misses an important piece of physics. In particular, the melting of the WAIS would also produce a rebound of the underlying crust, and this rebound will act to push water out of the region and into the global oceans. That is, the topographic hole that exists today below the WAIS is not the same as the hole that would exist after the immediate elastic rebound and subsequent viscous uplift following ice sheet retreat.

The sea-level theory adopted by Clark and Lingle [1977] was a special (elastic) case of a theory that was developed to model sea-level changes associated with the Late Pleistocene ice-age cycles [Farrell and Clark, 1976]. However, over the last decade this "standard" theory has been extended to include rotational feedback [e.g., Milne and Mitrovica, 1996, 1998; Peltier, 1998; Mitrovica et al., 2005] and shoreline migration due to local changes in sea level at coastlines and/or the growth or ablation of grounded marine-based ice [e.g., Johnston, 1993; Milne, 1998; Milne et al., 1999; Mitrovica and Milne, 2003; Mitrovica, 2003; Kendall et al., 2005]. In this paper we update and extend the Clark and Lingle [1977] results by adapting recent advances in ice-age sea-level physics to compute and interpret fingerprints associated with melting from both the WAIS and marine-based sectors of the EAIS. Our goal here is to provide a far more comprehensive and state-of-the-art answer to the question posed near the beginning of this Chapter - namely, what is the projected sea-level change that would occur after the collapse of (parts of) the AIS?

In the next section we review, in largely symbolic notation, the theory and algorithm we apply to generate our sea-level predictions. The theory is a summary of a derivation that may be found in the recent literature of ice-age sea level [Mitrovica and Milne, 2003; Kendall et al., 2005], but we do not include it merely for completeness. Rather, as we discuss in formulating our numerical algorithm, the implementation of the theory necessary to predict future sea-level changes is fundamentally different from the implementation one would use to calculate ice-age sea-level variations. The

difference arises because the initial (i.e., before loading) topography is known in the former case, but it is unknown in the latter application.

2.2 A Theory for Forward Predictions of Sea-Level Change

Mitrovica and Milne [2003] and Kendall et al. [2005] derived a generalized sea-level theory for application to problems in glacial isostatic adjustment (GIA). Furthermore, they outlined a suite of numerical algorithms tailored to the ice-age problem; in particular, these algorithms were designed for a system that evolves from the onset of ice-age loading, at some time in the past, up to the present day. In this section we briefly review this generalized theory, and we derive a revised numerical algorithm suitable for calculations that yield projections of future sea-level change.

We begin by denoting the radial position of the sea surface and solid surface, where the latter does not include ice height, as G and R, respectively. The former symbol is commonly adopted with the GIA literature because the position of the sea surface has been taken to be identical, within the static sea-level theory, to the position of the gravitational equipotential referred to as the geoid [This correction has, however, been shown to be imprecise; Tamisiea, 2011]. The fields G and R may be defined globally, and their difference yields sea level:

$$SL(\theta, \psi, t_j) = G(\theta, \psi, t_j) - R(\theta, \psi, t_j). \tag{2.1}$$

where θ and ψ denote the colatitude and east-longitude, and t_j is the time. With this definition, a simple relationship holds between topography (minus ice height) and sea level:

$$T(\theta, \psi, t_j) = -SL(\theta, \psi, t_j). \tag{2.2}$$

Our definition of topography and the radial position of the solid surface can easily be altered

to include the ice height. However, we have chosen to proceed in the above manner in order to be consistent with the previous literature. Moreover, this definition simplifies the connection between topography and various concepts related to sea level. For example, locations with positive topography (negative sea level) are synonymous with "land", while marine settings are defined by negative topography (or positive sea level). In reference to the latter case, any site free of grounded ice is considered to be "ocean", while other locations are said to be covered by grounded, marine-based ice. In the absence of ice cover, a shoreline is defined wherever $T = SL = 0$.

With this nomenclature in mind, the ocean height may be computed by projecting global sea level defined in equation (2.1) onto the region covered by ocean. This projection can be written as

$$S(\theta, \psi, t_j) = SL(\theta, \psi, t_j) \cdot C^*(\theta, \psi, t_j), \tag{2.3}$$

where the ocean function, C^*, is defined by

$$C^*(\theta, \psi, t_j) = \begin{cases} 1 & \text{if } SL(\theta, \psi, t_j) > 0 \text{ and there is no grounded ice} \\ 0 & \text{elsewhere,} \end{cases} \tag{2.4}$$

The connection between the height of the sea-surface equipotential, G, the radial position of the solid surface, R, and sea level SL, as well as the projection defined by equation (2.3), is illustrated in top frame of Figure 2.3. Wherever the height of the sea-surface equipotential (with location given by the top of the water in open ocean regions and by the dashed line elsewhere) lies above the solid surface (the top of the region in brown), irregardless of the presence or absence of ice, the topography is negative (or sea level is positive). Where the height of the sea-surface equipotential lies below the solid surface the topography is positive (sea level is negative). Moreover, the ocean function, C^*, is 1 wherever the topography is negative and there is no grounded ice; this is true

over the ocean pictured in the figure, including regions of the ocean that are covered by floating ice. It is important to emphasize that areas in which the ocean function is equal to 1 are, by definition, filled with water from the solid surface up to the sea surface (or covered by an equivalent mass comprised of a combination of water and floating ice).

Changes in the distribution of ice and water, whether in the past or into the future, act to perturb the radial position of the bounding surfaces that define sea level. If we denote these perturbations by ΔG and ΔR, respectively, and the time just prior to the onset of load redistribution by $t = t_0$, then we can express G and R at a later time t_j as:

$$\begin{aligned} G(\theta, \psi, t_j) &= G(\theta, \psi, t_0) + \Delta G(\theta, \psi, t_j), \\ R(\theta, \psi, t_j) &= R(\theta, \psi, t_0) + \Delta R(\theta, \psi, t_j). \end{aligned} \tag{2.5}$$

Using these expressions in equation (2.1) yields an analogous decomposition for global sea level

$$SL(\theta, \psi, t_j) = SL(\theta, \psi, t_0) + \Delta SL(\theta, \psi, t_j), \tag{2.6}$$

where

$$\Delta SL(\theta, \psi, t_j) = \Delta G(\theta, \psi, t_j) - \Delta R(\theta, \psi, t_j). \tag{2.7}$$

One can write a similar expression for topography. Using (2.2) in (2.6) yields

$$T(\theta, \psi, t_j) = T(\theta, \psi, t_0) - \Delta SL(\theta, \psi, t_j). \tag{2.8}$$

The sea-surface height anomaly, G, is generally separated into spatially varying and spatially uniform components,

$$\Delta G(\theta, \psi, t_j) = \Delta \mathcal{G}(\theta, \psi, t_j) + \frac{\Delta \Phi(t_j)}{g}, \tag{2.9}$$

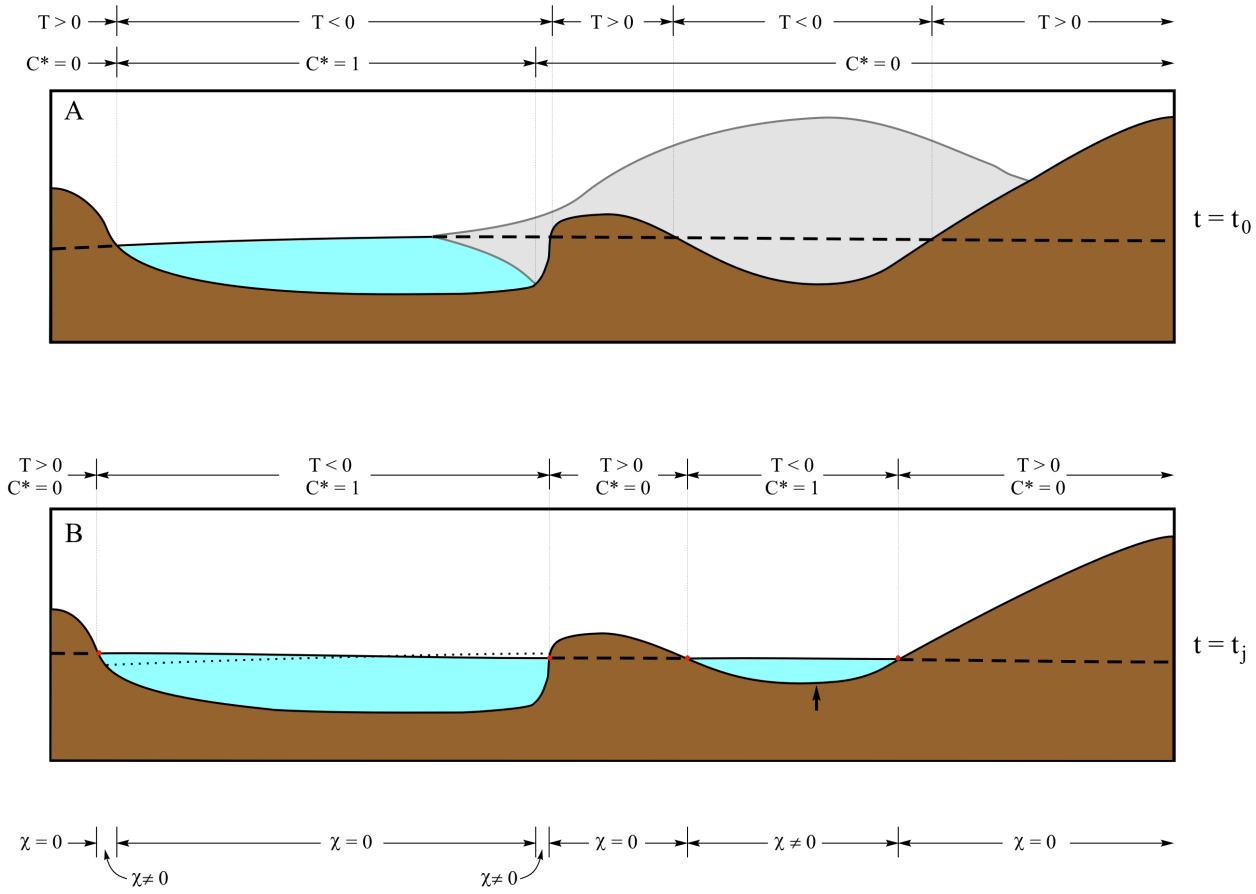

Figure 2.3: (A) Schematic illustrating the connection between sea level (or topography) and ocean height, following equation (2.3). The position of the sea surface equipotential, G, is given by the top of the open ocean and the dashed line in regions covered by ice or land. The height of the "solid surface", R, as we define it in the text, is given by the top of the region coloured in brown. Topography is positive (or sea level is negative) where $G < R$ and it is negative (sea level is positive) where $G > R$. Following equation (2.4), the ocean function, C^* is 1 where sea level is positive *and* there is no grounded marine-based ice, and it is zero elsewhere. (B) As in frame (A), except for the situation after all ice (floating and grounded) has melted. The thin dotted line at left on the figure shows the location of the original sea surface (i.e., the sea surface in frame A). At the base of the figure we indicate regions where $\chi \equiv T(t_0)[C^*(t_j) - C^*(t_0)]$ is zero or non-zero, where t_0 refers to the situation in frame (A) and t_j is the situation in frame (B). As discussed in the text, χ, which is the second term on the right-hand-side of the generalized sea-level equation (2.13), is non-zero wherever ocean exists at t_j and not t_0, or vica-versa. All symbols on the figure suppress the dependence on (θ, ψ, t).

where the uniform shift, $\frac{\Delta\Phi(t_j)}{g}$, will be constrained by invoking conservation of mass of the surface load (see below). The decomposition (2.9) has a straightforward physical interpretation. The sea surface is constrained, in a static sea-level theory, to remain an equipotential surface, However, as mass is transferred between ice and ocean reservoirs, and/or the Earth deforms in response to this changing load, the sea surface need not remain on the *same* equipotential surface through time [Dahlen, 1976]. The first term on the right-hand-side of equation (2.9) represents the perturbation in the original equipotential surface (i.e., the equipotential surface coincident with sea level at t_0) and the second term is the uniform shift that is associated with a change from one equipotential surface to another.

With this decomposition of the height of the sea-surface equipotential, we may also define

$$\Delta\mathcal{SL}(\theta,\psi,t_j) = \Delta\mathcal{G}(\theta,\psi,t_j) - \Delta R(\theta,\psi,t_j), \tag{2.10}$$

and equation (2.7) can then be rewritten as

$$\Delta SL(\theta,\psi,t_j) = \Delta\mathcal{SL}(\theta,\psi,t_j) + \frac{\Delta\Phi(t_j)}{g}. \tag{2.11}$$

Next, we turn to the ocean height. Deriving an expression for the change in ocean height relative to the initial ($t = t_0$) height is more complicated than the above derivations because determining this height requires, following equation (2.3), a projection onto the ocean function. If we write, in analogy with equation (2.5)

$$S(\theta,\psi,t_j) = S(\theta,\psi,t_0) + \Delta S(\theta,\psi,t_j), \tag{2.12}$$

then, equations (2.2), (2.3) and (2.6) yield, after some algebra, the generalized sea-level equation

(GSLE) derived by Mitrovica and Milne [2003]:

$$\begin{aligned}\Delta S(\theta,\psi,t_j) =& \Delta SL(\theta,\psi,t_j)C^*(\theta,\psi,t_j) \\ & - T(\theta,\psi,t_0)\left[C^*(\theta,\psi,t_j) - C^*(\theta,\psi,t_0)\right].\end{aligned} \tag{2.13}$$

The GSLE equation (2.13) indicates that the change in ocean height from the onset of loading is comprised of two terms. The first term on the right-hand-side is a simple projection of the total change in global sea level projected onto the ocean function at $t = t_j$ (i.e., from equation (2.3), a projection of global sea level onto all marine areas free of grounded ice at $t = t_j$). The second is a term which takes into account changes in geometry of oceans from $t = t_0$ to $t = t_j$. Specifically, this "correction" term [see Mitrovica and Milne, 2003] involves a projection of the initial topography onto a field which is non-zero only in locations in which the ocean geometry has changed during this time interval.

To illustrate these concepts, Figure 2.3 shows a rather general case in which an area that includes both floating and grounded marine based ice, as well as land ice (frame A), becomes ice free (frame B). We discussed Figure 2.3A above. In Figure 2.3B all areas with negative topography (positive sea level) are oceans (i.e., $C^* = 1$). If we take $t = t_0$ in the frame A and $t = t_j$ in the frame B, then at the bottom of the plot we indicate locations where the second correction term on the right-hand-side of GSLE equation (2.13) is either zero or non-zero. Specifically, this term is non-zero in all regions where the ocean function has changed across the time interval; that is, all locations that accommodate water at $t = t_j$ but not at $t = t_0$. Thus, this correction term tracks changes in shoreline geometry which can arise from local changes in sea level leading to onlap (e.g., the coast on the far left of the plot) or offlap, or through a combination of these local changes and the disappearance of grounded, marine-based ice (e.g., near the right coast of the ocean at left, and within the marine depression at right.)

Local changes in sea level (i.e., changes in the relative position of the sea surface equipotential and solid surface) are governed by the first term on the right-hand-side of equation (2.13). This term incorporates the gravitational, deformational and rotational changes in sea level driven by the change in the surface mass (ice plus ocean) load. Indeed, it is this term that controls the basic physics of post-glacial sea-level change that we discussed in the Introduction. For example, the movement of water away from the location of a melting ice sheet in response to a loss in gravitational attraction between the ice and water, evident in the fingerprint prediction of Clark and Lingle [1977] (Figure 2.2), and also in the change in tilt of the sea surface from Figure 2.3A to B, would be included in the so-called self-attraction term that would form part of any mathematical expression for $\Delta SL(\theta, \psi, t_j)$. Similarly, we pointed out in the Introduction that standard sea-level theories [Farrell and Clark, 1976; Clark and Lingle, 1977] do not incorporate the inundation of water in regions vacated by the retreat of grounded, marine-based ice, and the expulsion of some of this water as the inundated region viscoelastically rebounds. In the generalized sea-level theory, this inundation is included via the second term on the right-hand-side of equation (2.13), which "activates" this region as a reservoir for water (note the $\chi \neq 0$ value for the marine depression to the right of Figure 2.3B). However, the physics of water expulsion is captured by the sea-level change (or perturbations in the positions of the sea and solid surface) over the inundated region that would be incorporated into any detailed expression for $\Delta SL(\theta, \psi, t_j)$ on the right-hand-side of equation (2.13).

We must emphasize, however, that the two terms on the right-hand-side of the GLSE (2.13) are not independent of each other: Changes in global sea level, $\Delta SL(\theta, \psi, t_j)$, map into changes in the ocean function $C^*(\theta, \psi, t_j)$ via equation (2.4).

It will be useful to rewrite equation (2.13) in a slightly modified form. In particular, rather than considering the total change in sea level (or ocean height) from the onset of loading, we can

instead consider a change across two successive time steps in the evolution, say from $t = t_{j-1}$ to $t = t_j$. In particular, if the change in ocean height across this shorter time interval is given by

$$\delta S(\theta, \psi, t_j) = S(\theta, \psi, t_j) - S(\theta, \psi, t_{j-1}) = \Delta S(\theta, \psi, t_j) - \Delta S(\theta, \psi, t_{j-1}), \tag{2.14}$$

then equation (2.13) can be rewritten as

$$\begin{aligned} \delta S(\theta, \psi, t_j) = &- \Delta S(\theta, \psi, t_{j-1}) + \Delta SL(\theta, \psi, t_j) C^*(\theta, \psi, t_j) \\ &- T(\theta, \psi, t_0) \left[C^*(\theta, \psi, t_j) - C^*(\theta, \psi, t_0) \right]. \end{aligned} \tag{2.15}$$

Moreover, using the decomposition (2.11) yields

$$\begin{aligned} \delta S(\theta, \psi, t_j) = &- \Delta S(\theta, \psi, t_{j-1}) + \Delta \mathcal{SL}(\theta, \psi, t_j) C^*(\theta, \psi, t_j) + \frac{\Delta \Phi(t_j)}{g} C^*(\theta, \psi, t_j) \\ &- T(\theta, \psi, t_0) \left[C^*(\theta, \psi, t_j) - C^*(\theta, \psi, t_0) \right]. \end{aligned} \tag{2.16}$$

This version of the GSLE is in a form amenable to numerical solution, as we describe in the following section.

2.2.1 A Numerical Implementation

For the purpose of brevity it will be useful to rewrite equation (2.16) using a notation in which the dependence on the colatitude and east longitude is implicit and the time dependence is indicated by a subscript:

$$\delta S_j = -\Delta S_{j-1} + \Delta \mathcal{SL}_j C_j^* + \frac{\Delta \Phi_j}{g} C_j^* - T_0 \left[C_j^* - C_0^* \right]. \tag{2.17}$$

where we note that only the term $\frac{\Delta \Phi_j}{g}$ is independent of (θ, ψ).

Our GSLE holds for any kind of Earth model and may be applied as long as a formalism exists for computing the change in global sea level $\Delta \mathcal{SL}$ given some surface mass (ice plus ocean) loading

history. For example, Kendall et al. [2005] described a complete spectral theory, ultimately based on viscoelastic Love number theory [Peltier, 1974], for the case of a rotating, self-gravitating Earth model with depth-varying (i.e., 1-D) linear viscoelastic structure. The results described throughout this thesis are based on an implementation of the Kendall et al. [2005] expressions for $\Delta\mathcal{SL}$, though we adopt a new theory for computing load-induced perturbations in Earth rotation [Mitrovica et al., 2005]. We summarize the main elements of the theory we use for computing $\Delta\mathcal{SL}$ in section 2.2.2. We emphasize, however, that the same equation (2.17) also holds for 3-D Earth models of arbitrary complexity, and in this case expressions for $\Delta\mathcal{SL}$ may be generated, for example, using a suite of numerical algorithms that have been designed to treat the 3-D loading of a viscoelastic Earth [Martinec, 2000; Wu and van der Wal, 2003; Zhong et al., 2003; Latychev et al., 2005].

In the viscoelastic calculation, the perturbation $\Delta\mathcal{SL}$ is dependent on the complete time history of the surface load and rotation vector. We make this dependence explicit by re-writing equation (2.17) in the form

$$\delta S_j = -\Delta S_{j-1} + \Delta\mathcal{SL}_j \left(\underset{0\le m\le j}{\delta I_m} ; \underset{0\le m<j-1}{\delta S_m} ; \delta S_j; \underset{0\le m<j-1}{\delta\omega_m} ; \delta\omega_j \right) C_j^* + \frac{\Delta\Phi_j}{g} C_j^* - T_0 \left[C_j^* - C_0^* \right], \tag{2.18}$$

In this expression the history of the surface mass load has been decomposed into increments across two successive time steps of ocean height, δS_m, and ice height, δI_m, which are both functions of (θ, ψ), and an analogous set of increments for perturbations in the rotation vector, $\delta\omega_m$. For reasons that will become clear below, the ocean height and rotation vector increments have been separated into the increment at t_j and all prior increments.

The form of equation (2.18) makes clear that the GSLE is an integral equation. That is, the ocean height increment being solved for, δS_j, also appears on the right-hand-side of the equation in the expression for $\Delta\mathcal{SL}_j$. This form reflects the fact that changes in the ocean height are

governed by the gravitational field of the planet, and that this field is in turn perturbed by ocean height changes. The perturbation arises because of both the direct attraction of the load and the deformation it induces. Other terms on the right-hand-side of equation (2.18) also depend on the δS_j, albeit implicitly: C_j^* (via equation 2.4), $\frac{\Delta\Phi_j}{g}$ (see below), and $\delta\omega_j$ (since the perturbation in the rotation vector will depend on all load increments).

As mentioned above, an expression for $\frac{\Delta\Phi_j}{g}$ may be obtained by invoking conservation of mass of the surface load. Specifically, multiplying both sides of equation (2.18) by the density of water, ρ_w, integrating over the surface of the Earth (Ω), and rearranging yields:

$$\begin{aligned}\frac{\Delta\Phi_j}{g} = &-\frac{1}{\mathcal{A}_j}\frac{\rho_{\mathrm{I}}}{\rho_{\mathrm{W}}}\iint_{\Omega}\Delta I_j d\Omega \\ &-\frac{1}{\mathcal{A}_j}\iint_{\Omega}\Delta\mathcal{SL}_j\left(\underset{0\le m\le j}{\delta I_m};\underset{0\le m<j-1}{\delta S_m};\delta S_j\underset{0\le m<j-1}{\delta\omega_m};\delta\omega_j\right)C_j^* d\Omega \\ &+\frac{1}{\mathcal{A}_j}\iint_{\Omega}T_0\left[C_j^*-C_0^*\right]d\Omega,\end{aligned} \tag{2.19}$$

where ρ_{I} is the density of ice, ΔI_j is the total change in the ice load height from time t_0 to t_j (i.e., the sum of increments δI_m, from $m = 1, j$), and

$$\mathcal{A}_j = \iint_{\Omega} C_j^* d\Omega. \tag{2.20}$$

is the area of oceans that is free of grounded ice at t_j.

The system of equations (2.18-2.20) may be solved at each time step t_j using an iterative scheme. Specifically, if we use i to denote the iteration counter, then our numerical algorithm is based on

the following:

$$\begin{aligned}\delta S_j^i = &- \Delta S_{j-1} + \Delta\mathcal{SL}_j^{i-1}\left(\begin{smallmatrix}\delta I_m \\ 0\le m\le j\end{smallmatrix};\ \begin{smallmatrix}\delta S_m \\ 0\le m<j\end{smallmatrix}; \delta S_j^{i-1};\ \begin{smallmatrix}\delta\omega_m \\ 0\le m<j\end{smallmatrix}; \delta\omega_j^{i-1}\right) C_j^{*,i-1} \\ &+ \frac{\Delta\Phi_j^{i-1}}{g} C_j^{*,i-1} - T_0\left[C_j^{*,i-1} - C_0^*\right],\end{aligned} \tag{2.21}$$

$$\begin{aligned}\frac{\Delta\Phi_j^{i-1}}{g} = &- \frac{1}{\mathcal{A}_j^{i-1}}\frac{\rho_{\rm I}}{\rho_{\rm W}}\iint\limits_\Omega \Delta I_j d\Omega \\ &- \frac{1}{\mathcal{A}_j^{i-1}}\iint\limits_\Omega \Delta\mathcal{SL}_j^{i-1}\left(\begin{smallmatrix}\delta I_m \\ 0\le m\le j\end{smallmatrix};\ \begin{smallmatrix}\delta S_m \\ 0\le m<j\end{smallmatrix}; \delta S_j^{i-1};\ \begin{smallmatrix}\delta\omega_m \\ 0\le m<j\end{smallmatrix}; \delta\omega_j^{i-1}\right) C_j^{*,i-1} d\Omega \\ &+ \frac{1}{\mathcal{A}_j^{i-1}}\iint\limits_\Omega T_0\left[C_j^{*,i-1} - C_0\right] d\Omega,\end{aligned} \tag{2.22}$$

and

$$\mathcal{A}_j^{i-1} = \iint\limits_\Omega C_j^{*,i-1} d\Omega. \tag{2.23}$$

In these equations, the value of the total ocean height change at the previous time step $t = t_{j-1}$, ΔS_{j-1}, is assumed to be known (i.e., solved for). An initial guess for the ocean height increment δS_j^0 (see below) can then be used, in combination with all ice load increments δI_m $(m = 1, j)$ and ocean height and rotation increments before t_j, i.e., δS_m and $\delta\omega_m$ for $m = 1, j-1$, to compute all elements required for the right-hand-side of equation (2.21): $\delta\omega_j^0$, $\Delta\mathcal{SL}_j^0$, C_j^0, $\mathcal{A}_j^0$, and $\Delta\Phi_j^0$ (in that order). Then, using equation (2.21), the next estimate for δS_j^1 may be obtained, and the process is repeated until convergence.

As a starting guess for δS_j^0 we use the geographically uniform (eustatic) meltwater distribution associated with the ice increment δI_j (i.e., $\delta S_j = -\delta V_j^I \rho_i/(\rho_w A_j^o)$, where δV_j^I is the change in the volume of ice across the j^{th} time step).

The iteration scheme (2.21-2.23) differs significantly from the methodology used in the calculation of ice-age sea-level changes [Kendall et al., 2005]. In our present application, where we

are concerned with projections of future sea-level change, the initial topography T_0 is simply the present-day topography and it is therefore known. In contrast, in the ice-age problem the initial topography is the topography at the start of the ice-age loading and this is unknown at the onset of the calculation; only the present-day (observed) topography is known. Therefore, in ice-age applications a second "outer" iteration "k" loop is applied over the full loading history such that a first guess to the initial topography, $T_0^{k=0}$, is successively refined until the time-stepped numerical scheme yields a present-day topography that has converged to the actual, observed topography [Peltier, 1994; Milne et al., 1999; Kendall et al., 2005].

In the calculations below, we will compare our results to predictions based on the standard sea-level equation derived by Farrell and Clark [1976] and adopted by Clark and Lingle [1977]. Their derivation assumed that there are no marine-based ice components, that all shorelines remain fixed in time, and that there is no feedback associated with perturbations in Earth rotation. It also assumes a non-rotating Earth. In this case, the algorithm outlined above simplifies to the following:

$$\delta S_j^i = -\Delta S_{j-1} + \Delta \mathcal{SL}_j^{i-1} \left(\underset{0\le m\le j}{\delta I_m} ; \underset{0\le m<j}{\delta S_m} ; \delta S_j^{i-1} \right) C + \frac{\Delta \Phi_j^{i-1}}{g} C, \tag{2.24}$$

$$\frac{\Delta \Phi_j^{i-1}}{g} = -\frac{1}{\mathcal{A}} \frac{\rho_{\mathrm{I}}}{\rho_{\mathrm{W}}} \iint_\Omega \Delta I_j d\Omega - \frac{1}{\mathcal{A}} \iint_\Omega \Delta \mathcal{SL}_j^{i-1} \left(\underset{0\le m\le j}{\delta I_m} ; \underset{0\le m<j}{\delta S_m} ; \delta S_j^{i-1} \right) C d\Omega, \tag{2.25}$$

where C is equal to 1 over the present-day ocean and zero elsewhere, and A is the area of that ocean:

$$\mathcal{A} = \iint_\Omega C d\Omega. \tag{2.26}$$

2.2.2 Love Number Theory for Computing $\Delta\mathcal{SL}$

To compute the spatially variable component of global sea-level change, $\Delta\mathcal{SL}$, we adopt a spherically symmetric, self-gravitating Maxwell viscoelastic Earth model and employ viscoelastic Love number

theory [Peltier, 1974] to compute the response of the solid Earth and sea surface equipotential to a change in mass loading. The theory outlined here is valid for spherically symmetric, viscoelastically deforming Earth models. First, following Kendall et al. [2005], we present the case of a non-rotating Earth model, and then derive and add the additional terms necessary to account for the signal associated with perturbations in Earth rotation (Section 2.2.3).

The total change in surface loading is comprised of changes in the distributions of ice (ΔI) and water (ΔS) and is given by,

$$\Delta L(\theta, \psi, t_j) = \rho_w \Delta S(\theta, \psi, t_j) + \rho_i \Delta I(\theta, \psi, t_j). \tag{2.27}$$

We can model this load history as a series of Heaviside load increments as follows,

$$\Delta L(\theta, \psi, t_j) = \sum_{n=0}^{N} \left[\rho_i \delta I_n(\theta, \psi) + \rho_w \delta S_n(\theta, \psi)\right] H(t - t_n) \tag{2.28}$$

where

$$H(t - t_n) = \begin{cases} 0 & \text{if } t < t_n \\ \\ 1 & \text{if } t \geq t_n. \end{cases} \tag{2.29}$$

The geographically variable component of the change in sea level in response to this load change may be expressed as a space-time convolution of the load with the viscoelastic Green's functions for the gravitational potential perturbation (ϕ) and the radial displacement (Γ):

$$\Delta \mathcal{SL}(\theta, \psi, t_j) = \int_{-\infty}^{t_j} \iint_{\Omega} \Delta L(\theta', \psi', t'_j) \left[\frac{\phi(\gamma, t_j - t')}{g} - \Gamma(\gamma, t_j - t')\right] d\Omega' dt'. \tag{2.30}$$

The Green's functions in equation 2.30 may be written in terms of non-dimensional surface load Love numbers. The Love numbers h and k describe the impulse response of the Earth to loading

at spherical harmonic degree l. They take the form,

$$h_l(t) = h_l^E \delta(t) + \sum_{k=1}^{K} r_k^l e^{-s_k^l t}, \tag{2.31}$$

$$k_l(t) = k_l^E \delta(t) + \sum_{k=1}^{K} r_k'^l e^{-s_k^l t}, \tag{2.32}$$

where, in each equation, the first term gives the instantaneous elastic response of the Earth, and the second term gives the non-elastic response as a sum of K modes of exponential decay. These modes arise, for example, from the deformation of density discontinuity layers within the Earth. Thus when a load is applied, there will be an instantaneous elastic response, followed by non-elastic deformation that tends exponentially towards a final equilibrium state.

The Love number $h_l(t)$ are coefficients in a Legendre polynomial expansion of the Green's function for the radial displacement of the solid surface:

$$\Gamma(\gamma, t) = \frac{a}{M_e} \sum_{l=0}^{\infty} \left[h_l^E \delta(t) + \sum_{k=1}^{K} r_k^l e^{-s_k^l t} \right] P_l(\cos\gamma), \tag{2.33}$$

where a and M_e are the radius and mass of the Earth, respectively, and

$$\cos\gamma = \cos\theta\cos\theta' + \sin\theta\sin\theta'\cos(\psi - \psi'). \tag{2.34}$$

The $k_l(t)$ are coefficients in a Legendre polynomial expansion of the Green Function for the gravitational potential perturbation:

$$\phi(\gamma, t) = \frac{ag}{M_e} \sum_{l=0}^{\infty} \left[\delta(t) + k_l^E \delta(t) + \sum_{k=1}^{K} r_k'^l e^{-s_k^l t} \right] P_l(\cos\gamma) \tag{2.35}$$

where the $\delta(t)$ represents the potential perturbation due to the direct gravitational effect of the

impulse load. Substituting equations 2.33 and 2.35 into equation 2.30 and rearranging yields

$$\Delta\mathcal{SL}(\theta,\psi,t_j) = \int_{-\infty}^{t_j}\iint_{\Omega}\Delta L(\theta',\psi',t_j')\times \\ \sum_{l=0}^{\infty}\left[(1+k_l^E\delta(t)-h_l^E\delta(t))\delta(t_j-t')+\sum_{k=1}^{K}(r_k^{'l}-r_k^l)e^{-s_k^l(t_j-t')}\right]P_l(\cos\gamma)d\Omega' dt'. \tag{2.36}$$

Using the time dependence give by equation 2.28 allows the time convolution to be performed analytically, and this gives

$$\Delta\mathcal{SL}(\theta,\psi,t_j) = \frac{a}{M_e}\sum_{l=0}^{\infty}E_l\iint_{\Omega}\left[\rho_i\Delta I_j(\theta',\psi')+\rho_w\Delta S_j(\theta',\psi')\right]P_l(\cos\gamma)d\Omega' \\ +\frac{a}{M_e}\sum_{l=0}^{\infty}\sum_{n=0}^{N}H(t_j-t_n)\beta(l,t_n,t_j)\iint_{\Omega}\left[\rho_i\delta I_n(\theta',\psi')+\rho_w\delta S_n(\theta',\psi')\right]P_l(\cos\gamma)d\Omega' \tag{2.37}$$

where the Love numbers are embedded within the parameters

$$E_l = 1+k_l^E-h_l^E \tag{2.38}$$

and

$$\beta(l,t_n,t_j) = \sum_{k=1}^{K}\frac{r_k^{'l}-r_k^l}{s_k^l}\left[1-e^{-s_k^l(t_j-t_n)}\right]. \tag{2.39}$$

We employ a spherical harmonic (spectral) approach to derive analytic expressions for the spatial convolutions. Any scalar field $\chi(\theta,\psi)$ defined on the surface of a sphere as a spherical harmonic expansion may be expressed as follows,

$$\chi(\theta,\psi,t) = \sum_{l=0}^{\infty}\sum_{m=-l}^{l}\chi_{lm}(t)Y_{lm}(\theta,\psi) \tag{2.40}$$

where l and m are the spherical harmonic degree and order, respectively, and the $Y_{lm}(\theta,\psi)$ are

spherical harmonic basis functions that satisfy the normalization,

$$\iint_{\Omega} Y_{l'm'}(\theta,\psi)Y^{*}_{lm}(\theta,\psi)\sin\theta d\theta d\psi = 4\pi a^2 \delta_{l'l}\delta_{m'm}. \tag{2.41}$$

Using the addition theorem of spherical harmonics, we can also write,

$$\iint_{\Omega} \chi(\theta',\psi')P_l(\cos\gamma)d\Omega' = \frac{4\pi a^2}{2l+1}\sum_{m=-l}^{l}\chi_{lm}Y_{lm}(\theta,\psi). \tag{2.42}$$

Expressing each of the scalar fields in equation 2.37 in terms of a spherical harmonic decomposition and using equation 2.42 yields

$$\begin{aligned}\Delta\mathcal{SL}(\theta,\psi,t_j) =& \sum_{l,m} T_l E_l \left[\rho_i \Delta I_{l,}(t_j) + \rho_w \Delta S_{lm}(t_j)\right] Y_{lm}(\theta,\psi) \\ &+ \sum_{l,m} T_l \sum_{n=0}^{j-1} \beta(l,t_n,t_j)\left[\rho_i \delta I_{lm}(t_n) + \rho_w \delta S_{lm}(t_n)\right] Y_{lm}(\theta,\psi)\end{aligned} \tag{2.43}$$

where we define

$$T_l \equiv \frac{4\pi a^3}{M_e(2l+1)}. \tag{2.44}$$

2.2.3 Rotational Component of $\Delta\mathcal{SL}$

On a rotating Earth, perturbations in the Earth's rotation vector induced by changes in surface mass (ice plus ocean) loading will perturb sea-level [Milne and Mitrovica, 1996, 1998; Mitrovica et al., 2005]. A normal mode theory for computing changes in the magnitude and orientation of the rotation vector following a change in surface mass loading, valid for a spherically symmetric viscoelastic Earth model, may be found in Mitrovica et al. [2005] and will not be covered here. However, following Kendall et al. [2005], we summarize the theory needed to include the effect of Earth rotation changes on sea level.

Changes in the Earth's rotation vector following the onset of surface load changes alter the inertia tensor of the system, which gives rise to an evolving centrifugal potential perturbation referred to as a "driving potential" [Milne and Mitrovica, 1998]. The driving potential, $\Lambda(\theta, \psi, t_j)$, is described completely by degree 0 and 2 spherical harmonics, taking the form

$$\Delta\Lambda(\theta, \psi, t_j) = \Delta\Lambda_{0,0}(t_j)Y_{0,0}(\theta, \psi) + \sum_{m=-2}^{2} \Delta\Lambda_{2,m}(t_j)Y_{2,m}(\theta, \psi). \tag{2.45}$$

For small perturbations to the rotation vector caused by the ice distribution changes considered here, the driving potential is dominated by a degree two and order one "quadrential" geometry (as discussed in detail below).

The method for computing the response of sea level to the driving potential is analogous to the method used in section 2.2.2 for surface load changes. We can model the driving potential as a series of Heaviside increments (as in the expression for the surface loading given by equation 2.28) as follows

$$\Delta\Lambda_{lm}(t) = \sum_{n=0}^{N} \delta\Lambda_{lm}(t_n)H(t - t_n). \tag{2.46}$$

The viscoelastic tidal Love numbers (as opposed to surface mass load Love numbers),

$$k_l^T(t) = k_l^{T,E}\delta(t) + \sum_{k=1}^{K} r_k'^{l,T} e^{-s_k^l t} \tag{2.47}$$

$$h_l^T(t) = k_l^{T,E}\delta(t) + \sum_{k=1}^{K} r_k^{l,T} e^{-s_k^l t}, \tag{2.48}$$

where T refers to the tidal forcing, may be used to describe the response of the Earth to a potential forcing. A time convolution of the spherical harmonic coefficients of the driving potential with a sea level Green's functions associated with a tidal forcing yields the spherical harmonic coefficients

of the sea-level perturbation associated with the driving potential:

$$\Delta\mathcal{SL}_{lm}T(t_j) = \int_{-\infty}^{t_j} \Delta\Lambda_{lm}(t') \left[\frac{\phi_l^T(t_j - t')}{g} - \Gamma_l^T(t_j - t') \right] dt', \tag{2.49}$$

where the Green's functions $\phi_l^T(t)$ and $\Gamma_l^T(t)$ may be simply expressed in terms of the tidal Love numbers [Milne and Mitrovica, 1998; Peltier, 2007] as follows,

$$\phi_l^T(t) = \delta(t) + k_l^T(t) \tag{2.50}$$

$$\Gamma_l^T(t) = \frac{1}{g} h_l^T(t). \tag{2.51}$$

The Dirac-delta function in equation 2.50 accounts for the direct effect of the potential forcing. Finally, combining equations 2.46 - 2.51, the spherical harmonic coefficients of the sea-level perturbation associated with rotation effects may be written as:

$$\Delta\mathcal{SL}_{lm}^T(t_j) = \frac{1}{g} E_l^T \Delta\Lambda_{lm}(t_j) + \frac{1}{g} \sum_{n=0}^{j-1} \beta^T(l, t_n, t_j) \delta\Lambda_{lm}(t_n), \tag{2.52}$$

where

$$E_l^T = 1 + k_l^{T,E} - h_l^{T,E} \tag{2.53}$$

and

$$\beta^T(l, t_n, t_j) = \sum_{k=1}^{K} \frac{r_k'^{l,T} - r_k^{l,T}}{s_k^l} \left[1 - e^{-s_k^l (t_j - t_n)} \right]. \tag{2.54}$$

Adding equation 2.52 into equation 2.43 for the total sea-level change, we arrive at our final ex-

pression:

$$\begin{aligned}\Delta\mathcal{SL}(\theta,\psi,t_j) = &\sum_{l,m} T_l E_l \left[\rho_i \Delta I_{l,}(t_j) + \rho_w \Delta S_{lm}(t_j)\right] Y_{lm}(\theta,\psi) \\ &+ \sum_{l,m} T_l \sum_{n=0}^{j-1} \beta(l,t_n,t_j) \left[\rho_i \delta I_{lm}(t_n) + \rho_w \delta S_{lm}(t_n)\right] Y_{lm}(\theta,\psi) \\ &+ \sum_{l,m} \frac{1}{g} E_l^T \left[\Delta\Lambda_{lm}(t_j)\right] Y_{lm}(\theta,\psi) \\ &+ \sum_{l,m} \frac{1}{g} \sum_{n=0}^{j-1} \beta^T(l,t_n,t_j) \left[\delta\Lambda_{lm}(t_n)\right] Y_{lm}(\theta,\psi).\end{aligned} \tag{2.55}$$

The associated expression for the term $\frac{\Delta\Phi_j}{g}$ for the uniform shift in the height of the sea-surface equipotential is given in Kendall et al. [2005].

All calculations in Chapters 2, 3 and 6 (unless otherwise specified) employ the sea-level theory valid for a rotating Earth model, while Chapters 4 and 5 consider flowline ice sheet simulations in which ice and water loading changes are symmetric about the Earth's rotation poles and therefore rotational effects need not be included.

2.3 Results and Discussion of Sea-Level Changes Following Future Ice-Sheet Collapse

We will consider two different scenarios for melting from the Antarctic. In the first, we melt the entire WAIS. The total (grounded) volume of the ice sheet corresponds to an eustatic sea-level rise of 8.4 m, and an effective eustatic value (henceforth EEV) of 5.0 m. In the second, we remove ice only from marine-based sectors of the EAIS (see Figure 2.1). This volume, which is taken largely from Wilkes Land, corresponds to a eustatic sea-level rise of 18.0 m, and an EEV of 14.2 m. Our ice thickness model for these regions is taken from the EISMINT web site (http://homepages.vub.ac.be/ phuybrec/eismint/antarctica.html).

The sea-level algorithm described above will be solved using a so-called pseudo-spectral methodology [Kendall et al., 2005]. In particular, $\Delta\mathcal{SL}_j$ is computed in the spectral (i.e, spherical harmonic) domain, while all projection operations required in the various terms of equations (2.21-2.22) are performed in the space domain and then converted into the spectral domain. The switching back and forth between spectral and space domains is motivated by the fact that projections are much more efficiently computed in the space domain (where they are simply multiplications between associated grid elements) than in the spectral domain. These spectral calculations are all performed up to spherical harmonic degree and order 512. The present-day topography, T_0, is given by ETOPO2 (http://www.ngdc.noaa.gov/mgg/fliers/01mgg04.html) with the ice thickness model removed.

Our predictions will be based on an Earth model with elastic and density structure taken from the seismic inference PREM [Dziewonski and Anderson, 1981]. We begin with predictions of sea-level change "soon" after the collapse of the ice sheets. In this case we assume that the time elapsed from the onset of melting to the observation of the sea-level change is sufficiently small that no viscous relaxation occurs. As a preliminary investigation of the effect of viscous relaxation on these "elastic" predictions, we end this section with a set of calculations that predict the change in sea level 500 years after the melting event has ceased. These calculations, in contrast to the elastic predictions, will be a function of the adopted radial profile of mantle viscosity, and for this purpose we use a profile that is amongst a class of inferences that has received wide support within the ice-age modeling community [e.g., Lambeck et al., 1998; Mitrovica and Forte, 2004]. The profile is characterized by an elastic lithosphere of thickness 120 km, an upper mantle viscosity of 5×10^{20} Pa s, and a lower mantle viscosity of 5×10^{21} Pa s.

In Figure 2.4A and B we show normalized sea-level fingerprints for the collapse of the WAIS computed using the full sea-level theory (equations 2.21-2.23) and the older theory of Farrell and Clark [1976] (equations 2.24-2.26), respectively. Figure 2.4C is the difference between these two

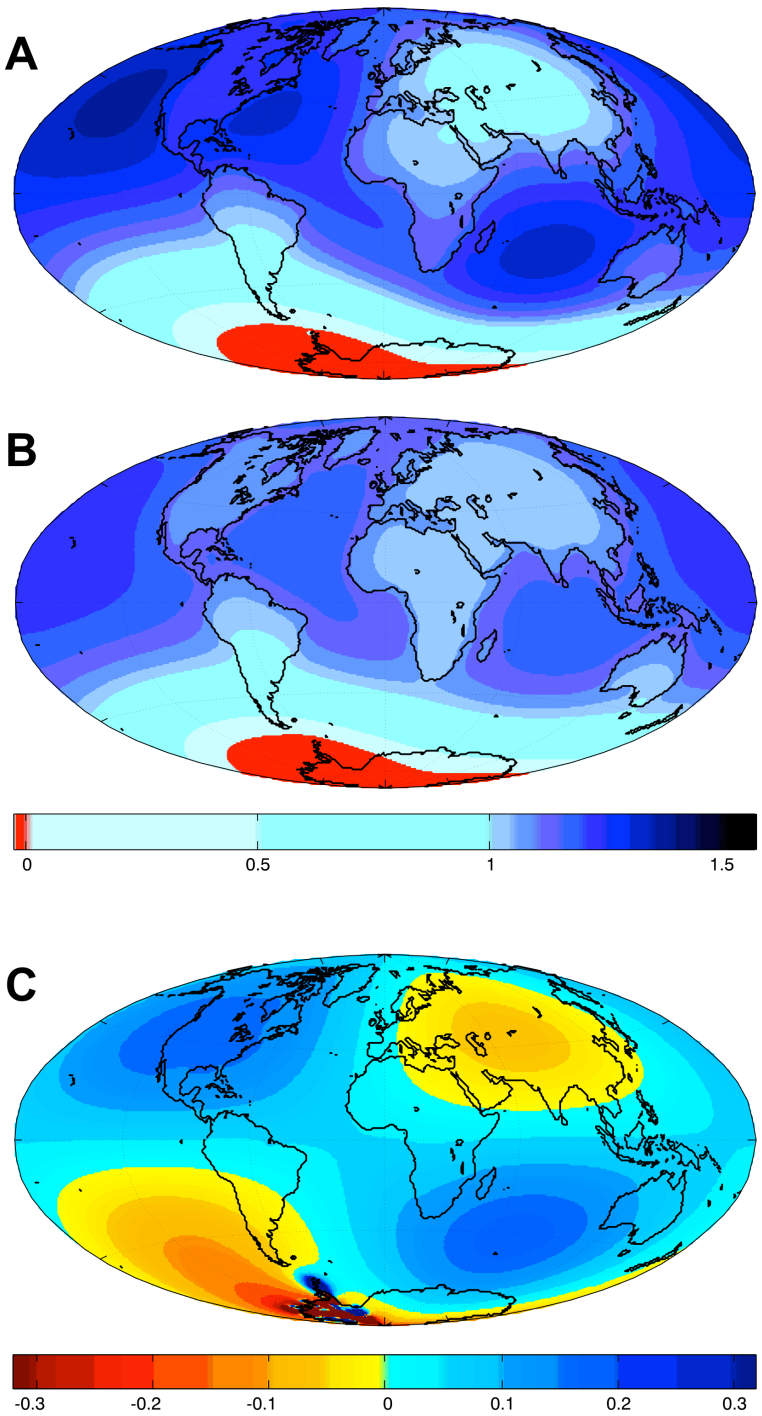

Figure 2.4: (A) Sea-level change in response to the collapse of the WAIS computed using the full sea-level theory described by equations (2.21-2.23). The total volume of the WAIS is used in the calculation, but the prediction is normalized by the effective eustatic value. (B) As in frame (A), except that the calculations adopt an older sea-level theory (see equations 2.24-2.25) which assumes a non-rotating Earth, no marine-based ice, and shorelines that remain fixed (to the present-day geometry) with time. In this calculation only an amount of ice with a volume that matches the effective eustatic sea-level rise for the ice model in frame (A) (5.0 m; see text) is removed from the system. (C) The difference between predictions generated using the new and old sea-level theories (frame A minus B).

predictions.

Figure 2.4B accurately reproduces the fingerprint computed by Clark and Lingle [1977], shown in Figure 2.2, despite differences in the adopted elastic Earth model (PREM in our case versus 1066B), the geometry of melting (Clark and Lingle [1977] assumed a uniform thinning of the WAIS), and the sea-level formalism (Clark and Lingle [1977] solved the sea-level equation using a spatial gridding of the Earth's surface which had an effective resolution that was significantly less than our spectral truncation). Figure 2.4B is characterized by peak values in the north Atlantic and Indian Oceans of 1.19, and a global peak value of 1.25 in the north Pacific Ocean. These values are less than one percent lower than the associated peaks in Figure 2.2. Our calculations also show the same tapering down to progressively lower contour values toward the shorelines in oceanic regions. Our results, in contrast to those in Figure 2.2, show variations in sea level over both land and water, and these global patterns confirm our earlier physical argument for the tapering. Namely, this trend is due to ocean loading, which causes a downward flexure of the oceans and an upward flexure of the continents.

A comparison between Figures 2.4A and B indicates that the new sea-level theory described in the last section yields a far-field signal that is characterized by significantly enhanced sea-level rise relative to the theory adopted by Clark and Lingle [1977]. The peaks in the north Atlantic and north Pacific ocean reach 1.32 and 1.37, respectively, and both have migrated closer to the coastlines of North America, while the peak in the Indian Ocean is 1.33. The difference plot (Figure 2.4C) indicates that the largest enhancements occur on the coasts of the U.S., and in particular the west coast; in these regions, the new theory predicts a normalized sea-level rise $\sim$0.15 higher than the older theory, or 0.8 m for an EEV of 5 m. A similar enhancement occurs over the southern Indian Ocean.

The pattern evident in Figure 2.4C is strongly suggestive of a dominant contribution from

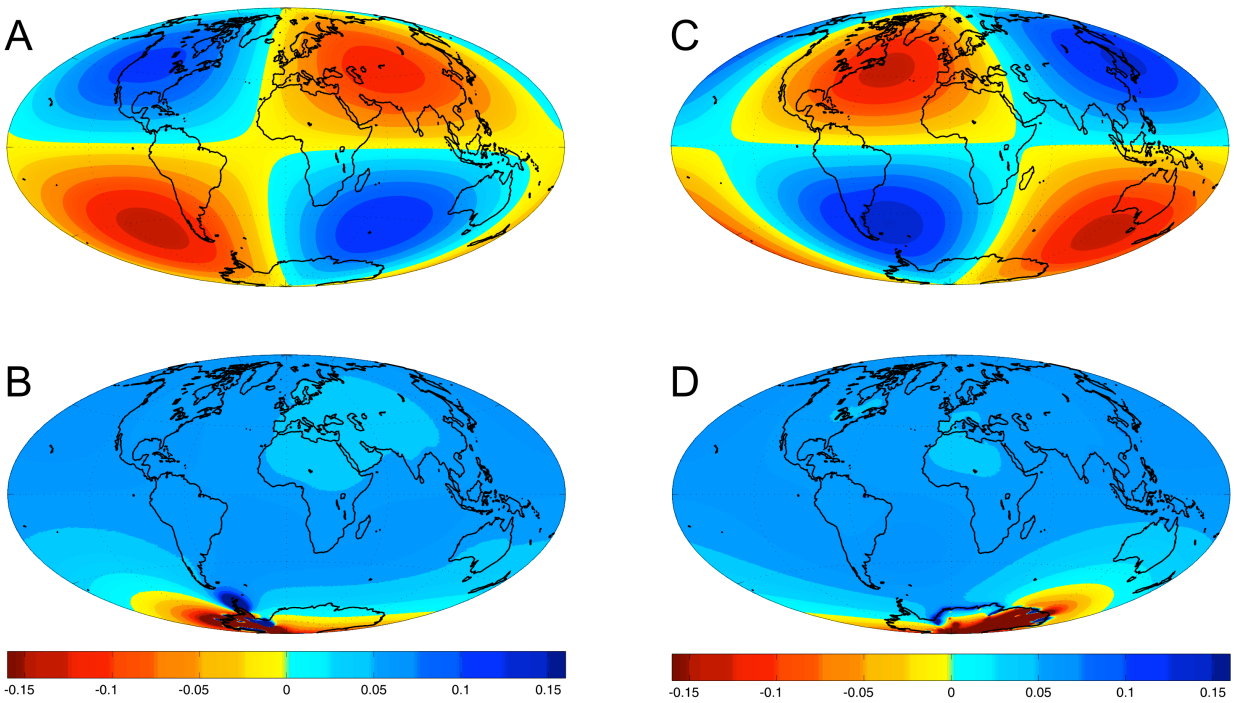

Figure 2.5: Decomposition of the difference between predictions of sea-level change due to the collapse of the WAIS based on the new and old sea-level theories (i.e., Figure 2.4C). Specifically, the difference is decomposed into contributions associated with (A) feedback due to Earth rotation and (B) the expulsion of water from uplifting and flooded marine-based sectors of the now-vanished ice sheet. (C) and (D), as in (A) and (B), except for the case of the EAIS and a decomposition of the difference plot shown in Figure 2.7C.

rotational effects, which are characterized by the same "quadrential" sea-level geometry [e.g., Milne and Mitrovica, 1996; Mound, 1998]. We explore this issue in detail in Figure 2.5A, where we isolate the contribution to the signal from rotational feedback. The figure shows the difference between a prediction based on the old theory (Figure 2.4B) and a second prediction, also based on the old theory, in which we add the contribution to sea-level change from perturbations in Earth rotation. In addition, Figure 2.5B shows the difference between a calculations based on the new theory (Figure 2.4A) and the old theory where we once again incorporate rotational effects; i.e., the figure plots the part of the discrepancy between the old and the new theory that is not explained by rotational feedback.

The physics of rotational feedback is outlined in Figure 2.6 and the associated caption. A reorientation of the rotation pole is accompanied by a rise in sea level in quadrants that the local pole (either the north pole in the northern hemisphere or the south pole in the southern hemisphere) is moving away from and a fall in sea level in antipodal quadrants. The maximum sea-level signal will be 45° from the poles. In our calculations the collapse of the WAIS leads to a shift in the rotation pole of 92 m per metre of effective eustatic sea-level rise (or $\sim$ 0.46 km for an EEV of 5 m); the direction of the polar wander is such that the south pole moves toward the West Antarctic (253°W longitude) and the north pole moves toward India (73° W). Accordingly, the maximum positive sea-level rise due to rotational feedback occurs over North America and the Indian Ocean (while the antipodal regions of sea-level fall occur in Asia and the southeast Pacific). This positive signal, which reaches a magnitude of 0.11 (or $\sim$ 0.6 m for an EEV of 5 m), is clearly responsible for a large part of the enhanced sea-level rise over North America and the Indian Ocean in Figure 2.4A relative to Figure 2.4B. Moreover, the contribution in Figure 2.5A is also responsible for the fact that the peak sea-level predictions obtained using the new theory (Figure 2.4A) occur closer to the U.S. coastlines than the calculations generated using the old theory (Figure 2.4B).

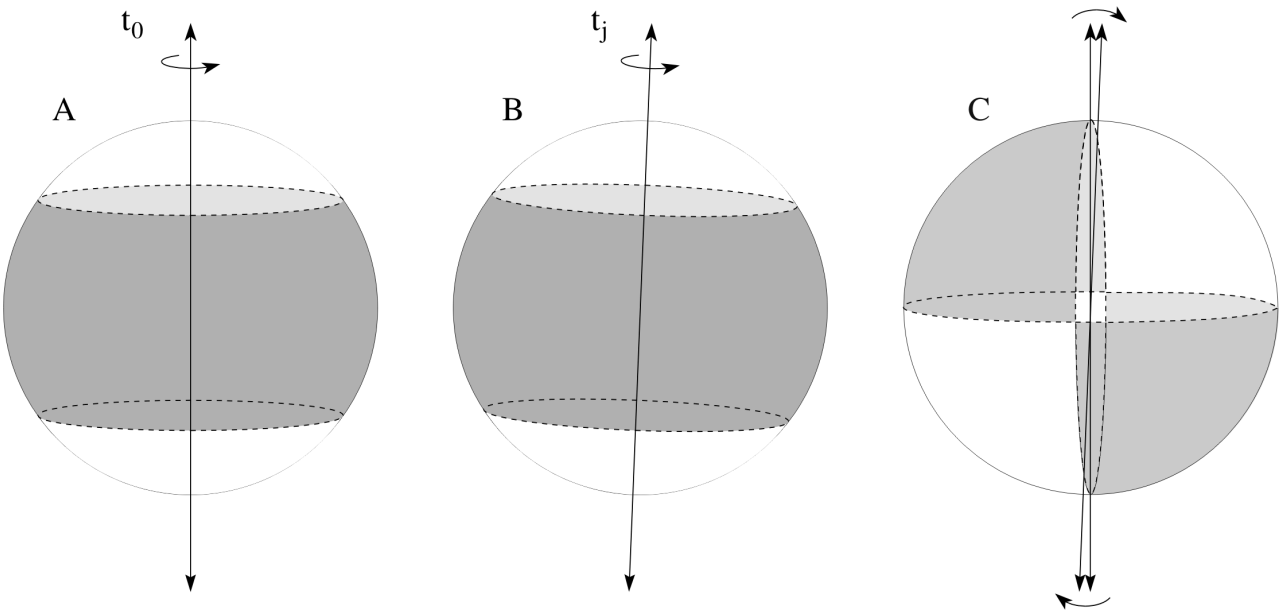

Figure 2.6: Schematic illustrating the geometry of the rotational feedback contribution to sea level. (A) and (B) show the orientation of the centrifugal potential for an Earth model prior to the melting event (t_0) and some time after the melting event (t_j), respectively. From t_0 to t_j the rotation pole, which was initially vertical, is assumed to have moved in a clockwise direction (compare frames A and B) relative to the solid surface of the planet. (C) shows the difference in centrifugal potential between the two frames (B minus A) associated with the true polar wander event. The geometry in frame (A) is given by the spherical harmonic degree two and order zero harmonic, while the perturbation in this potential, the so-called rotational driving potential, has a spherical harmonic degree two and order one (quadrential) geometry (frame C). The orientation in (C) is such that the driving potential is positive in quadrants that the local pole (N in the north and S in the south) is moving away from (shaded regions) and negative in the antipodal quadrants. The driving potential is zero along two great circles; the first is along the equator, and the second is perpendicular to both the first great circle and the great circle that defines the pole path. The driving potential is at a maximum 45° from the pole. The rotational feedback signal in sea-level has essentially the same geometry as the driving potential shown in (C), although the former is perturbed by loading effects.

The relatively large rotational feedback signal in response to the collapse of the WAIS may be surprising given that the location of the Antarctic, close to the pole, would seem to make any loading from the region a somewhat inefficient mechanism for driving polar wander. However, the centre of mass of the West Antarctic is $\sim 10^{\circ}$ from the south pole, and this displacement is clearly sufficient to drive a significant reorientation of the pole.

The second contribution that distinguishes the new predictions from the old, which is shown in Figure 2.5B, is more geographically uniform in the far-field of the West Antarctic. This contribution is primarily due to water being pushed out of the marine-based sector of the exposed West Antarctic as this region rebounds elastically in response to the melting. To investigate this issue, we re-plot, in Figure 2.7A, the total sea-level change driven by WAIS collapse (Figure 2.4A) in a new projection centred on the south pole. The figure shows that there is a significant fall in sea level within the West Antarctic, reaching ~ 17 times the amplitude of the EEV, driven by the radial uplift of the crust and the loss of gravitational attraction toward the now-vanished WAIS. In any marine-based sectors of the West Antarctic (i.e., in regions covered by water) this sea-level fall means that water is being pushed out of the region. The expulsion of water from these marine-based sectors is responsible for a normalized sea-level rise of $\sim$0.07 (or ~ 0.3 m for an EEV of 5 m in Figure 2.5B).

Over North America and the Indian Ocean the rotational feedback and water expulsion signals constructively interfere and the new sea-level theory predicts a (normalized) enhancement of the sea-level rise relative to old calculations [Clark and Lingle, 1977]. Over the southeast Pacific and Asia, where the two effects destructively interfere, the new theory predicts a somewhat smaller sea-level signal than the old calculation (Figure 2.4C).

Next, we turn to the case of the collapse of marine-based sectors of the EAIS (EEV=14.2 m). Figures 2.8A and B are predictions of the sea-level change just after this collapse based on the new sea-level theory (equations 2.21-2.23) and the older theory derived by Farrell and Clark [1976]

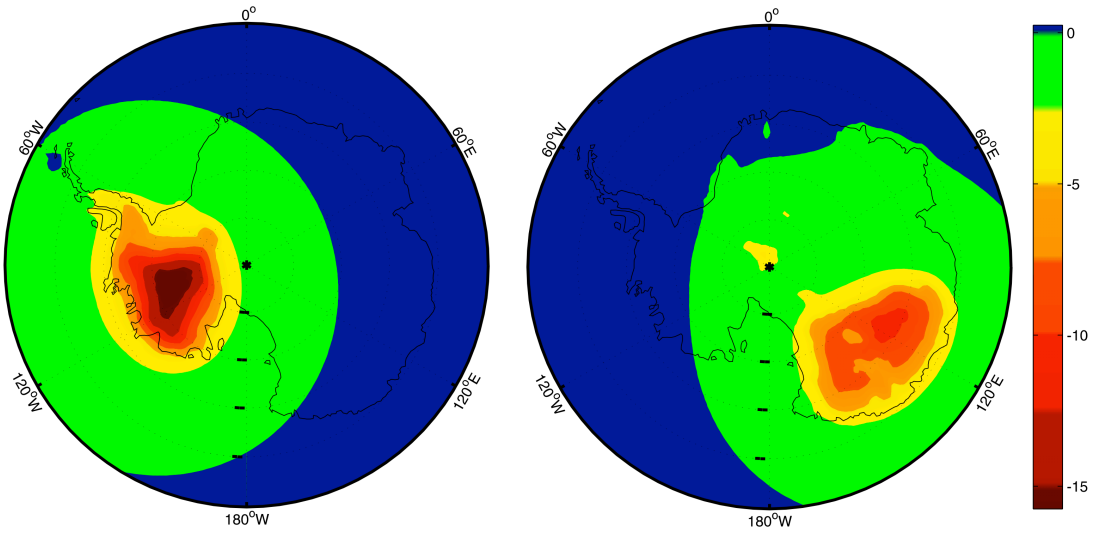

Figure 2.7: (A) A prediction of the change in sea level over the south pole following the collapse of the WAIS. The figure is a polar projection out to 60°S of the results plotted in Figure 2.4A. (B) as in (A), except for the case of a collapse of the EAIS (a polar projection of Figure 2.8A).

(equations 2.24-2.26), respectively. The difference between the two is shown in Figure 2.8C. The normalized sea-level rise computed using the new theory is increased by ∼0.2 in the northwest Pacific and the southwest Atlantic (which translates to a difference of ∼ 3 m if we use an EEV of 14.2 m), while it is reduced by ∼0.08 in the north Atlantic.

The origin of these differences is evident in Figures 2.5C and D, where we once again decompose the signal into contributions from rotational feedback (Figure 2.6) and water expulsion from the marine-sectors of the melting ice complex (Figure 2.7B). As in the predictions for WAIS collapse, the expulsion yields a relatively uniform sea-level rise over the far-field of the now-vanished ice sheet. The normalized amplitude of this signal is ∼0.07. A far more significant difference between the WAIS and EAIS collapse scenarios is the orientation of the rotational feedback signal (compare Figures 2.5A and C). Melting of the marine sectors of the EAIS leads to a displacement of the rotation pole of ∼ 102 m per metre of EEV. The direction of the displacement is such that the south pole moves toward Wilkes Land in the East Antarctic (specifically, along ∼ 131°E longitude)

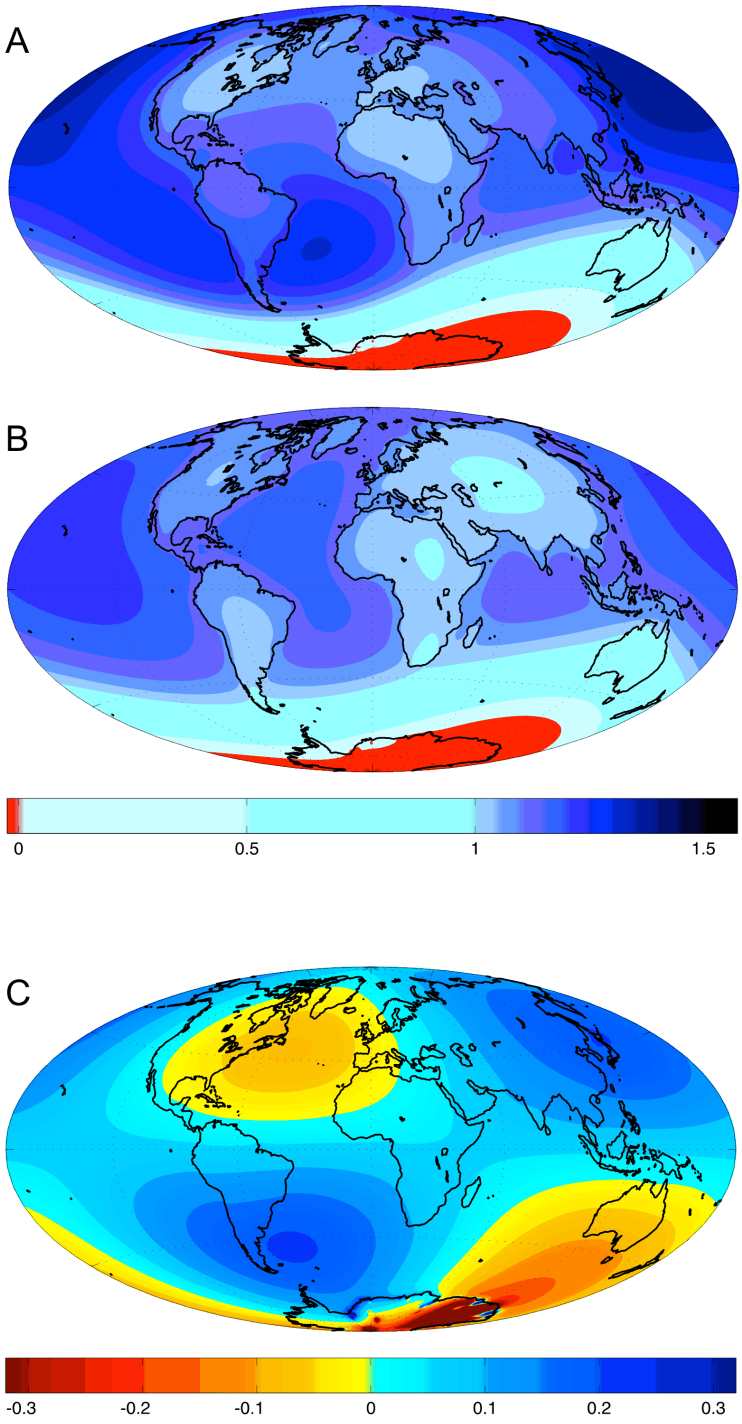

Figure 2.8: As in Figure 2.4, except for predictions based on a scenario where marine-based sectors of the EAIS collapse. In this case, the effective eustatic value used in the normalization of the results is 14.2 m. A decomposition of the difference plot (C) into contributions from rotational feedback and water expulsion from the uplifting marine-based sectors of the EAIS is shown in Figure 2.5C and D, respectively.

and the north pole moves along $\sim 49°$W longitude, or roughly toward Newfoundland. The resulting feedback signal is a sea-level fall over the north Atlantic and the south Indian Ocean and a sea-level rise in antipodal quadrants (Figure 2.5C), each with a (normalized) magnitude of 0.13. (This value is slightly higher than the amplitude in Figure 2.5A because marine sectors of the EAIS have a centre of mass that is slightly more distant from the south pole than the centre of mass of the WAIS.) Thus, for this melting scenario our new sea-level theory predicts a significantly enhanced sea-level rise over the north Pacific and the south Atlantic, where rotational feedback and expulsion constructively interfere, and a reduced sea-level rise over the north Atlantic, where the interference is destructive and the rotational effect dominates, relative to the old theory.

We note that polar motion driven by melting from the WAIS and marine sectors of the EAIS are roughly in opposite directions. As a consequence, if both melting scenarios were active and with similar EEVs then the total rotational feedback (the sum of Figures 2.5A and C) would have a significantly smaller amplitude than the individual feedback signals. In other words, in this case the common view that melting from the entire AIS would lead to relatively little net true polar wander (and sea-level feedback signal) would be correct.

Our focus, to this point, has been on the short-term, elastic response to rapid melting from either the WAIS or the EAIS sectors of Antarctica. In Figure 2.9 we show predictions of the change in sea level over a 500 year time window following this immediate elastic response. The calculations adopt the radial profile of mantle viscosity discussed above. As the system evolves forward from the short term response, the ongoing uplift of marine-based sectors of the vanished ice sheet would lead to a continued expulsion of water. However, the physics of viscoelastic adjustment is such that the associated rise in sea level is largely limited to areas just outside the zone of melting. Specifically, the subsidence of the "peripheral bulge" produces a ring of sea-level rise that accommodates much of the water migration due to expulsion. In the far-field oceans the change in sea level is more

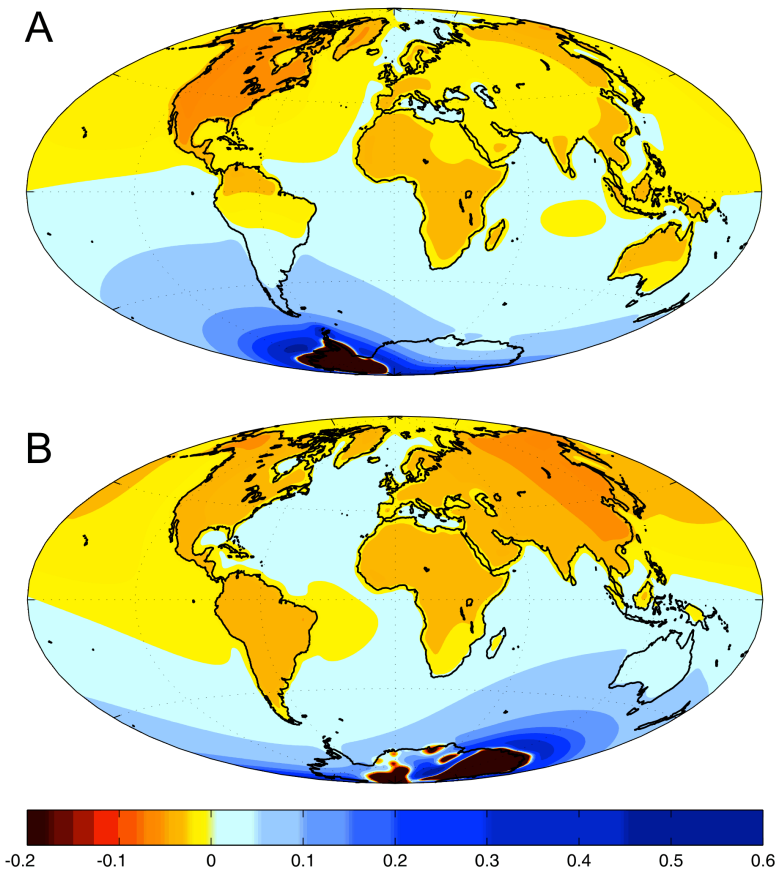

Figure 2.9: (A) Change in sea level, normalized by the effective eustatic value, in the 500 year period following the "elastic" sea-level fingerprint associated with WAIS melting shown in Figure 2.4A. The total sea-level change at this time is the sum of the two maps. (B) As in frame (A), except for the EAIS melting scenario considered in Figure 2.8A. The calculations in this figure, in contrast to those shown in Figures 2.4 and 2.8, are sensitive to the adopted radial profile of mantle viscosity. The profile we adopt is specified in detail in the text.

moderate, and the small trend from ocean to continent regions reflects both ocean loading effects (which tend to deflect the continents upward) and a superimposed rotational feedback. In any event, we conclude that the elastic fingerprints patterns described above (Figures 2.4 and 2.8) will not be altered significantly in the far-field of Antarctica in the centuries following any collapse of the ice sheets.

The goal of this section has been to provide updated predictions of the sea-level change that would follow any future collapse of various marine-based sectors of the AIS. As we have shown, an accurate prediction of this change, and in particular its geographic variation, requires a sea-level theory that includes self-gravitation of the surface mass load, deformation of the solid Earth, inundation and subsequent adjustment of marine-based sectors of the ice sheet, and the feedback into sea level of contemporaneous perturbations in the Earth's rotation.

We have been motivated, in part, by recent discussions of sea-level projections associated with the disappearance of the WAIS. As an example, Chapter 10 of the penultimate IPCC report cites a sea-level rise of 5 m in this case [Solomon et al., 2007], which is an estimate of the uniform rise in sea level within the global oceans after all depressions in marine sectors of the West Antarctic have been filled to sea level. We have coined the term "effective eustatic value" for this rise, to distinguish it from the eustatic value ($\sim$ 8 m) associated with the total volume of the WAIS. It has been important to note that the EEV ignores a prediction, now thirty years old, that demonstrated the significant geographic variation in sea level that would follow the melting event [Clark and Lingle, 1977]. Specifically, Clark and Lingle [1977] showed that load self-gravitation, and the associated adjustment of the crust, would lead to a dramatic migration of water from the near field to the far field of the melt zone; the net effect would be a sea-level fall in the vicinity of the melting, and a sea-level rise about 20% greater than the EEV in the far field. We have shown that the expulsion of water from marine-based sectors of the WAIS and rotational feedback are capable of increasing

this enhancement relative to the EEV by about a factor of two in regions where the two processes constructively interfere (e.g., the coastlines of North America and the Indian Ocean). In locations where the two processes destructively interfere, the net effect is a reduction in sea level relative to predictions based on the Farrell and Clark [1976] theory adopted by Clark and Lingle [1977] (Figure 2.4).

Similar conclusions can be drawn from our calculation in which all marine sectors of the EAIS disappeared (Figure 2.8). In this case, over the northwest Pacific and the south Atlantic, rotational feedback and water expulsion act in tandem to double the enhancement of sea-level rise (relative to the EEV) predicted using the theory of Farrell and Clark [1976]. In contrast, in the north Atlantic, where the two processes are of opposite sign, the net predictions based on the two sea-level theories are nearly equal.

The importance of water expulsion and rotation can be further illustrated by considering results for specific geographic sites, rather than simply comparing peak predictions based on the new and old theories (since these peaks predicted for each theory may not be located at the same place). In Table 2.1 we list normalized sea-level predictions for a set of 18 sites obtained using the two theories. The table includes results for both of the melting scenarios considered in this paper; namely, melting of the entire WAIS and all marine sectors of the EAIS. In the case of sites along the U.S. coast and WAIS collapse, the old theory predicts a normalized sea-level change of ~ 1.1, or a 10% enhancement above the effective eustatic value. In contrast, the new theory increases this enhancement by a factor of 2.5, or ~ 0.7 m of additional sea-level rise if we adopt an EEV of 5 m. In the case of the EAIS scenario, the old theory yields a sea-level change in southern South America (e.g., Santiago, Buenos Aires) of $\sim 6 - 7\%$ above the EEV, while this enhancement is increased by a factor of four (to 26-28%) when the new theory is adopted. A similar ($\sim 20\%$) increase in the normalized prediction is also evident in Japan between the old and new theories.

Table 2.1: Sea Level predicted at a selection of globally distributed sites.

Site	WAIS		EAIS	
	New Theory	Old Theory	New Theory	Old Theory
Vancouver	1.26	1.10	1.15	1.11
Portland	1.26	1.11	1.07	1.11
San Francisco	1.31	1.14	1.19	1.14
Los Angeles	1.29	1.13	1.17	1.13
Boston	1.27	1.12	1.08	1.11
New York	1.26	1.11	1.07	1.11
Washington	1.25	1.09	1.07	1.10
Savannah	1.26	1.11	1.12	1.11
Miami	1.29	1.14	1.16	1.15
Rio de Janeiro	1.02	1.01	1.29	1.11
Buenos Aires	0.82	0.85	1.28	1.06
Lima	1.05	1.09	1.25	1.12
Santiago	0.80	0.85	1.26	1.07
London	1.11	1.09	1.09	1.09
Lisbon	1.15	1.11	1.09	1.11
Chennai	1.11	1.11	1.23	1.10
Melbourne	1.07	0.99	0.60	0.68
Tokyo	1.16	1.16	1.38	1.17

We conclude that at many locations the rotational feedback and water expulsion contribute significantly more than load self-attraction, which has been the focus of many previous discussions of sea-level fingerprints, including the Clark and Lingle [1977] estimate of sea-level change following melting from the WAIS. In this regard we note that while rotational feedback would be active throughout the melting event, water expulsion would only be activated once marine-based sectors of ice disappear and inundation begins.

2.4 Results and Discussion of Post Glacial Sea-Level Changes

In this section we use the results of a suite of illustrative sea-level calculations to review in somewhat more detail the relevant physics of post-glacial sea-level change on longer timescales. We separate the contributions to sea-level change from current, rapid ice distribution changes (as discussed in Section 2.3) from ongoing sea-level changes due to past ice-sheet evolution. In particular, we simulate sea-level changes following two scenarios of ice-sheet retreat, one characterized by widespread ice loss and the other by local ice loss. The simulations are performed using the version of the sea-

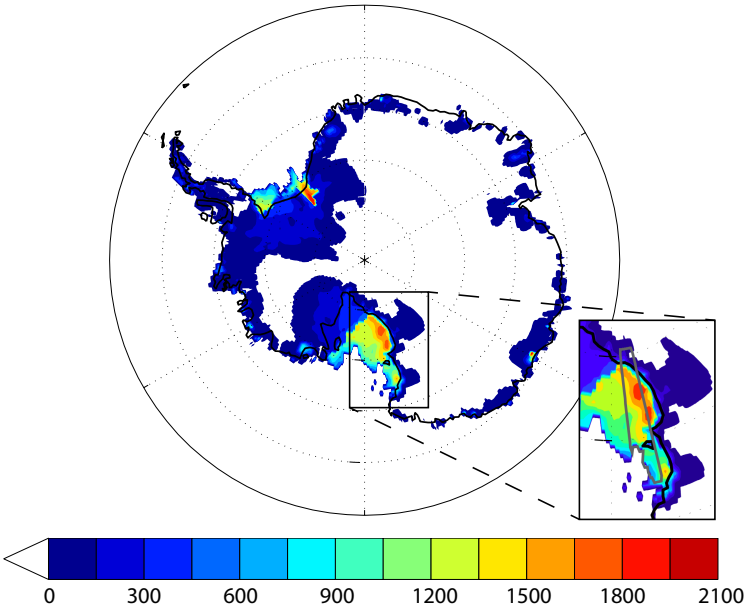

Figure 2.10: Pattern of ice loss considered in two illustrative ice-age sea-level simulation. Thickness of grounded ice loss (in meters) over the course of a 200 yr model melt phase involving widespread retreat of the Antarctic Ice Sheet. Inset: Area outlined in grey shows the thickness of grounded ice loss (in meters) over the course of a 200 yr model melt phase that provides a scenario of localized ice retreat within a small region near the Ross Ice Shelf.

level theory described in Section 2.2 valid for a gravitationally self-consistent, rotating, viscoelastic Earth model with migrating shorelines. In each scenario, we alter the ice geometry rapidly in a single, 200 year time step at the start of the simulation and then hold the ice distribution constant for 10,000 ky. Sea-level changes are predicted every 200 years after the ice-melting event.

To begin, consider the widespread ice loss across the AIS depicted in Figure 2.10. This ice geometry was constructed by taking the difference in ice distribution between 11 ka and 10 ka predicted in simulation of the AIS through the last deglaciaion using the Pollard and DeConto [2012b] ice-sheet model that we discuss in Chapter 6. There is an associated loss of grounded ice of 90,000 km^3, equivalent to 1.78 m of globally averaged sea-level rise (after account is taken of water inundation into Antarctic marine sectors freed of ice at 10 ka).

Figure 2.11A shows a global map of the sea-level change immediately following the melting event

and Figure 2.11B shows the same field focused on Antarctica. On this short timescale, deformation of the Earth can be considered purely elastic, so the second and fourth terms in equation 2.55 which describe the viscous components of the sea-level perturbations can be neglected and the physical effects discussed in Section 2.3 drive the sea-level changes. As in Figure 2.4A, the pattern of sea-level change is dominated by a large sea-level fall in the vicinity of ice melt (i.e., the near-field) driven by gravitational effects and elastic rebound of the solid surface, and a sea-level rise at distance from the ice sheet (i.e., the far field) that reaches up to $\sim 30\%$ higher than the global average. Ocean loading and a signal due to load-induced perturbations in Earth's rotation vector also contribute to the spatial variability of the sea-level change [see Section 2.3, Mitrovica et al., 2011].

Figures 2.11C and 2.11D show the sea-level change predicted over the 10 ky period following the instantaneous sea-level response plotted in Figures 2.11A and 2.11B. (Note, once again, that there is no change in ice geometry during this time period.) In this case, the sea-level change is strongly dominated by viscous deformation of the solid Earth in response to the unloading of ice and loading of melt water (with associated gravitational and rotational effects). Mitrovica and Milne [2002] have summarized the various physical effects that contribute to this pattern of sea-level change and we review these effects here. There is an ongoing, large amplitude sea-level fall in regions that experienced ice loss as the solid surface viscously rebounds towards isostatic equilibrium. The nearby surrounding areas experience a sea-level rise as subsidence occurs at the periphery of regions of ice loss. These effects are described on the left side of the schematic in Figure 2.12A and its caption. The location and amplitude of the peripheral subsidence is sensitive to both the geometry of ice loss and the Earth model. In the far-field, there is a broad region of relatively small amplitude sea-level fall due largely to the migration of water towards the Antarctic to fill the accommodation space created within peripheral regions experiencing subsidence (see right side of

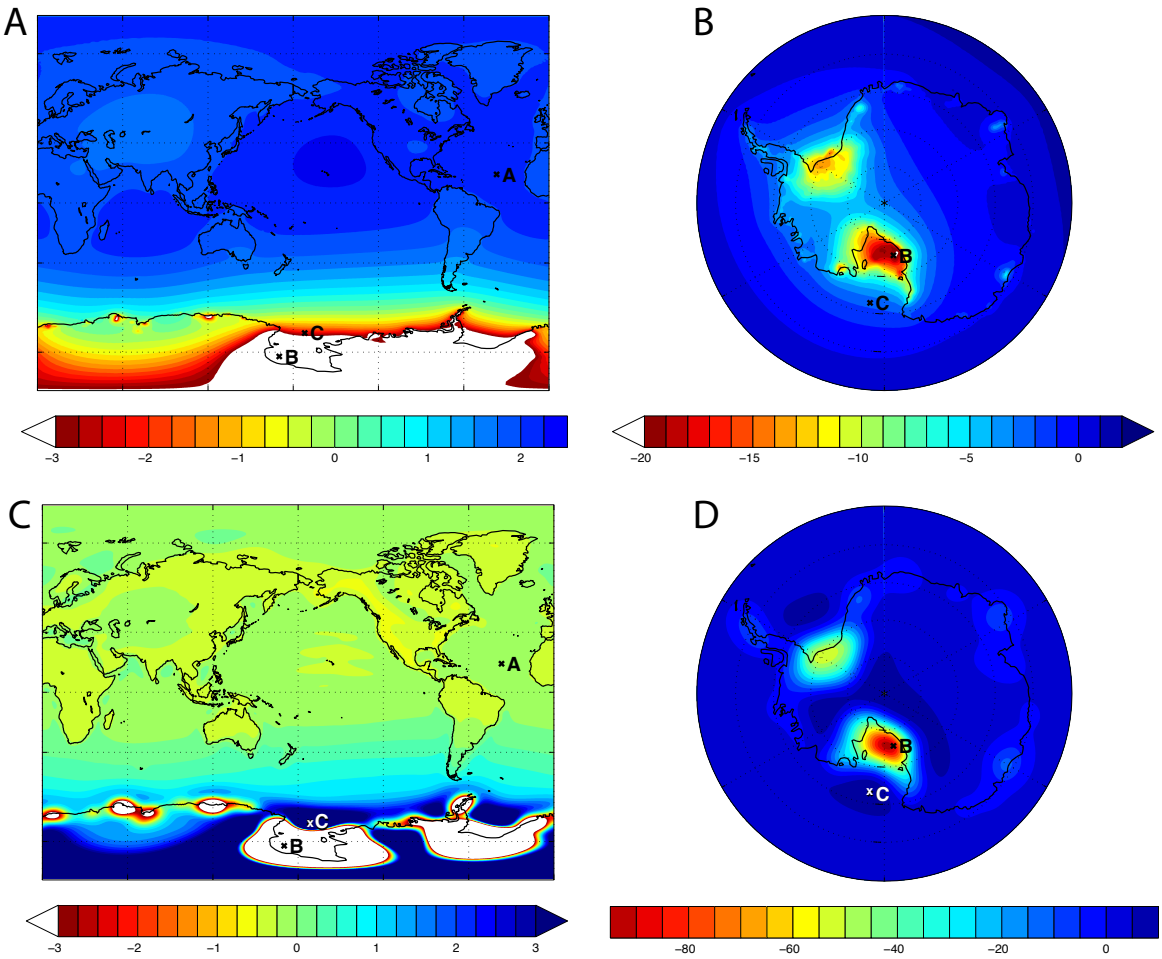

Figure 2.11: Initial and subsequent (long term) patterns of sea-level change following the ice loss scenario shown in Figure 2.10. (A, B) Sea-level change immediately following the rapid loss of grounded ice depicted in Figure 2.10, plotted globally (A) and local to the Antarctic (B). (C, D) Total sea-level change in the 10 ky period following the initial sea-level perturbation, plotted globally and locally (D). No ice loss occurs during this latter 10 ky time period. Labels 'A', 'B' and 'C' refer to the locations of the time series plotted in Figure 2.13.

schematic in Figure 2.12A). This process is known as ocean syphoning [Mitrovica and Milne, 2002]. There is additional spatial variability in the far-field associated with the viscous effects of meltwater loading, including a tilting of the crust at continental margins, as illustrated in Figure 2.12B. This so-called continental levering [Nakada and Lambeck, 1989; Mitrovica and Milne, 2002] is reflected in a thin offshore zone of sea-level rise; the accommodation space created by this deformation also contributes to ocean syphoning [Mitrovica and Milne, 2002].

In Figure 2.13, we plot time series of the total sea-level change (blue curves), as well as the radial displacements of the sea surface (green curves) and solid surface (red curves) relative to their positions at the start of the simulation. Each column corresponds to a different site, as labeled on the maps in Figure 2.11. These sites sample, from left to right in Figure 2.13, the far-field, near-field and the peripheral bulge (labeled 'A', 'B' and 'C', respectively, on the maps in Figure 2.11).

Within the far-field (Figure 2.13A), the majority of the initial sea-level jump is due to a rapid rise in the sea surface as meltwater is added to the ocean. Subsequently, there is a gradual fall in sea level as a drop in the sea surface height due to syphoning outpaces the ocean load-induced subsidence of the solid surface. For the site within the region of ice loss (Figure 2.13B), there is an instantaneous sea-level fall of 19.4 m immediately following the melt event. This is comprised of a 6.2 m drop in the sea surface due to the loss of gravitational attraction toward the ice, and a 13.2 m rise of the solid surface due to elastic rebound. The subsequent sea-level fall ($\sim$ 170 m in 10 ky) is almost entirely due to viscous relaxation of the solid Earth towards isostatic equilibrium. There is also a small sea surface height increase at this location due to the gradual relaxation of the initial gravitational perturbation as the solid surface rebounds. Finally, the site at the periphery of the melt event (Figure 2.13C) initially experiences a sea-level fall due to a combination of gravitational and (elastic) deformational effects. Subsequently, as the region experiences crustal subsidence due to the adjacent ice unloading, and sea surface uplift due to the weakening of the initial gravitational

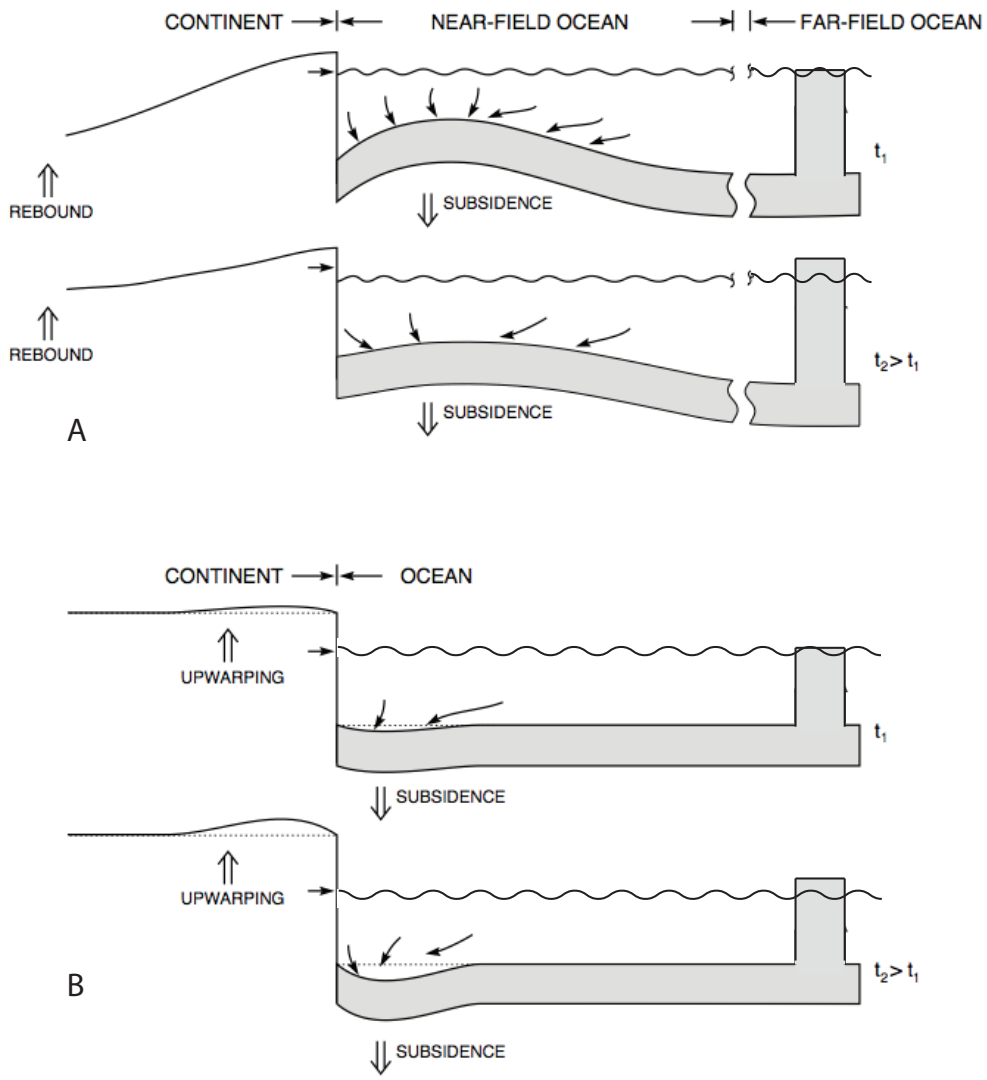

Figure 2.12: Schematic taken from Mitrovica and Milne [2002] with minor modifications illustrating the physics of post-glacial sea-level changes. Frame (A) illustrates post glacial rebound (left), peripheral bulge subsidence (middle) and ocean syphoning of equatorial regions (right). Frame (B) illustrates the continental levering effect caused by ocean loading (left) and the associated sea-level fall in open ocean regions (right).

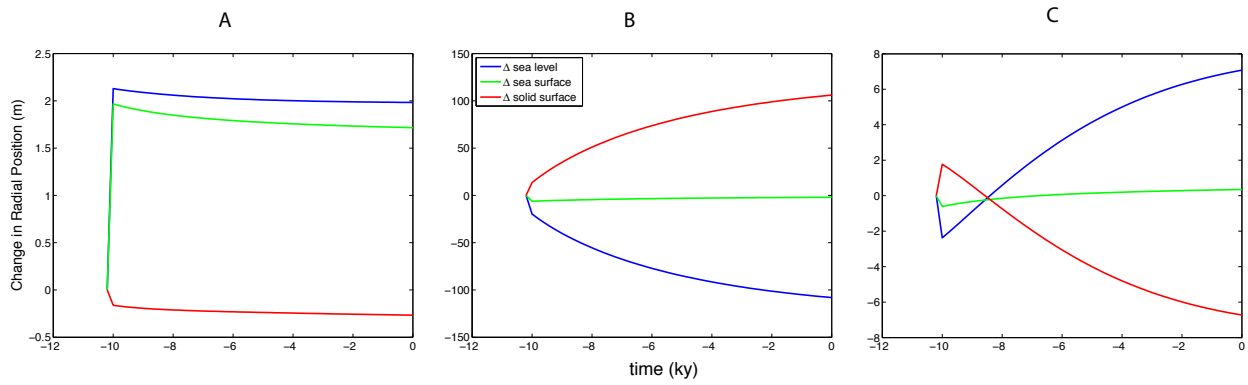

Figure 2.13: Total change in sea level and the surfaces bounding sea level at specific sites following the ice loss scenario in Figure 2.10. (A) Change in sea level (blue), sea surface (green) and solid surface (red) heights as a function of time computed for the far-field (subtropical North Atlantic) site labeled 'A' in Figure 2.11A. Sea surface and crustal heights are defined relative to the center of the Earth. (B) same as Figure 2.13A, except for the site within the region of ice loss (western Ross Ice Shelf) labeled 'B' in Figure 2.11B. (C) same as in Figure 2.13A, except for the site at the periphery of the ice loss region (outer Ross Sea) labeled 'C' in Figure 2.11.

perturbation, the site experiences a monotonic sea-level rise.

Next, we consider results (Figure 2.14) for the localized melting scenario shown in Figure 2.10 (inset), in which only a small sector near the Ross Ice Shelf experiences ice loss. In this case, the melt event involves a change in ice volume of ∼11,000 km^3, equivalent to a global average sea-level rise of 0.11 m when accounting for the inundation of marine sectors freed of ice. The physical effects active in this scenario are the same as those in the first scenario. Note that while the volume of meltwater is an order of magnitude smaller than in the scenario of Figure 2.10, the sea-level fall within the region of melting is significant on both short and long timescales. For example, the site labeled 'B' in Figure 2.14B experiences an initial sea-level fall of 9 m, comprised of a 2.5 m drop in the sea surface height and a 6.5 m (elastic) uplift of the solid surface. Over the subsequent 10 ky, sea level falls an additional 80 m at this site (Figure 2.14D).

The results described in this section highlight the strong geographic variability and temporal complexity in sea-level change following an ice melting event. This complexity becomes even more

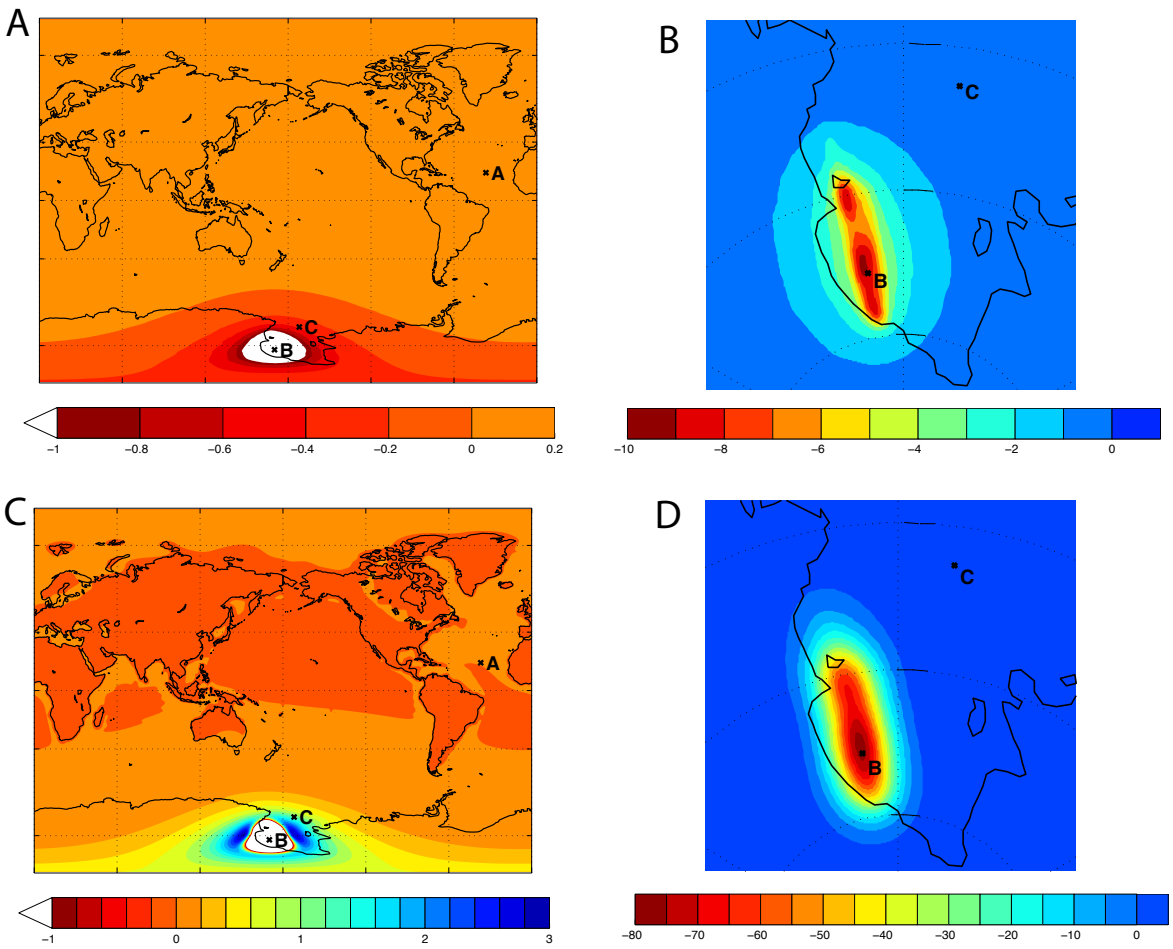

Figure 2.14: Initial and subsequent (long term) patterns of sea-level change following the ice loss scenario shown by the grey box in the inset of Figure 2.10. Format as in Figure 2.11, except frames (B) and (D) are further zoomed in on the region of ice loss. This scenario involves ice loss localized to an area near the Ross Ice Shelf.

pronounced as the ice sheet evolves and the loci of melting vary in space and time. In Chapters 3, 5 and 6 we present simulations of ice-sheet retreat through the entire deglaciation phase of an ice-age cycle. In these simulations, at any given time during the ice-sheet retreat, the total predicted sea-level change is a combination of a short timescale signal governed by the total ice melt and a viscous signal associated with the full history of ice melting.

Chapter 3

Laurentide-Cordilleran Saddle Collapse as a Contribution to Meltwater Pulse 1A

3.1 Introduction

There is growing recognition that the last deglaciation phase of the Ice Age was punctuated by a series of meltwater pulses associated with the rapid collapse of ice sheet sectors and catastrophic drainage of proglacial lakes [e.g., Fairbanks, 1989; Barber et al., 1999; Clark et al., 2002; Deschamps et al., 2012; Törnqvist and Hijma, 2012]. The most prominent example is Meltwater Pulse 1A (mwp-1A), which involved ∼20 meters of globally averaged sea-level rise in under 500 years at around 14 ka [Deschamps et al., 2012].

The source or sources of mwp-1A are uncertain and controversial. It has been assumed that retreat of the Laurentide Ice Sheet [Kennett and Shackleton, 1975; Fairbanks et al., 1992], in particular the southern sector of the ice sheet [Leventer et al., 1982; Keigwin and Jones, 2010; Andrews et al., 1994; Peltier, 2004], dominated the meltwater flux. However, a significant southern Laurentian source for mwp-1A is inconsistent with oxygen isotope records from the Gulf of Mexico [Carlson, 2009]. Moreover, analysis of sea-level records across the mwp-1A time window at Barbados and Sunda Shelf rule out a sole Southern Laurentide source [Clark et al., 2002; Bassett, 2005]. The

This chapter is in preparation for submission with Lauren Gregoire, Jerry X. Mitrovica and Tony Payne.

fingerprinting study of Clark et al. [2002] suggests either globally distributed sources for mwp-1A or a dominant contribution from the Antarctic Ice Sheet. The latter scenario is supported by climate modeling [Weaver, 2003], analyses of far-field sea-level records during the post-mwp-1A time period [Bassett, 2005], and a fingerprinting study including newly collected sea-level data from Tahiti [Bard et al., 2010]. In contrast to these analyses, ice-sheet modelling studies indicate that the excess volume of the Antarctic Ice Sheet at Last Glacial Maximum (LGM) relative to the modern was smaller than previously believed, equivalent to a globally averaged sea-level change of 5-9 meters, which implies a relatively minor contribution from the AIS to mwp-1A [Whitehouse et al., 2012a; King et al., 2013; Ivins et al., 2013; Gomez et al., 2013].

Recently, Gregoire et al. [2012] modeled the retreat of the Laurentide Ice Sheet (LIS), the Cordilleran Ice Sheet (CIS) and the Greenland Ice Sheet (GIS) from the Last Glacial Maximum to the present day. They concluded that the collapse of the ice saddle between the LIS and CIS may have been responsible for a significant component of mwp-1A. The consistency of this scenario with observations of sea-level change across the mwp-1A time window have not been explored. In this chapter we compute the post-LGM geometry of sea-level change associated with the deglaciation model of Gregoire et al. [2012] and compare these results with available sea-level records from Barbados, Sunda Shelf and Tahiti.

3.2 Methods

We compute post-glacial sea-level changes using the gravitationally self-consistent theory described in Chapter 2 [Kendall et al., 2005] that accounts for viscoelastic deformation of the solid Earth, time-dependent shorelines, including the influx of water into sectors freed of marine ice, and the feedback into sea level of perturbations in Earth rotation. We adopt a 1-D (depth varying) Maxwell Earth model with a spherical harmonic truncation at degree and order 256. The elastic and density

structure of the Earth model is prescribed by the seismic model PREM. We consider two different radial profiles of mantle viscosity. The first, the VM2 model of Peltier [2004], which is associated with the ICE5G global ice history reconstruction, is characterized by an elastic lithosphere of thickness of 90 km, upper mantle viscosity close to 5×10^{20} Pa s, and a lower mantle viscosity that remains close to $2 - 3 \times 10^{21}$ Pa s. The second, henceforth model LM, has a lithospheric thickness of 120 km, and upper and lower mantle viscosities of 5×10^{20} Pa s and 5×10^{21} Pa s, respectively. The latter model has been preferred on the basis of independent analyses of ice-age data sets (e.g., Lambeck et al., 1998; Mitrovica and Forte, 2004).

We normalize the sea-level predictions presented below using the effective eustatic value of sea-level change (EEV) associated with the Gregoire et al. [2012] deglaciation model. As defined in Chapter 2, the EEV is defined as the globally uniform shift in sea level equal to the meltwater volume, after the latter has been corrected for marine-based sectors that are exposed by the melting ice sheets [Gomez et al., 2010b]. In practice, we compute the EEV using the full sea-level theory that accounts for migrating shorelines described, but we do so on a rigid Earth fixed to modern topography, with rotational and gravitational effects turned off.

The Gregoire et al. [2012] model for the LIS, CIS and GIS extends from 21,000 (Last Glacial Maximum) to present and we compute post-glacial sea-level changes across this entire period. Figure 3.1A shows the meltwater flux associated with changes in grounded ice over a time window that encompasses the collapse of the ice saddle between the LIS and CIS. The flux peaks at ~ 0.30 Sv during this interval, with a background flux of $\sim$0.1-0.15 Sv. Figure 3.1B and 3.1C show snapshots of the ice cover at 11.8 ka and 11.3 ka of model time, which bound the main phase of saddle collapse. The ice saddle collapse across this interval is located in northwestern Canada, but ice cover also thins in the vicinity of Hudson Bay. Gregoire et al. [2012] suggest that the model time window of 11.8-11.3 ka, which corresponds to an EEV of 10.47 m, should be interpreted as coinciding with

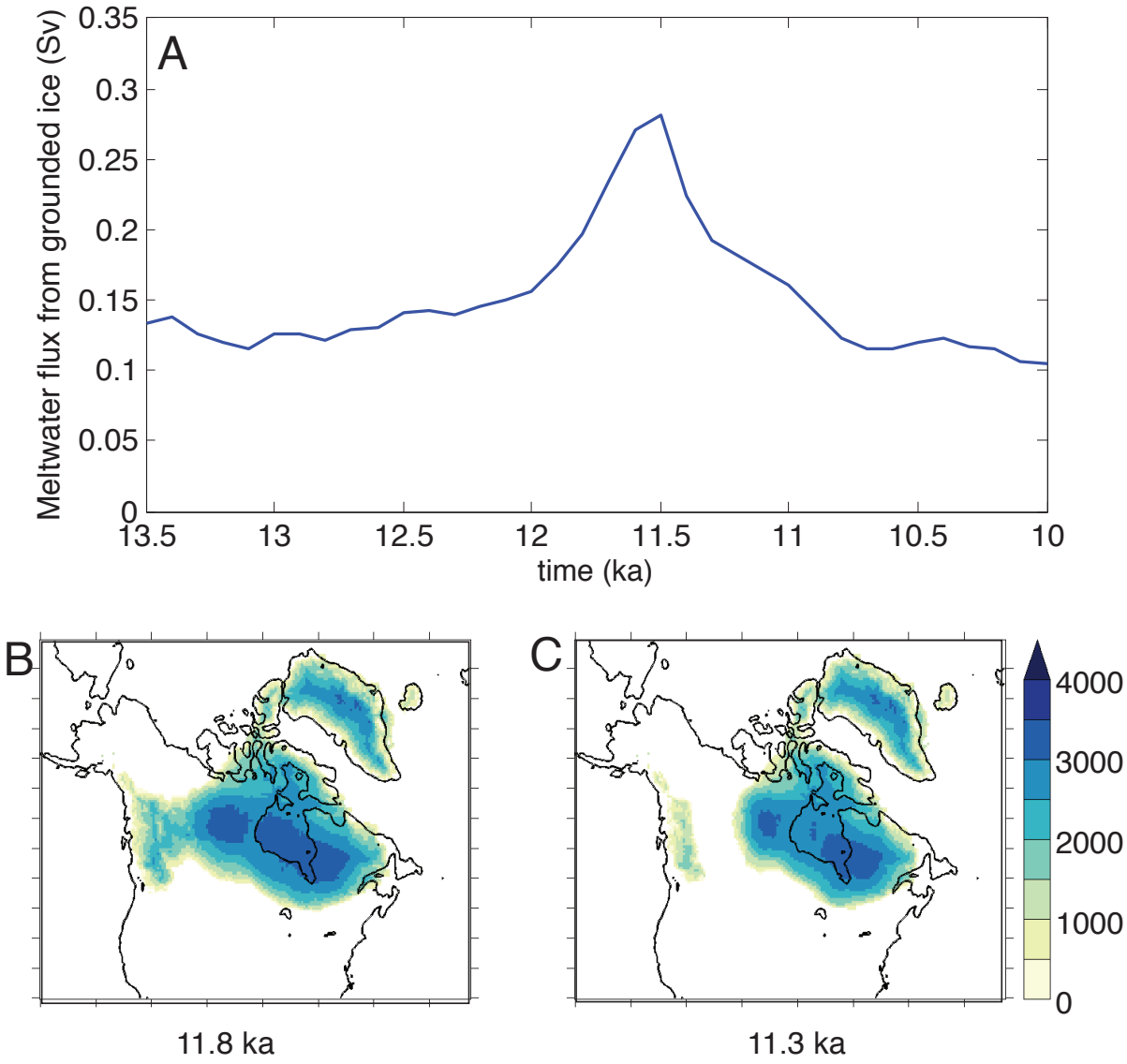

Figure 3.1: The Gregoire et al. [2012] model of Laurentide, Cordilleran and Greenland Ice Sheet evolution through the Meltwater Pulse 1A event. (A) Meltwater flux from grounded ice (in sverdrups) as a function of model time (in ky) before, during and after the ice saddle collapse event they associate with mwp-1A. (B-C) Snapshots of grounded ice thickness over North America near the start (B) and end (C) of the saddle collapse.

the main phase of mwp-1A (i.e., ∼14 ka) on the basis that the timing of mwp-1A is consistent with geochronological constraints on the opening of an ice-free corridor between the LIS and CIS.

3.3 Results

We begin with an analysis of the global geometry of sea-level change predicted during the mwp-1A event. Figure 3.2A shows the normalized sea-level fingerprint for the saddle collapse across the 11.8-11.3 ka time window of the Gregoire et al. [2012] model computed using the VM2 viscosity model. Figure 3.2B shows the same field in the vicinity of the saddle collapse and resolves the near field structure of the fingerprint. The general physics of such fingerprint was discussed in detail in Chapter 2. Gravitational and deformational effects associated with a rapid ice mass loss produce a large sea-level fall in the vicinity of the melt zone, and a greater than average sea-level rise in the far field. Ocean meltwater loading leads to a subsidence of the sea floor and a gradient in the computed sea-level change close to shorelines. Finally, the surface mass redistribution causes the Earth's rotational pole to shift towards the center of mass of the ice loss, contributing to the azimuthal asymmetry evident in the sea-level fingerprint.

Since we are considering the sea-level change across a finite time interval in Figure 3.2A and B, there may be a contribution to the prediction from viscous effects associated with the full time history of the deglaciation up to 11.3 ka. We quantify this contribution in Figures 3.2C and D, where the former is the normalized sea-level change across the 11.8-11.3 ka time window computed assuming a purely elastic response of the solid Earth to the change in the surface mass load, and the latter is the difference between the total signal (frame A) and the elastic signal (frame C). That is, Figure 3.2C represents the usual sea-level fingerprint computed by including only elastic deformation (henceforth the "elastic fingerprint"), while Figure 3.2D represents the departure from this fingerprint associated with the viscous response across the 500 yr time window associated with

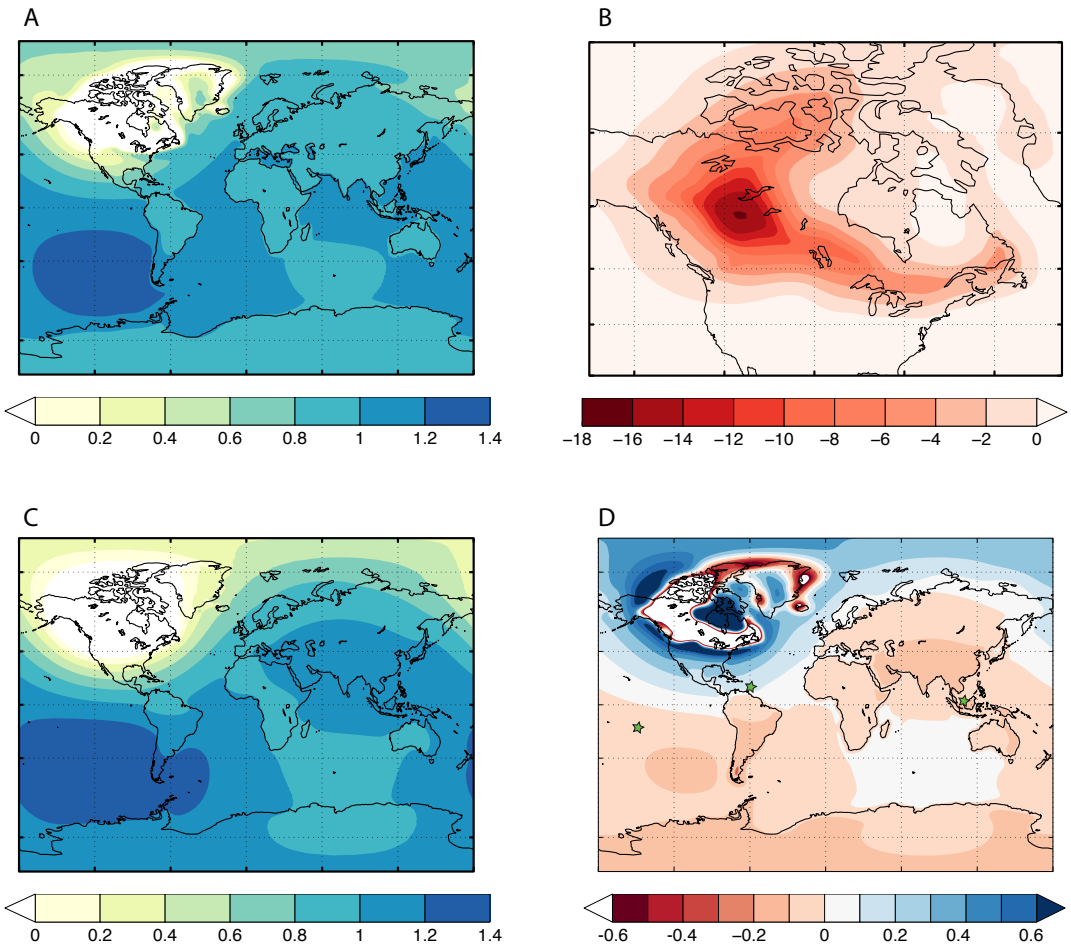

Figure 3.2: (A) Normalized sea-level fingerprint computed for the saddle collapse between 11.8-11.3 ka in the deglaciation model of Gregoire et al. [2012]. (B) As in (A), except the plot focuses on the near field of the ice collapse. (C) Normalized sea-level fingerprint computed assuming only elastic deformation of the Earth. (D) The difference between frames (A) and (C), isolating the contribution to the computed sea-level change due to viscous deformation. The green stars in frame (D) indicate the location of (from left to right): Tahiti, Barbados and Sunda Shelf.

the full time history of the surface load changes between 21 ka (LGM) and 11.3 ka.

In the vicinity of the regions of ice loss, the elastic fingerprint is characterized by widespread uplift that extends well beyond the margins of the ice loss. Note, in this regard, the extended and smooth zone of sea-level fall in Figure 3.2C relative to Figure 3.2A. The difference between

these two global fingerprints reflects the contribution from viscous effects of smaller spatial scale, including post-glacial uplift and subsidence of peripheral bulge regions (the blue zones in Figure 3.2D). Note that the signal from peripheral bulge subsidence extends to Central America, where it leads to a $\sim 10 - 15\%$ augmentation of the elastic sea-level fingerprint at Caribbean Island sites.

Next, consider the signal associated with viscous adjustment at locations beyond the peripheral bulges, in the so-called far-field of the ice loss. Several physical effects contribute to this signal. First, the shift in the orientation of the Earth's rotation axis associated with viscous deformation of the solid Earth gives rise to a sea-level signal with quadrential (spherical harmonic degree two, order one) geometry (Figure 3.2D). This signal is characterized by sea-level fall in the southeast Pacific and Asia, and sea-level rise in the Indian Ocean and across North America. (As discussed in Chapter 2, ongoing surface mass redistribution and the associated elastic deformation also gives rise to a signal associated with rotational feedback, which is apparent in Figure 3.2C.) Second, a background migration of water out of the far-field and into the regions experiencing peripheral bulge subsidence leads to a large-scale drop in sea-surface height (and thus sea level) in Figure 3.2D. This effect is commonly termed "ocean syphoning" [Mitrovica and Milne, 2002]. Finally, ongoing viscous adjustments associated with the full history of ocean loading since LGM produce a gradient in the predicted sea-level change near shorelines in Figure 3.2D, contributing a sea-level fall onshore and a sea-level rise offshore that is termed "continental levering" [Mitrovica and Milne, 2002]. These three effects combine to produce a sea-level fall in equatorial and southern ocean regions that can reach $\sim 10\%$ of the sea-level rise associated with the elastic fingerprint.

As discussed in the Introduction (Section 3.1), constraints on the change in sea-level across the mwp-1A event exist at three sites: Barbados, Tahiti and Sunda Shelf (shown by the stars on Figure 3.2D). Deschamps et al. [2012] estimate the sea-level jump associated with mwp-1A to be 16 ± 4 m at Barbados and 17 ± 5 m at Tahiti. They refined the latter range to 16 ± 2 m on the basis of

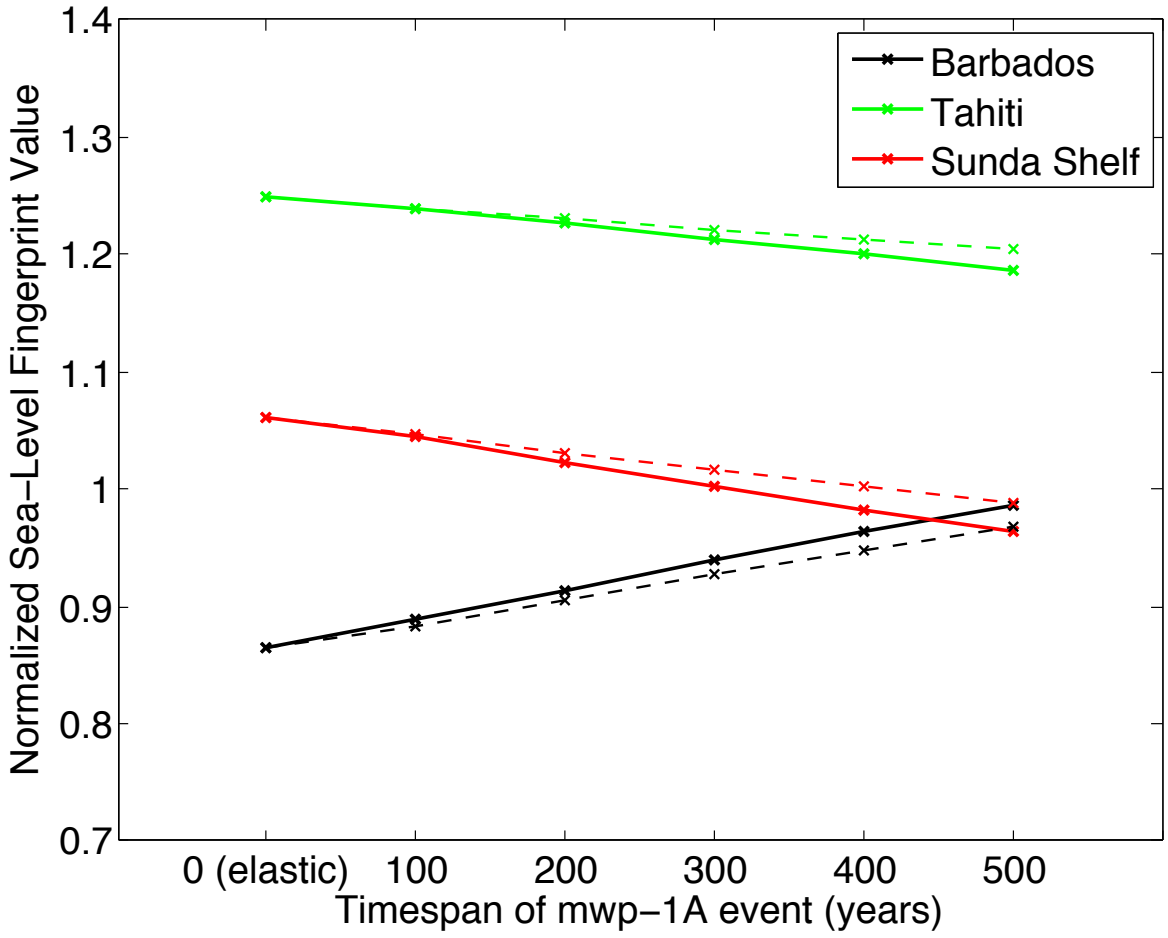

Figure 3.3: Normalized sea-level fingerprints at Barbados, Tahiti and Sunda Shelf (as labeled) computed for the mwp-1A event in the Gregoire et al. [2012] reconstruction as a function of the assumed duration of the event (see text). Calculations were performed using both the VM2 (solid lines) and LM (dashed lines) viscosity profiles.

several lines of argument. The original study of the Sunda Shelf record concluded that the sea-level jump across mwp-1A was up to 16 m at this site [Hanebuth et al., 2000]. However, recent work by Liu and Milne [pers. comm.], which accounts for the fact that the mwp-1A event is bounded by data collected at different sites, suggests that the sea-level rise associated with mwp-1A at Sunda Shelf was 12 ± 3 m.

It is clear from the results in Figure 3.2D that the viscous component of sea-level change can have a significant impact on predictions of the sea-level rise associated with the mwp-1A event. However, this contribution will depend on the duration of the event, which is uncertain. Deschamps et al. [2012] concluded, on the basis of the Tahiti record, that mwp-1A took place in less than $\sim$350 years. Moreover, since the ice-sheet model employed by Gregoire et al. [2012] does not accurately capture the timing of the saddle collapse, the modeled duration of the event may also be suspect. To address this uncertainty, we have repeated the fingerprint calculation in Figure 3.2 for a suite of simulations in which the total change in ice volume between 11.8-11.3 ka (EEV = 10.47 m) was applied over progressively shorter time windows ranging from 500 ky (as in Figure 3.2A) to 0 ky (as in Figure 3.2C). The ice history from 21 ka to 11.8 ka was unchanged in all the simulations. Predictions of the normalized fingerprint at the Barbados, Sunda Shelf and Tahiti computed for this sequence of calculations is shown in Figure 3.3, where the solid and dashed lines are predictions based on the VM2 and LM viscosity profiles, respectively.

The predictions at all three sites vary linearly as the duration is increased from zero (the purely elastic case) to 500 ky. (That is, the perturbation in the normalized fingerprints associated with viscous effects increases linearly with time over the range of durations considered in Figure 3.3.) Barbados sits on the peripheral bulge of the saddle collapse and thus, as discussed above, viscous effects contribute a sea-level rise at this site. In contrast, viscous adjustments contribute a sea-level fall at Tahiti and Sunda Shelf, which are in the far-field of the saddle collapse. We note that the

magnitude of the signal due to viscous adjustments is relatively insensitive to the adopted viscosity model for the range of timestands treated in Figure 3.3.

Clark et al. [2002] computed the sea-level fingerprint for the case of a collapse of the southern sector of the Laurentide Ice Sheet and the magnitude of the sea-level signal they computed at Sunda Shelf was $\sim$ 50% greater than the prediction at Barbados. The inconsistency between this prediction and the observed jump in sea-level across mwp-1A at these two sites, which are of comparable amplitude (12 $\pm$ 3 m and 16 $\pm$ 4 m, respectively), led them to conclude that this sector of the Laurentide Ice Sheet could not have been the sole source for the meltwater pulse. This conclusion was reinforced by the Tahiti record obtained by Deschamps et al. [2012] (a 16 $\pm$ 2 m jump across mwp-1A) since a southern Laurentide source for mwp-1A would produce a sea-level rise there that was $\sim$ 70% greater than at Barbados, which is inconsistent with the observations. In contrast to this scenario, an Antarctic source for mwp-1A would lead to comparable sea-level rise at all three sites [Clark et al., 2002], and is thus consistent with all of the observations [Deschamps et al., 2012].

How does the Gregoire et al. [2012] model of saddle collapse between the Laurentide and Cordilleran Ice Sheets perform in this regard? The sea-level fingerprint associated with this model is consistent with the observation of a comparable jump in sea-level across mwp-1A at Barbados and Sunda Shelf as long as the event occurred over a time span of $\sim$300 yr or more (Figure 3.3). The progressive improvement in the fit to these observations, as one moves from a duration of zero (the elastic case) to 300 yr or more, is a result of viscous adjustments which, as noted above, raise sea level within the peripheral bulge (Barbados) and lower sea level in the far-field (Sunda Shelf) of the saddle collapse (see Figure 3.2). For a mwp-1A duration of 300-500 yr, the saddle collapse scenario predicts a sea-level jump at Tahiti that is $\sim$ 20% greater than the jump at either Barbados or Sunda Shelf, which cannot be ruled out on the basis of the uncertainty in the observations at

the three sites. We conclude that the scenario may have been a significant, and indeed dominant, contribution to mwp-1A.

3.4 Final Remarks

We have computed sea-level changes associated with the Gregoire et al. [2012] model of the evolution of the Laurentide, Cordilleran and Greenland Ice Sheets since the LGM. Our results show that a saddle collapse between the LIS and CIS yields a fit to the observed sea-level jump across mwp-1A at Barbados, Sunda Shelf and Tahiti that is comparable to the fit obtained assuming a sole Antarctic source and significantly better than the fit predicted for a scenario in which the southern sector of the Laurentide Ice Sheet is the sole source of the event. It is, of course, possible that a combination of saddle and AIS collapse may have dominated mwp-1A.

A reduction of the AIS contribution to mwp-1A would bring this estimate into accord with inferences of excess ice volume in the Antarctic Ice Sheet during the LGM [e.g., Whitehouse et al., 2012a; King et al., 2013; Ivins et al., 2013; Gomez et al., 2013]. Any further refinement of the constraints on the source(s) of mwp-1A will require additional high-resolution sea-level records for the mwp-1A event. As a final point, our analysis suggests that viscous effects cannot be neglected if the duration of mwp-1A exceeded a few centuries. Therefore, future studies of sea level during this important period of ice-sheet instability and mass flux should not assume a purely elastic deformation response of the solid Earth.

Chapter 4

Sea level as a stabilizing factor for marine-ice-sheet grounding lines

The potential for climate change to destabilize marine ice sheets poses uncertainty for projections of future sea-level rise [Oppenheimer, 1998; Solomon et al., 2007; Vaughan, 2008; Smith et al., 2009]. An instability mechanism, whereby ice-sheet thinning or rising sea level leads to irreversible retreat of the grounding line, is widely predicted for marine ice sheets resting upon reversed bed slopes [Weertman, 1974; Thomas and Bentley, 1978; Schoof, 2007a; Katz and Worster, 2010]. However, existing analyses of this instability mechanism have not accounted for deformational and gravitational effects that lead to a sea-level fall (rise) at the margin of a rapidly shrinking (growing) ice sheet [Mitrovica et al., 2001; Plag and Juettner, 2001; Gomez et al., 2010b, see Chapter 2]. In this chapter, we present a suite of predictions of gravitationally self-consistent sea-level change following grounding line migration. These predictions vary the initial ice-sheet size and also consider the contribution to sea-level change from various sub-regions of the ice sheet. Using these results, we revisit a canonical analysis of marine ice-sheet stability [Weertman, 1974] and demonstrate that sea-level changes local to the grounding line contribute a stabilizing influence on ice sheets grounded upon reversed bed slopes. We conclude that accurate treatments of sea-level change should be

A version of this chapter was published with Jerry X. Mitrovica, Peter Huybers and Peter Clark in the journal Nature Geoscience, vol 117, F01013, 2010.

incorporated into analyses of past and future marine ice-sheet dynamics.

Weertman [1974] derived the following equation governing the grounding line position L of a simple, two-dimensional, marine-based, steady state ice sheet (see Figure 4.1A):

$$\beta L + D_o = GL^{2/9}, \tag{4.1}$$

where β and D_o are initial, pre-loaded values for the bed slope (positive values denote increasing depth in direction of ice flow), and the minimum depth of the bed, respectively. With suitable choices for the accumulation rate, flow parameters, etc., the constant G equals 22.7 $\mathrm{m}^{7/9}$. Physically, the left-hand-side of this equation represents sea level at the grounding line, $D(L)$, where the ice is at the critical flotation thickness. The right-hand-side of the equation describes the ice thickness (in terms of an equivalent thickness of water) required such that accumulation of ice balances mass flux across the grounding line.

The solution of Equation (4.1) for various parameter choices is illustrated in Figure 4.1B. As an example, the case of $D_o = 200$ m and $\beta = 0$ leads to one steady state solution (blue circle) while increasing β to 0.4 m/km yields two steady state solutions (red, green circles). On the figure we adopt the terms "unstable" or "stable" following the arguments of Weertman [1974], which we summarize here. Consider the steady state given by the green dot in Figure 4.1B. If the ice sheet grows by some incremental amount, δL, then sea level at the new grounding line would be too high for ice flux across the grounding line to be balanced by accumulation of ice through the interior (i.e., the dashed red line falls above the solid black line at $L + \delta L$). Specifically, the ice loss will be greater than accumulation and the ice sheet will shrink, ultimately returning to its original steady-state position. Similarly, if we perturb the ice sheet by making L slightly smaller, sea level at the grounding line will be smaller than the value required to balance ice loss and accumulation, and

the ice sheet will grow until it returns to its original configuration. Hence, this particular steady state is stable. In contrast to this case, consider the steady state given by the red dot in Figure 4.1B. If the ice sheet grew by some incremental amount then sea level at the grounding line would be smaller than the thickness needed to balance accumulation and ice loss and the ice sheet would continue to grow instead of returning to its original configuration. Similarly, if the grounding line were perturbed to a smaller value, the ice sheet would continue to shrink. Hence, this steady state is considered unstable.

In general, if the slope of the curve describing sea level at the grounding line is greater than the slope of $GL^{2/9}$ at a point of intersection, the ice sheet is in stable steady state; the ice sheet is unstable if the reverse is true. Whenever the initial bed slope, β, is less than or equal to zero, the solution is unconditionally unstable, and a small retreat (advance) of the ice margin would lead to greater mass loss (gain) across the grounding line than accumulation and thus further retreat (advance). This result is the basis for Weertman [1974]'s conclusion that the model ice sheet is inherently unstable when it rests on a bed that was flat or sloped downwards inland prior to loading.

One shortcoming of Weertman [1974]'s argument regarding stability is that it invokes a time-dependent perturbation of the system within an otherwise steady state framework. For example, the bedrock topography is assumed to be in hydrostatic equilibrium with the ice load, even when the margin is advancing or retreating. Recent analyses have extended the Weertman [1974] treatment to account for, among other features, non-steady state conditions [Schoof, 2007a,b; Katz and Worster, 2010]. These studies have concluded that the condition that an ice sheet on a reversed bed slope is unstable applies to the observed, rather than the pre-loaded topography.

A second shortcoming of Weertman's analysis is the assumption that sea level at the grounding line remains constant as the size of the marine ice sheet is perturbed. Previous analyses have considered the influence of a sea-level perturbation (dD) on ice-sheet stability by assuming a ge-

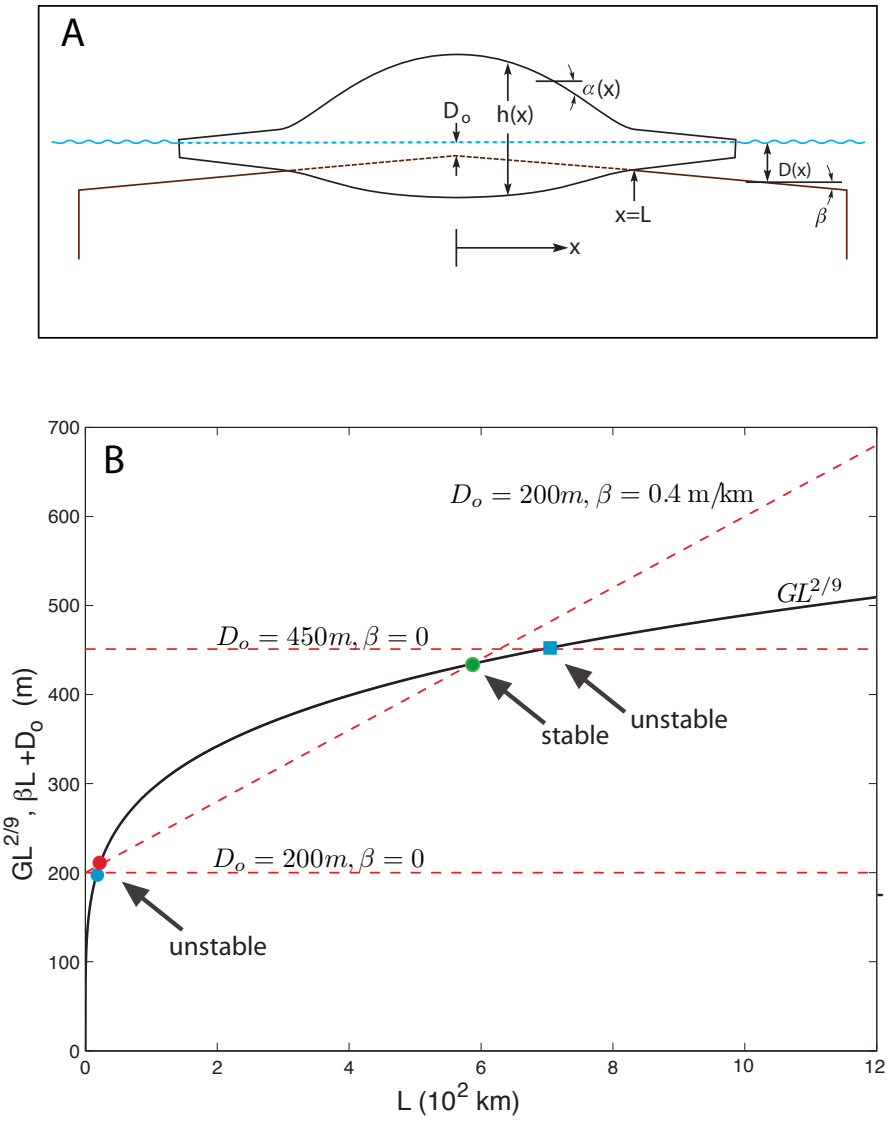

Figure 4.1: A summary of the Weertman analysis of ice-sheet stability. (A) Vertical cross section through the two-dimensional, marine-based ice sheet considered by Weertman [1974]. The radial dimension is denoted by x, where $x = L$ is the grounding line. The ice sheet of thickness $h(x)$ is in isostatic equilibrium and sits on bedrock initially inclined with slope β, where positive β denotes a bedrock depth that increases as one moves outward. D_o denotes the pre-loaded depth of the bedrock at the center of the ice sheet, and α is the slope of the upper ice surface. (B) Plot of solutions for grounding line position according to Weertman [1974]'s steady state marine ice-sheet stability theory. The figure shows $GL^{2/9}$ versus grounding line position L (black line) and $\beta L + D_o$ versus L for various D_o and β values (red lines, as labelled). The intersections between the $GL^{2/9}$ curve and the straight lines (denoted by red, green and blue circles and blue square) are solutions to Equation (4.1) and they therefore represent possible steady state marine ice-sheet configurations. The terms "stable" and "unstable" that appear on the figure are defined in the text.

ographically uniform, or eustatic, change in sea level [Thomas and Bentley, 1978; Hindmarsh and Le Meur, 2001; Schoof, 2007a; Wilchinsky, 2009]. Under this assumption, a decrease in ice mass, with an associated change in L, leads to an increase in sea level at the grounding line (Figure 4.2A). The assumption of eustasy is roughly consistent with Weertman's assumption of hydrostatic equilibrium in the sense that adjustments in ice mass over very long time scales will maintain isostatic equilibrium and thus lead to sea-level changes that are nearly uniform geographically (in the absence of a lithosphere that maintains elastic strength over very long periods). However, isostatic equilibrium will not be maintained for ice-mass changes over time scales ranging out to tens of millennia, so that eustasy will generally be an inadequate description of changes in sea level, particularly near the ice sheet itself.

Gravitationally self-consistent sea-level (GSCSL) changes following rapid melting of grounded ice are, in fact, characterized by markedly non-uniform spatial patterns [Mitrovica et al., 2001; Plag and Juettner, 2001; Gomez et al., 2010b, Chapter 2]. As discussed in Chapter 2, the departure from eustasy is due to three effects: (1) elastic deformation of the solid Earth in response to the load redistribution, including a rebound of the solid Earth in the vicinity of the diminishing ice load; (2) load self-gravitation, which primarily involves the migration of water away from the melting ice sheet as its gravitational pull on the ocean weakens; and (3) the feedback of contemporaneous, load-induced perturbations in the orientation of the Earth's rotation vector onto sea level. A GSCSL theory that combines these effects [Gomez et al., 2010b; Kendall et al., 2005, Chapter 2] predicts near-field sea-level changes in the opposite direction, and an order of magnitude larger, than would be predicted assuming eustasy (see Figure 4.2A).

The GSCSL predictions presented below are computed using the sea-level equation and pseudo-spectral algorithm given in Chapter 2 (Equations 2.21-2.23) [see also Mitrovica and Peltier, 1991; Kendall et al., 2005; Gomez et al., 2010b], with truncation at spherical harmonic degree and order

512. We use a version of the theory valid for a one-dimensional (depth varying), elastic Earth model. The elastic and density structure of the Earth model is prescribed by the seismic model PREM [Dziewonski and Anderson, 1981], with this structure embedded in the elastic Love numbers discussed in Section 2.2.2.

Consider an ice sheet with initial length $L_o = 700$ km that undergoes mass loss whose profile is consistent with that assumed by Weertman [1974], i.e., maintaining a steady state surface profile. In this case, each kilometre of inward migration of the grounding line is associated with 0.30 m of sea-level fall (Figure 4.2A). More generally, the predicted GSCSL change at the grounding line ranges from 0.20 to 0.34 m/km for grounding line positions L ranging from 265 km to 1400 km. This relative insensitivity occurs because the ice loss is largest at the margins and tapers off into the ice sheet and because the computed sea-level change at the grounding line is progressively less sensitive to ice-mass changes at greater distance.

This issue is explored in more detail in Figures 4.2B and 4.2C, which show the contribution to the GSCSL change from ice-mass changes within successively broader sub-regions of the ice-sheet-wide perturbation considered in Figure 4.2A. In Figure 4.2B, the sea-level change is plotted as a function of the fractional extent of ice-mass changes, as measured from the initial grounding line (see caption). As an example, in the case $L_o = 700$ km, and mass changes confined to the outer 25% of the ice sheet, sea level changes by 0.24 m/km, or 80% of the ice-sheet-wide case. Figure 4.2C accounts for tapering of the ice loss from the margin to the interior by plotting the sea-level change as a function of the fractional cross-sectional area of the mass change, as measured from the initial grounding line. In the $L_o = 700$ km case, for example, the 0.25 fractional extent that yields a sea-level change of 0.24 m/km corresponds to a fractional cross-sectional area of 0.5.

These sea-level results may be combined with the bed slope at the grounding line to compute an effective topographic slope. As an example, the grounding line of an ice sheet rapidly retreating

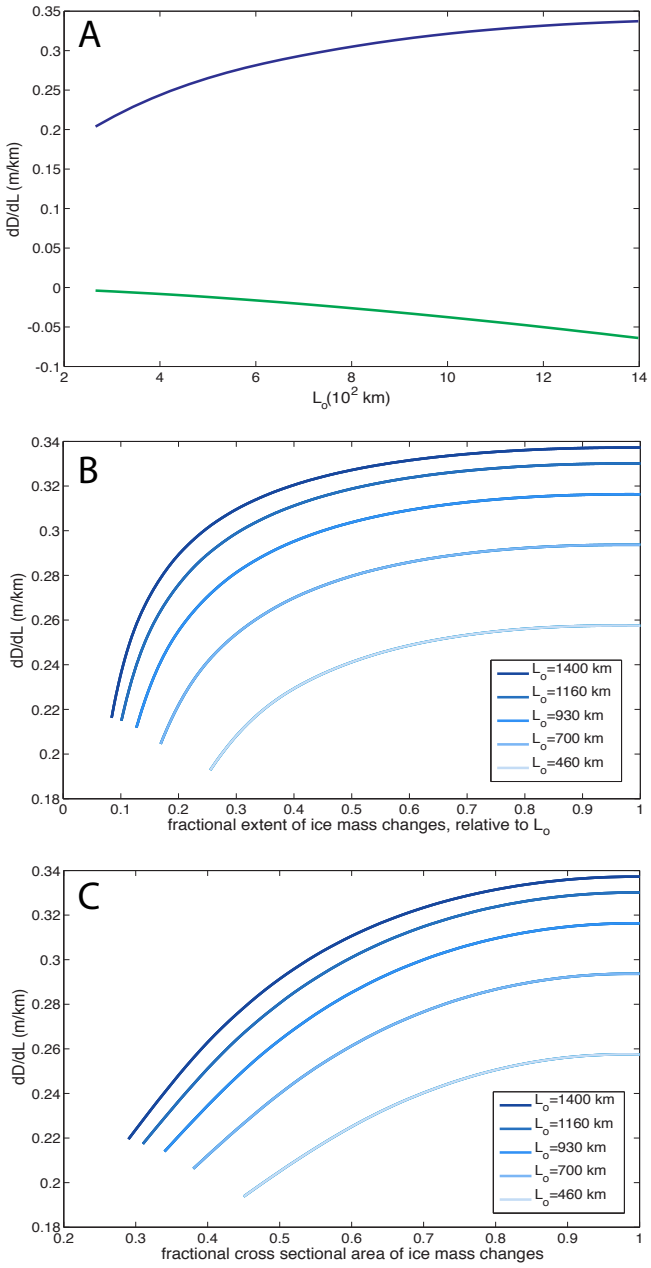

Figure 4.2: Sea-level changes following grounding line migration. (A) Change in sea level at the grounding line divided by the change in the grounding line position, i.e., dD/dL, plotted as a function of the initial grounding line position L_o. Green curve: A calculation which assumes a geographically uniform (eustatic) meltwater redistribution. Blue curve: A gravitationally self-consistent sea-level calculation (see text). These calculations assume that the ice sheet maintains a steady state surface profile as the grounding line migrates. (B), (C) Contributions to the GSCSL change (blue line) in (A), as a function of the fractional extent or fractional cross-sectional area, respectively, of the total ice load change in frame (A). As an example, an x-axis value of 0.2 in frame (B) means that only mass change within a distance from the grounding line that is 20% of L_o is included. An x-axis value of 0.2 in frame (C) means that only 20% of the total cross-sectional area of melting in frame (A) that is closest to the grounding line is included.

on a flat bed will actually be subject to an effective topographic slope of 0.3 m/km (up toward the center of the ice sheet) if the retreat reflects an ice-sheet-wide mass loss (Figure 4.2; this effective slope is as a result of the elastic uplift of the solid Earth due to the (ice plus water) unloading and the fall of the local sea surface arising from the associated loss in gravitational attraction. Both processes act to stabilize the retreat of the grounding line.

Under what conditions would the sea-level feedback mechanism stabilize an ice sheet resting on a reversed bed slope? A preliminary answer to this question is possible by replacing, as we discussed above, the pre-loaded slope β in Equation (4.1) with the observed slope, which we denote as β', and by adding an expression for the change in sea level that accompanies migration of the grounding line:

$$\beta' L + D_o + dD(L, dL) = GL^{2/9}. \tag{4.2}$$

Specifically, $dD(L, dL)$ is the change in sea level due to a shift of the grounding line from L to a new position, $L + dL$. For small changes in grounding line position, δL, away from some reference value L_o, we can rewrite the additional term as

$$dD(L_o, \delta L) = \delta L \left.\frac{dD}{dL}\right|_{L=L_o}. \tag{4.3}$$

We note that $\beta' + dD/dL$ represents the effective topographic slope at L_o, as defined above.

Figure 4.3 revisits the $D_o = 450$ km, flat bed solution in Figure 4.1 (blue square) using the extended stability Equation (4.2). Under the assumption that the migration of the grounding line is accompanied by a eustatic sea-level change, the instability we previously noted in the context of Figure 4.1 is exacerbated. (That is, the slope of the green line is even lower than the slope of the black.) The inclusion of a eustatic sea-level change perturbs the marine ice sheet toward a more unstable state. In contrast, if we incorporate a GSCSL change into the stability theory, a retreat

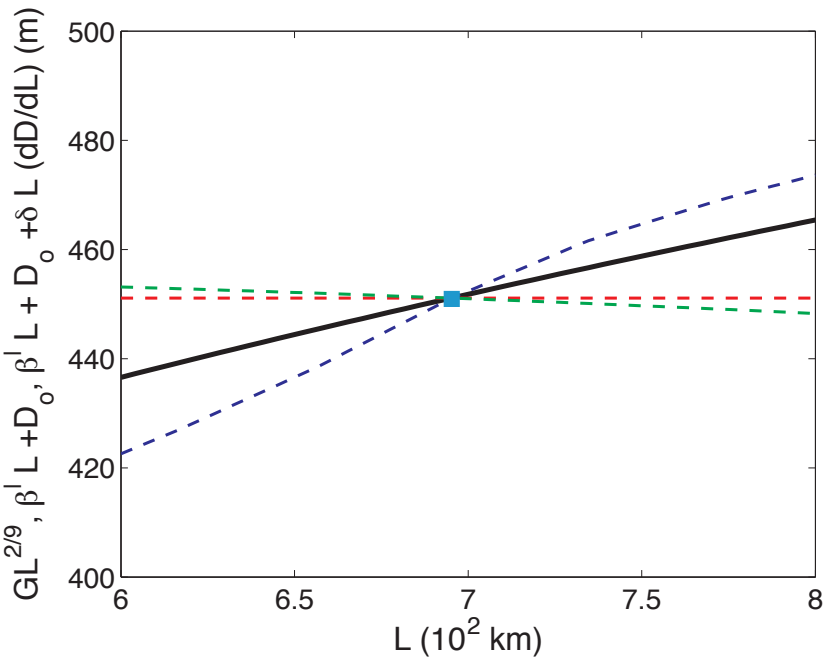

Figure 4.3: Revised analysis of marine ice-sheet stability based on a theory (Equation 4.2) that includes GSCSL change. The figure specifically considers the steady state, flat bed ice-sheet configuration denoted by the blue square ($D_o = 450$ km; $L_o \sim 700$ km) on Fig. 4.1B. The solid black and dashed red lines are reproduced from that figure. The dashed green and blue lines represent the total sea level at the grounding line computed by including either an ESL or GSCSL change (see text), respectively, associated with a perturbation in ice-sheet size from the steady state configuration (i.e., the left-hand-side of Equation 4.2). That is, we compute the term $dD(L_o, dL)$ as a function of the change in the grounding line position, $dL = L - L_o$, away from the value L_o while maintaining a steady state surface profile and add this to the red dashed line.

of the grounding line from the original steady state position ($L_o \sim 700$ km) will lead to a fall in sea level at the grounding line, a reduction of the flux across the grounding line, and an advance of the ice sheet back to its original configuration. The marine ice sheet will thus be stable. We conclude that local sea-level change following rapid grounding line migration will contribute a stabilizing influence on marine ice sheets, even when grounded upon beds of non-negligible reversed slopes, i.e., $\beta' < 0$.

In Figure 4.4, we use the results in Figure 4.2 to explore the impact of the sea-level stabilization mechanism within a parameter space defined by ice sheet size, melt geometry and bed slope. The

goal is to identify more generally the conditions under which sea-level change may be a significant stabilizing factor for marine based ice sheets. We begin by defining the "critical bedslope" as the bed slope at the grounding line for which an ice sheet transitions between stable and unstable states. Figure 4.4A (black curve) plots the critical bed slope as a function of initial grounding line position L_o, determined from Weertman [1974]'s Equation (4.1). The curve indicates that positive initial bed slopes can also be unstable; whereas horizontal or reverse initial bed slopes guarantee instability regardless of the size of the ice sheet.

Next, we calculate the critical bedslope using Equation (4.2) by incorporating either the ESL or GSCSL changes under the assumption that the ice-mass perturbation geometry maintains a steady-state surface profile (as in Figure 4.2A). The former (green line) illustrates the moderate destabilizing effect of ESL changes. The latter demonstrates the stabilizing influence of the local GSCSL changes that will accompany grounding line migration. Ice sheets with a spatial scale greater than $\sim$ 350 km can be stable over a range of negative bed slopes. As an example, in the case of $L_o = 700$ km, the critical bed slope is -0.15 m/km.

In Figs 4.4B and C we explore the contribution to the critical bed slope from ice-mass changes within successively broader sub-regions of the ice-sheet-wide zone considered in Figure 4.4A; in this case, we make use of the sea-level changes computed in Figs 4.2B and C. In Figure 4.4B, the critical bed slope is plotted as a function of the fractional extent of ice-mass change, as measured from the initial grounding line. As an example, in the case $L_o = 700$ km, mass flux that occurs within a zone that covers the outer 2% of the ice sheet length L_o produces a sea-level change that yields a critical bed slope of -0.1 m/km, or 65% of the ice-sheet-wide case. More generally, this same fractional extent of melting yields a critical bed slope that is negative for any ice sheet of spatial scale greater than $\sim$ 500 km. In Figure 4.4C we plot the critical bed slope as a function of the fractional cross sectional area of the mass change, as measured from the initial grounding

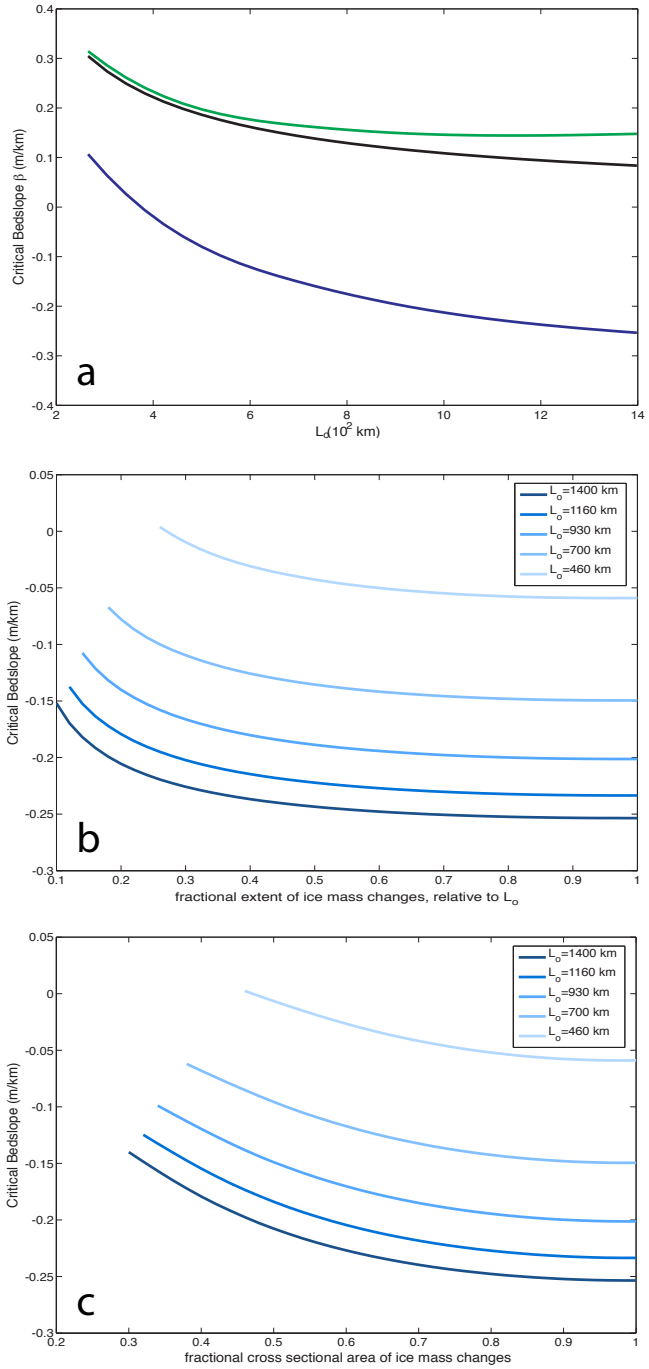

Figure 4.4: Exploration of the parameter space governing sea-level stabilization of marine ice sheets. (A) Predictions of the "critical bed slope" (see text) as a function of grounding line position L. The black curve is computed on the basis of Equation (4.1). The green and blue curves are computed using Equation (4.2), where the change in sea level dD is calculated assuming eustasy (i.e., ESL) or a GSCSL theory, respectively. A marine ice sheet with a bed slope that falls below the line will be unstable. (B), (C) Contributions to the critical bed slope in (A), for a range of initial ice sheet sizes, as a function of the fractional extent or fractional cross-sectional area, respectively, of the ice-mass change zone.

line. In the $L_o = 700$ km case, for example, the 0.25 fractional extent that yields a critical bed slope of -0.1 m/km corresponds to a fractional cross-sectional area of ~ 0.5. We conclude that the stabilization may be important even in the case of relatively localized perturbations in ice mass.

Note that the ice-mass perturbation need not be instantaneous. Our predictions of GSCSL change are based on elastic Earth models, and they are therefore accurate for mass changes integrated over times scales up to $\sim 300 - 500$ years (the Earth's Maxwell time). The issue of time scale is also relevant to our neglect of sea-level variations due to (meltwater-induced) perturbations in ocean dynamics. Global ocean simulations [Kopp et al., 2010] that include freshwater hosing from Greenland into the North Atlantic suggest that static sea-level perturbations will dominate dynamic effects in most of the world ocean once melt volumes have reached ~ 20 cm of equivalent ESL change. In the near-field of the ice sheet, where the GSCSL changes are largest, this dominance will likely be established at much lower magnitudes of melt. We also note that changes in sea level associated with freshening or warming could be largely compensated for by a decrease in flotation thickness of the ice at the grounding line.

The large difference in the near-field and far-field sea-level signal computed using a GSCSL theory has implications for any potential teleconnection between ice sheets in opposite hemispheres. As an example, melting from the Greenland Ice Sheet would lead to a sea-level rise at the WAIS that is 15%-30% above the eustatic value associated with this mass loss, depending on the specific location. If this local sea-level rise triggered an instability of roughly the same mass in the WAIS, the local sea-level drop that results would be an order of magnitude larger than the initial sea-level rise, and this difference would preclude a runaway inter-hemispheric ice-sheet instability. However, such inter-hemispheric teleconnections might not be precluded if meltwater volumes originating from the far-field were much larger than the local melt loss triggered by the consequent sea-level rise, as might have occurred during periods of the ice age (see Chapter 6 for an ice-age application

of coupled ice sheet - sea level modeling).

The above results have highlighted the potential importance of the sea-level stabilization mechanism using a highly simplified model of marine ice-sheet stability based on Weertman [1974]. More complete descriptions of grounding line dynamics and marine ice-sheet stability have been developed which include ice-shelf buttressing [Dupont, 2005; Goldberg et al., 2009], boundary layers to model the ice sheet-ice shelf transition zone [Schoof, 2007a,b] and an extension to three dimensions [Katz and Worster, 2010]. However, the GSCSL physics we have described is universal, and thus it will be active regardless of the level of complexity in the ice-sheet stability theory. In this regard, our results provide a framework for including the sea-level stabilization mechanism in more realistic models (as described in the next two chapters of this thesis) and, in turn, should lead to improved estimates of the stability and possible rates of change of marine-ice sheets such as the West Antarctic Ice Sheet.

Chapter 5

Evolution of a coupled marine ice sheet - sea level model

In this chapter, we investigate the stability of marine ice sheets by coupling a gravitationally self-consistent sea-level model valid for a self-gravitating, viscoelastically deforming Earth to a 1-D marine ice sheet-shelf model. The evolution of the coupled model is explored for a suite of simulations in which we vary the bed slope and the forcing that initiates retreat. We find that the sea-level fall at the grounding line associated with a retreating ice sheet acts to slow the retreat; in simulations with shallow reversed bed slopes and/or small external forcing, the drop in sea level can be sufficient to halt the retreat. The rate of sea-level change at the grounding line has an elastic component due to ongoing changes in ice-sheet geometry, and a viscous component due to past ice and ocean load changes. When the ice-sheet model is forced from steady state, on short timescales ($<\sim$ 500 years), viscous effects may be ignored and grounding-line migration at a given time will depend on the local bedrock topography and on contemporaneous sea-level changes driven by ongoing ice-sheet mass flux. On longer timescales, an accurate assessment of the present stability of a marine ice sheet requires knowledge of its past evolution.

A version of this chapter was published with David Pollard, Jerry X. Mitrovica, Peter Huybers and Peter U. Clark in the journal Geophysical Research Letters Vol. 117, F01013, 2012.

5.1 Introduction

The stability of polar ice sheets, and in particular that of the West Antarctic Ice Sheet (WAIS), is of central concern within studies of modern climate change [Lenton et al., 2008; Smith et al., 2009]. The WAIS is a marine-based ice sheet that interacts with the surrounding ocean. The ice shelves that fringe the WAIS are known to have a stabilizing or buttressing effect on the ice sheet [Dupont, 2005; Goldberg et al., 2009; Thomas and Bentley, 1978], but these shelves appear susceptible to climate change since warming of the atmosphere and/or ocean could lead to increased melting and disintegration either from above and/or below, respectively [Jenkins and Doake, 1991; MacAyeal et al., 2003; Rignot, 2002]. Indeed, collapse of ice shelves as well as thinning, retreat and acceleration of outlet glaciers have recently been observed in various sectors of the WAIS [e.g. Rignot, 2006; Shepherd, 2001; Thomas, 2004; Wingham et al., 2009].

Marine ice sheets gain mass by accumulation throughout their interior and they lose mass by flux of ice across the grounding line into floating ice shelves. The grounding-line zone is located where the ice changes from being thick enough to keep the base of the ice grounded on bedrock below the local sea surface, to thin enough that the ice floats, dividing the floating ice shelves from the grounded ice sheet. Ice thickness at the grounding line is approximately proportional to the depth of water; in order for the ice sheet to come into equilibrium after an increase in water depth requires the grounding line to shift toward a shallower location [Schoof, 2007a; Thomas and Bentley, 1978; Weertman, 1974]. As discussed in Chapter 4, Weertman [1974] used a steady state ice-sheet model to argue that marine ice sheets resting on reversed bed slopes (i.e., sloping down toward the interior) are unstable and prone to rapid retreat [see also Thomas and Bentley, 1978]. This so-called Marine Ice Sheet Instability Hypothesis is based on the premise (supported by analysis in the references above) that ice velocity across the grounding line depends very strongly

on grounding-line depth, so as the grounding line retreats into deeper water, the rapidly increasing flux of ice across the grounding line causes drawdown of upstream grounded ice and an accelerating grounding-line retreat. These conclusions have been supported by recent theoretical studies that have extended these canonical analyses to include ice-shelf buttressing, boundary layers to model the ice sheet/ice-shelf transition zone and an extension to three spatial dimensions [e.g., Dupont, 2005; Goldberg et al., 2009; Katz and Worster, 2010; Schoof, 2007a].

In general, investigations of marine ice-sheet stability have either ignored sea-level changes associated with ice-mass changes, or included them by assuming that such changes are geographically uniform [Schoof, 2007a; Thomas and Bentley, 1978; Wilchinsky, 2009]. However, gravitationally self-consistent predictions of sea-level change following the retreat or advance of grounded ice sheets or glaciers are characterized by dramatically non-uniform geometries. In particular, in the vicinity of a rapidly melting ice sheet (i.e., within 2000 km), sea level will fall as a consequence of instantaneous gravitational and deformational effects [Farrell and Clark, 1976; Gomez et al., 2010b; Mitrovica et al., 2001, see Chapter 2]. These effects also contribute to a geographically variable pattern of sea-level rise predicted for sites at greater distances from the ice sheet. In Chapter 4, we coupled predictions of this instantaneous sea-level fingerprint to the Weertman [1974] steady state 1-D ice-sheet model, and demonstrated that on a reversed bed, the sea-level fall resulting from ice loss compensates for the deepening of the bed, and for some reversed bed slopes this compensation is sufficient to stabilize the ice sheet.

The present analysis extends the analysis in Chapter 4 by rigorously introducing the dimension of time, i.e., we move beyond simple descriptions of instability versus stability to assess the timescale of retreat for a range of ice-sheet forcings. This analysis requires more complex sea-level and ice-sheet models. The sea-level fingerprints used in Chapter 4 are valid for melting events with a timescale less than the Maxwell time over which the solid Earth deforms elastically. However,

large-scale changes in ice sheets can take place over several thousand years or longer. Recall from Chapter 2 that on these timescales, the viscous response of the upper mantle and crust, which will be a function of the entire pre-history of ice and ocean loading, can contribute significantly to local changes in sea level. In this case, the elastic and viscous responses combine to produce, for example, a localized zone of uplift on the solid Earth in the vicinity of a melting ice sheet and a subsidence of surrounding forebulges as the system relaxes toward isostatic equilibrium. To model such effects, we adopt a gravitationally self-consistent sea-level model that accounts for the deformation of a self-gravitating, viscoelastic Earth model [Kendall et al., 2005; Gomez et al., 2010b]. In addition, the Weertman [1974] ice-sheet model considered only the stability of steady state ice-sheet configurations. Here we employ a dynamic ice-sheet model [Pollard and DeConto, 2007, 2009] to investigate how sea-level changes influence the timescale and extent of retreat of a marine ice sheet subject to a perturbation in climate.

5.2 Model Setup

5.2.1 Ice-Sheet Model

We adopt a 1-D, axisymmetric version of the ice sheet-shelf model described by Pollard and DeConto [2007, 2009]. In this type of model, long-term variations of ice thickness are stepped forward in time, accounting for net horizontal advection by ice flow, annual accumulation minus ablation on the ice surface, and any melting or freezing at the base. Our model heuristically combines the scaled equations for grounded (shearing) flow and for floating or stream (stretching) flow. The grounding-line zone acts as a boundary layer between the two flow regimes, and a recent parameterization of ice velocity at the grounding line [Schoof, 2007a] captures the effect of the grounding-line zone on the large-scale flow in the model and avoids the need for very fine resolution to resolve explicitly variations through the grounding-zone boundary layer. Following Schoof [2007a], this

parameterization also incorporates buttressing of the upstream flow by ice shelves. In addition, the model predicts ice thickness variations due to mass advection and surface mass balance. For all runs here, ice temperatures and thermal effects are not included, and ice rheology is uniform with a Glen flow law exponent of 3 and a coefficient of 2×10^{-16} Pa^{-3} a^{-1}. Basal sliding occurs wherever the ice is grounded. The sliding velocity is given by $u_b = B\tau_b^2$, where τ_b is basal shear stress and $B = 10^{-10}$ m a^{-1} Pa^{-2} is the sliding coefficient. Unless otherwise specified, surface accumulation everywhere is 0.1 m a^{-1} ice equivalent with no seasonal or interannual variability, and there is no sub-ice shelf oceanic melting. At the most peripheral grid point (right-hand side of the plots below), ice thickness is set to zero, which is equivalent to allowing free flow of ice out of the model domain and has no upstream effect. The interior edge of the domain (left-hand side of the plots below) is a divide, i.e., where the ice elevation is maximum, and surface slope and ice flux are zero; this is nominally the South Pole for the idealized model here, but would be the limit of the catchment area for real glacier systems. The ice sheet domain is regularly gridded in latitude at 0.1 latitude (11 km) and irregularly gridded in the vertical into ten intervals, and the model time step is 0.1 yr. Note that the results of experiments with twice the spatial resolution and shorter time steps showed no significant differences from the results presented here.

Floating ice shelves affect upstream flow and grounding line migration by their back stress ('buttressing') at the grounding line [e.g., Schoof, 2007a]. Back stress is caused by the ice shelf moving past or abutting land or grounded ice (called "side drag" here), or by bedrock pinning points impinging on its base. In their absence, a freely floating ice shelf would provide zero back stress at the grounding line, and would have no dynamical effect on grounding-line position or on upstream grounded flow if it were to break up entirely; conversely, breakup of a previously buttressing ice shelf can cause dramatic upstream acceleration, drawdown of grounded ice, and grounding-line retreat [Scambos et al., 2004; Schoof, 2007a]. To include buttressing effects in idealized 1-D flow line

studies, side drag or pinning points must be parameterized [Dupont, 2005; Gagliardini et al., 2010; Goldberg et al., 2009]. Here, a retarding stress per unit horizontal area is applied in the momentum equation where ice is floating, proportional to ice thickness and velocity, and independent of flow band width [similar to Gagliardini et al., 2010]:

$$SD = Ku_a h, \tag{5.1}$$

where SD is the retarding stress (in units of N m^{-2}), K is a coefficient with nominal value 3×10^{-4} N a m^{-4}, u_a is ice-shelf horizontal velocity (in m a^{-1}), and h is ice-shelf thickness (in m). This simple parameterization can be considered to represent either side drag or pinning points equally well; in reality, both probably depend on ice thickness and velocity with at least the same sign as in equation (5.1) (but note that we use the phrase "side drag" for brevity throughout this paper). The nominal magnitude of K is selected to produce reasonable pre-perturbation states in the flow line model; a more realistic prediction will require 3-D modeling with explicit side-shear geometry and pinning-point bathymetry.

5.2.2 Sea-Level Model

We adopt the generalized, gravitationally self-consistent sea-level theory described in detail by Kendall et al. [2005] and Gomez et al. [2010b], and reviewed in Chapter 2. In particular, we use the version of this theory valid for a spherically symmetric, self-gravitating, Maxwell viscoelastic Earth model (here called the GSCVE sea-level theory). As in Chapters 2 and 4, the depth-dependent variations in the elastic and density structure in the Earth model are given by the seismic model PREM [Dziewonski and Anderson, 1981] and the viscosity structure is characterized by an infinite viscosity (i.e., elastic) lithosphere of thickness 120 km, an upper mantle viscosity of 5×10^{20} Pa s and a lower mantle viscosity of 5×10^{21} Pa s [Lambeck et al., 1998; Mitrovica and Forte, 2004].

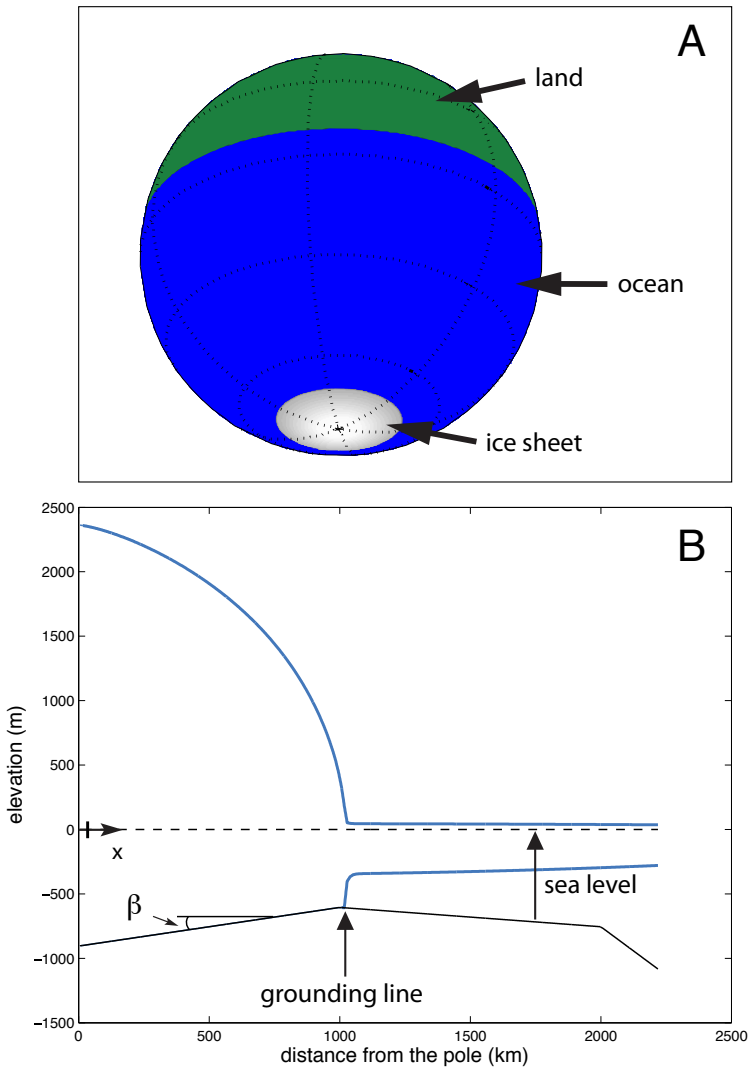

Figure 5.1: Schematic illustrating the initial steady state model configuration. (A) The axisymmetric configuration of the model Earth, which includes an ocean covering 70% of the surface area of the Earth (blue), a spherical cap continent at the North Pole (green), and a circular disk ice sheet on the South Pole (white). (B) Cross section of the ice sheet in Figure 5.1a. The blue lines represent the elevation of the surface of the ice and the bottom of the ice shelf. The solid black line represents the elevation of the bedrock and the dashed black line at zero elevation represents the sea surface. The ice sheet's grounding line, corresponding to the junction of the solid blue and black lines, is initially located just outside of a region where the bed slopes down to the center of the ice sheet with slope β.

Recall from Chapter 2 that the GSCVE sea-level model accounts for the exchange of mass between grounded ice and ocean and incorporates time-dependent shoreline migration, allowing for the inundation of water into areas freed of marine-based ice. Since the model is gravitationally self-consistent, deformation of the solid surface and the sea surface equipotential are coupled, i.e., deformation of the solid Earth alters the gravitational field and thus perturbs the sea surface. The latter impacts the distribution of water in the model, and this redistribution will, in turn, deform the solid Earth.

Figure 5.1A shows the axisymmetric continent configuration adopted in our model. It is comprised of two regions: a continent with bedrock below the sea surface at the South Pole on which the ice sheet sits (see discussion of Figure 5.1B below) and a spherical cap continent centered at the North Pole with elevation above the sea surface elevation. The area of the latter is chosen such that 70% of the surface area of the Earth is covered by ocean and ice shelves in the initial configuration of the Antarctic Ice Sheet model. The initial state of the ice, bedrock and ocean is assumed to be in isostatic equilibrium, and the sea-level model predicts changes from this state as the ice sheet evolves, as described in Section 5.2.3. Sea-level calculations are performed with a truncation at spherical harmonic degree 512 (i.e., a spatial resolution of 40 km).

5.2.3 Ice Sheet - Sea Level Coupling

We perform a two-way coupling between the ice-sheet and sea-level models described above. Predictions of current sea level in the model are used to update bedrock topography in the ice-sheet model. Conversely, predictions of ice geometry in the ice-sheet model are used to specify ice loading in the sea-level model. In the simulations described below, the ice-sheet model is run continuously for $10,000$ years. Every 50 years, the current ice geometry is passed to the sea-level model, which computes the sea-level change (or equivalently, the negative of the bedrock elevation change) over

the last 50-year interval. The current sea-level field is updated accordingly and passed back to the ice-sheet model. Passed fields are linearly interpolated in latitude between the two model grids. Note that we also ran a series of simulations with shorter coupling time intervals and these results showed no significant differences from the simulations shown here using a 50 year interval.

As discussed above, the change in the current sea level computed by the GSCVE sea-level model is a combination of (1) an instantaneous elastic deformation of the solid Earth and perturbation to the sea surface equipotential driven by contemporaneous ice and ocean load changes and (2) a delayed viscous response of the solid Earth (and associated gravitational effects) that depends on the entire history of ice and ocean loading. In order to model the viscous response, the GSCVE sea-level model stores the entire sequence of 50-year-interval ice geometries from the start of the run, and uses them to compute the current sea level each time it is called. A critical quantity that we must track for the purpose of coupling the sea level and ice-sheet models is the distance between the surface that the ice rests upon and the gravitational equipotential that defines the sea surface. This distance governs the buoyancy of grounded ice. We specify the equipotential sea surface as zero elevation in the ice-sheet model, and in this reference frame changes in bedrock elevation are equivalent to the negative of changes in sea level. This relationship permits a simple coupling of the two models.

As noted above, the ice-sheet model domain is axisymmetric in longitude, with only one grid cell in the east-west direction. Within the ice-sheet model, the longitudinal arc-width of the flow band is arbitrary. The arc-width is specified as 360 for coupling to the sea-level model, which is global in extent and axisymmetric, i.e., as shown in Figure 5.1A. Chapter 6 will address more realistic geometries associated with specific Antarctic sectors.

5.3 Experiments

In this section, we consider the impact of the sea-level coupling on the ice sheet response to a prescribed external forcing for a range of parameter choices and timescales. The ice-sheet model is initially run to the steady state configuration illustrated in Figure 5.1B. The ice sheet's grounding line is initially located 10 km outside a region where the bed inclines down to the center of the ice sheet with slope β.

In many of the experiments below, the external forcing is a reduction in ice-shelf buttressing, imposed by reducing the side-drag coefficient K in equation (5.1). The model would also respond similarly if, for instance, sub-ice-shelf oceanic melt rates (zero in all experiments here) were increased, which would thin the ice shelf and reduce side drag through the term h in equation (5.1). However, in line with the idealized geometry and to simplify the interpretation of results, we have chosen to reduce K directly. Actual reductions of buttressing in real Antarctic ice shelves stemming from atmospheric and oceanic forcing are deferred to future 3-D modeling. In the first set of experiments (Figure 5.2),the side-drag coefficient K is instantaneously reduced at time $t = 0$ from its nominal value, which increases the flux of ice across the grounding line, causing the grounding line to retreat onto the reversed bed slope. As an example, Figure 5.2A shows the evolution of the ice sheet along a reversed bed slope of $\beta = 0.7$ m/km following a reduction in K to 2/3 its nominal value. In this example, the positions of the bedrock and sea-surface equipotential stay constant (i.e., the sea-level coupling is not included). Once the grounding line reaches the reversed slope, a small additional retreat moves the grounding line into deeper water, leading to a greater ice loss across the grounding line and further retreat. As a consequence, the ice sheet retreats down the slope until it disappears. The full retreat takes approximately 4000 model years.

Next, we explore the implications for this particular scenario of adding the sea-level coupling

to the ice-sheet model (Figure 5.2B). In this case, as the ice sheet retreats, sea level falls, or equivalently, the bedrock elevation relative to the sea-surface height increases (the black line in Figure 5.2B deforms upwards). Thus, the water level is shallower at the new grounding line than predicted in the simulation where sea level remained fixed (Figure 5.2A). The rate of ice loss across the grounding line is slower than in the fixed-bed case and the retreat is slowed. The ice sheet takes 7300 years to disappear, or 1.8 times longer than predicted in Figure 5.2A.

Figure 5.2C shows the sea-level change relative to the initial steady state (i.e., relative to the horizontal line) at each time step of the ice-sheet evolution plotted in Figure 5.2B. As described above, the sea-level changes are applied as a perturbation to the bedrock topography in Figure 5.2B. Elastic effects dominate the sea-level change 1000 years into the evolution. As the ice sheet loses mass over this time interval, the gravitational attraction it exerts on the surrounding water weakens and, in response, water migrates away. In addition, the solid Earth in the vicinity of the ice loss and water out-flux rebounds elastically. Both of these effects contribute to the sea-level fall predicted by the GSCVE sea level model at the grounding line [Gomez et al., 2010a]. In subsequent time steps, the viscous effects also act to raise the bedrock at the grounding line, thus elastic and viscous effects combine to produce a further decrease in sea level. Note that since gravitational and deformation effects are coupled (see Section 6.2.2), raising the solid surface toward isostatic equilibrium counters the direct gravitational effect of ice loss (i.e., the net negative mass anomaly created by past ice loss and solid Earth deformation tends to zero as the solid surface rebounds toward isostatic equilibrium). However, this signal is swamped by deformation driven by the ongoing ice mass loss. Within a given time interval, the fall in sea level is greatest in the region across which the grounding line migrates (i.e., the maximum drop in the sea-level curves in Figure 5.2C are located near the corresponding grounding line location in Figure 5.2B).

When the external forcing imposed through a reduction in the side drag coefficient and/or the

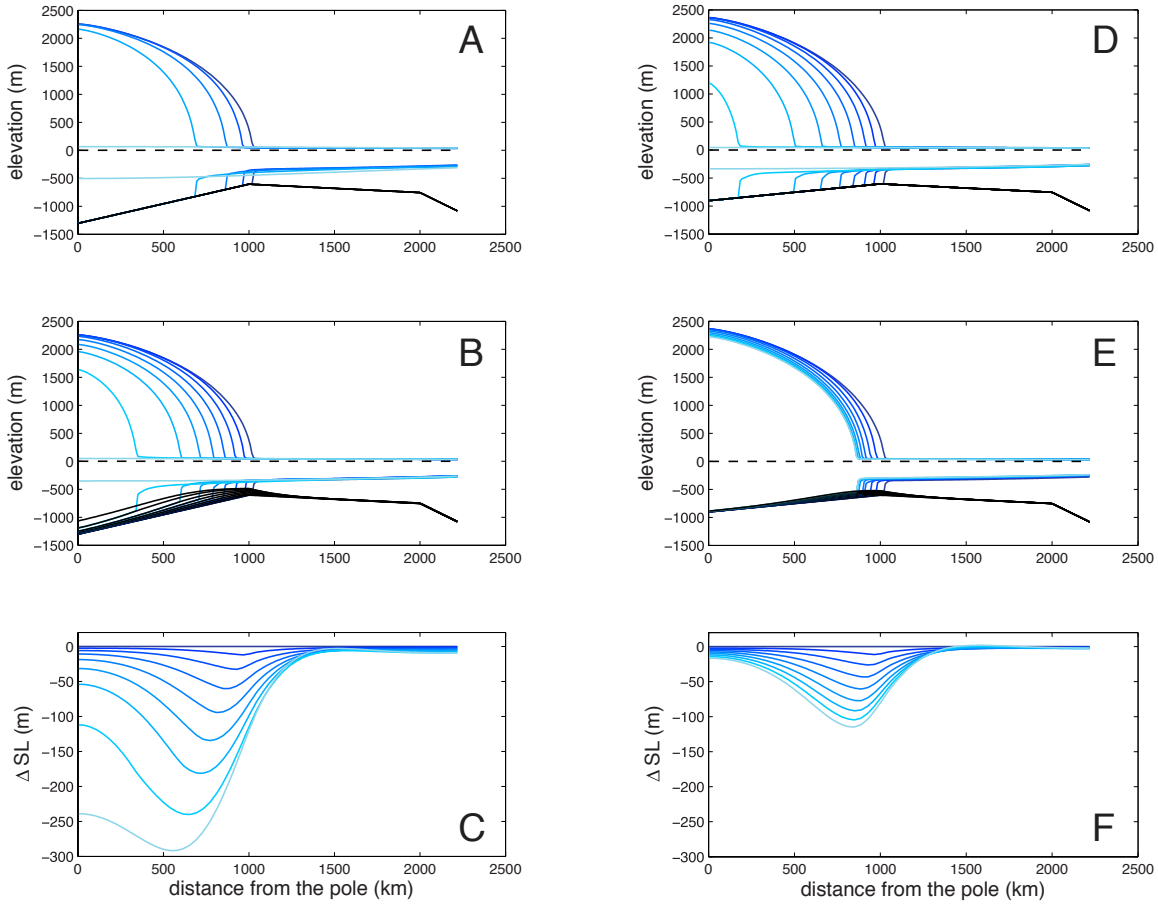

Figure 5.2: The evolution of the ice sheet shown in Figure 5.1B following a reduction in the side-drag coefficient to 2/3 its nominal value. Ice and bedrock elevation contours are plotted every 1000 years, and the ice contours move from dark to light blue as time increases. (A and B) The retreat along a reversed bed of slope 0.7 m/km in the fixed topography (Figure 5.2A) and topography that is updated by the sea-level model every 50 years (Figure 5.2B). (C) sea-level change in the scenario of Figure 5.2B relative to the initial steady state, plotted every 1000 years. (D-F) Analogous to Figures 5.2A -5.2C for retreat along a bed slope of 0.3 m/km.

reversed bed slope are sufficiently small, the fall in sea level that accompanies ice-sheet retreat will be large enough that the ice sheet stabilizes to a new steady state. An illustrative scenario is shown in Figures 5.2D-5.2F for the case of an ice sheet resting on a bed slope that is initially 0.3 m/km, which is less steep than the value adopted in Figures 5.2A-5.2C (0.7 m/km). In Figure 5.2D, the bedrock and sea-surface elevations are held constant and the ice sheet disappears in 7200 years. In contrast, when the sea-level coupling is included in Figure 5.2E, the sea level fall (Figure 5.2F) is sufficient to halt the ice-sheet retreat. The ice sheet reaches a new equilibrium with the grounding line located 200 km inland of its initial position. Note from Figure 5.2F that as the ice sheet reaches a new equilibrium, ongoing viscous deformation toward isostatic equilibrium causes sea level to continue to fall. This residual sea-level change further stabilizes the ice sheet and may lead to a future re-advance.

5.3.1 Bed Slope and Forcing Parameters

In this section, we discuss results of sensitivity analyses that vary several key aspects of the ice-sheet model. To begin, we investigate further the influence of changing the bed slope adopted in the initial steady state configuration of the model. In Figure 5.3A, we initiate ice-sheet retreat with a fixed, 60% reduction in the side-drag coefficient, and track the location of the grounding line as a function of time for simulations with a range of initially reversed bed slopes. The green lines are results of simulations in which sea level is fixed (i.e., as in Figures 5.2A and 5.2D) while the blue lines plot the grounding-line position when sea-level changes are coupled with the ice-sheet model (as in Figures 5.2B and 5.2E). In all cases where sea level is fixed, the grounding line retreats down the reversed slope until the ice sheet completely disappears, and the time scale of collapse increases with progressively shallower slopes. Once again, the inclusion of the sea-level coupling acts to slow the rate of retreat. For initial bed profiles that are horizontal or have a relatively shallow slope

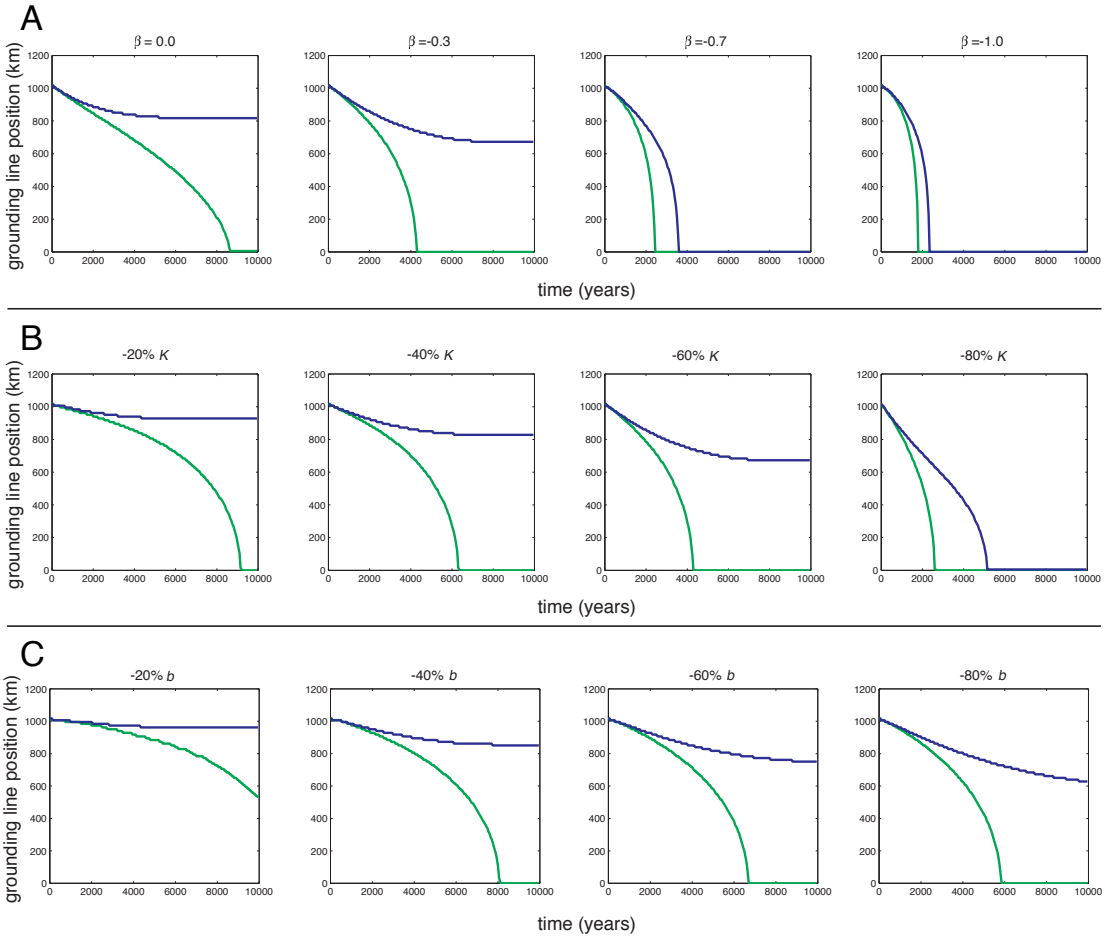

Figure 5.3: Grounding-line position as a function of time for (A) ice-sheet retreat initiated by a fixed 60% reduction in the side-drag coefficient, K, down a range of reversed bed slopes of magnitude 0.0 to 1.0 m/km (as labeled). (B) As in Figure 5.3A except for reductions in the side-drag coefficient within the range 20%-80% of the nominal value and a fixed bed slope of 0.3 m/km. (C) As in Figure 5.3B, except that the side-drag coefficient is fixed and retreat is instead initiated by a reduction in the accumulation rate, b, of 20%-80% of the nominal rate of 0.1 m a $^{-1}$. The green lines are results when sea-level change is not coupled into the ice-sheet model, whereas the blue lines include this coupling.

($\beta = 0.3$ m/km), the sea-level fall at the grounding line is ultimately sufficient to halt the retreat and the ice sheets reach a new steady state 200 km and 300 km inward, respectively, of the original grounding line.

Next,we consider the effect of varying the strength of the forcing that is applied to initiate the retreat. Figure 5.3B plots the grounding-line position as a function of time for simulations on a

reversed bed slope of 0.3 m/km and a range of reductions in the ice-shelf side-drag coefficient K in equation (5.1). In the case where sea level is fixed, the speed of grounding-line retreat increases with greater reductions in K, and thus the time scale for complete collapse decreases. The inclusion of the sea-level coupling once again acts either to halt (Figure 5.3B, with a 20%, 40%, or 60% reduction in K) or slow down (by a factor of 2 with an 80% reduction in K) the retreat.

In addition to driving retreat by reducing the side-drag coefficient, we also initiated ice-sheet retreat by reducing the rate of accumulation. The results presented in Figure 5.3C show similar trends to those evident in Figure 5.3B except that the ice sheet responds less strongly to accumulation changes than to the same percentage change in the side-drag coefficient. In addition, in order to initiate retreat onto the reversed slope, these simulations prescribe rates of accumulation that are lower than the range expected over the Antarctic Ice Sheet. This difference in response is not surprising since marine ice in the Antarctic is generally more sensitive to changes in ocean temperature than to changes in accumulation rates and surface melting [Jenkins and Doake, 1991; MacAyeal et al., 2003; Rignot, 2002]. Thus, reducing the ice-shelf buttressing effect (through a reduction in side drag) is a more effective way of initiating retreat than altering accumulation rates.

Finally, in Figure 5.4 we summarize a large sequence of results based on simulations with a range of external forcing and bed slope combinations. In particular, Figure 5.4A plots the ratio of the time taken for the grounding line to retreat 200 km in simulations based on the coupled ice sheet-sea level model relative to simulations in which sea level is fixed in time. Figure 5.4B shows analogous results for a grounding line retreat of 500 km, i.e., the contours in Figure 5.4 represent the multiplicative factor by which the time scale of retreat is extended as a consequence of the inclusion of the GSCVE sea-level model. In some simulations the grounding line does not retreat by the target distance within the 10,000 year model run either because a new steady state is reached

(indicated by light gray contours) or because the retreat velocity is too small (dark gray contour). As an example, if the side-drag coefficient is reduced by half its nominal value on a reversed bed slope of 0.7 m/km, the inclusion of the sea-level feedback in the ice-sheet model extends the time scale by a factor of 1.3 for a 200 km retreat and by a factor of 1.6 for a 500 km retreat. The sea-level feedback has greater influence on the ice sheet's stability for the case of the 500 km retreat, rather than the 200 km retreat. The reason is that the former level of retreat involves more ice loss and is achieved over a longer time scale than the latter; therefore, the net sea-level fall predicted by the GSCVE sea-level model at the grounding line, which acts to compensate for the reversed bed slope, is greater.

5.3.2 Elastic and Viscous Effects

As we discussed earlier in this chapter and in more detail in Section 2.4, the sea-level change at a given time in the evolution of the ice sheet is due to both an instantaneous elastic signal associated with ongoing ice and ocean load changes and a viscous signal that depends on the complete time history of loading changes. Figure 5.5 explores the relative contribution of these signals to the computed ice-sheet evolution for three different values of the initial bed slope ranging from 0.3 to 0.7 m/km. In all cases, ice-sheet retreat is initiated through a 60% reduction in the ice-shelf side-drag coefficient. The green line in each frame represents the case where sea-level changes are not incorporated into the ice-sheet model, and the blue and red lines are the results of simulations that incorporate sea-level changes either predicted by the GSCVE sea-level model or a special case of this sea-level model that only includes an elastically deforming Earth model, respectively. In the first 500 years of the simulation (i.e., less than or comparable to the Earth's Maxwell time), the stabilization associated with the sea-level feedback is the same whether the sea-level solver adopts an elastic or viscoelastic Earth rheology. On longer timescales, these two cases diverge as

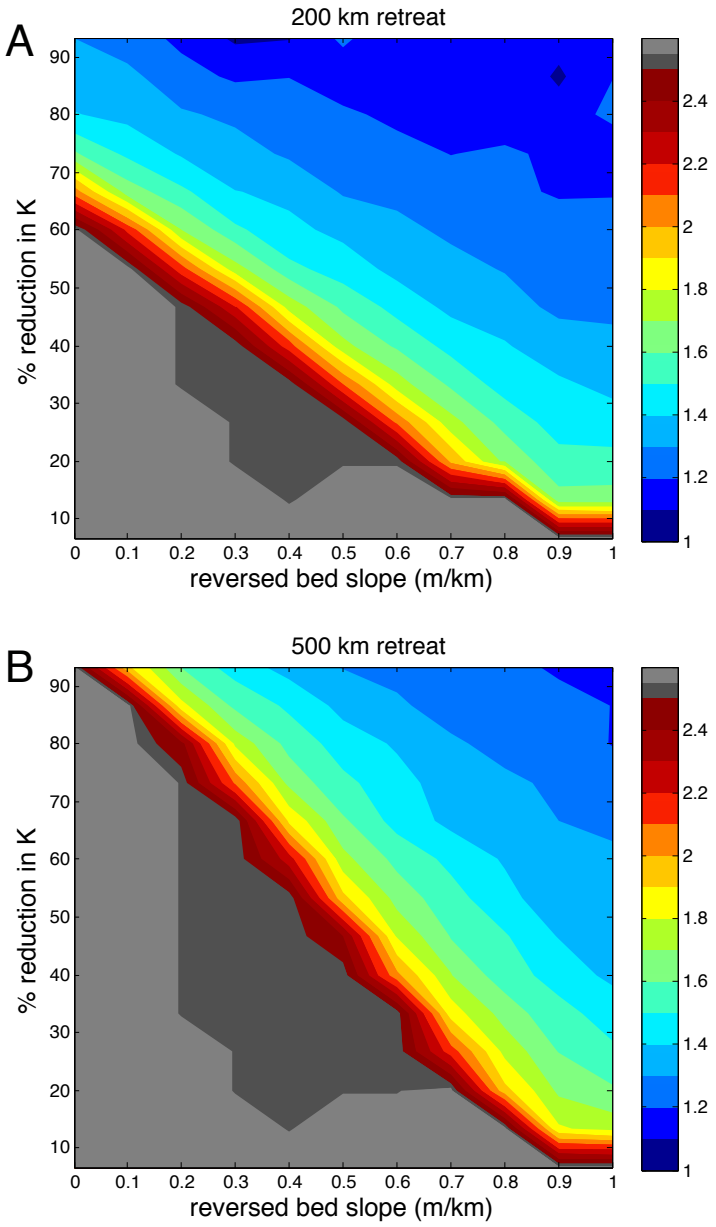

Figure 5.4: The ratio of the time scale of ice-sheet retreat including sea-level change coupling to the case without this coupling. Results are contoured as a function of bed slope and the percent reduction in side-drag coefficient K, where the latter is used to initiate retreat. The frames refer to time scales required for a retreat of either (A) 200 km or (B) 500 km and a total simulation time of $10,000$ years. The gray contours represent simulations in which the coupled model does not retreat to the target distance within the $10,000$ year simulation time, either because the retreat is too slow (dark gray) or the system reaches a new equilibrium (light gray).

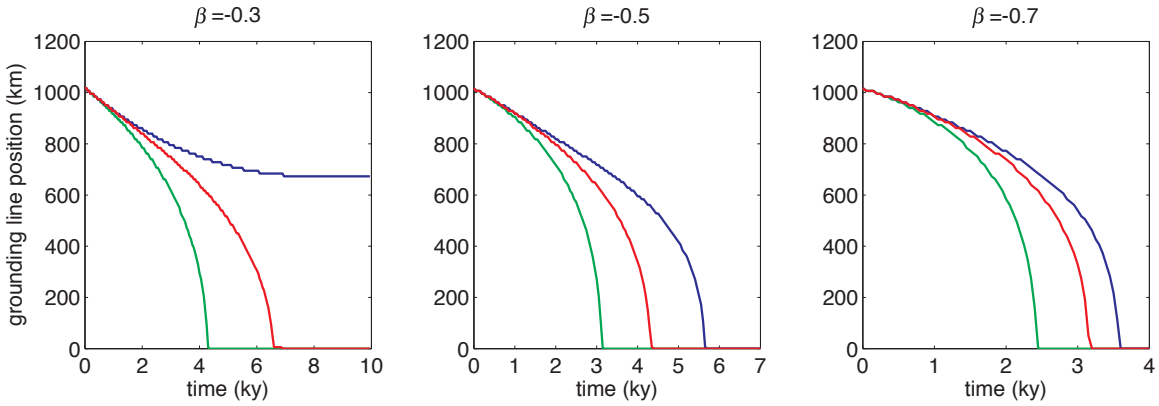

Figure 5.5: Grounding-line position of the ice-sheet model as a function of time, in cases where sea level is not included in the model ice-sheet evolution (green); or where the ice-sheet model incorporates sea-level changes computed using either the full viscoelastic Earth response (blue), or the elastic response alone (red). Results are shown for a range of reversed bed slopes, as labeled on each frame, and in all cases retreat is initiated by a 60% reduction in the side-drag coefficient.

the ongoing viscous effects from past ice and ocean load changes become important. The elastic component of sea-level change is an important stabilization mechanism throughout the evolution of the ice sheet, and this importance relative to the full viscoelastic case is proportionately greater as the rate of retreat increases or, equivalently, the amplitude of the reversed bed slope increases (Figure 5.5).

5.3.3 Conclusions

Accurate prediction of global sea level requires knowledge of the evolution of marine ice sheets, and it appears that local changes in sea level can have a first order influence upon the rate of mass loss that marine ice sheets undergo and the equilibrium states that they may attain. In Chapter 4, we considered the influence of sea-level changes on the stability of marine ice sheets by coupling the steady state ice-sheet model of Weertman [1974] to a sea-level model that adopted an elastically deforming Earth model . While the study highlighted the potential importance of the sea-level feedback, it was inadequate for the purposes of exploring the influence of this stabilization

mechanism on the timescale of ice-sheet retreat.

Here, we coupled a gravitationally self-consistent sea-level model that incorporates viscoelastic deformation of the Earth [Gomez et al., 2010b; Kendall et al., 2005, Chapter 2] to a more realistic, time-evolving marine ice sheet-shelf model [Pollard and DeConto, 2007, 2009] and considered the timescale of retreat under a large suite of simulations in which the external forcing, bed slope, and sea-level feedback were varied. Our results demonstrate that the sea-level fall associated with a retreating ice sheet will slow down and, in the case of shallow reversed bed slopes and/or small external forcing, may even halt the retreat (see Figure 5.4). Therefore, the stability and motion of the grounding line will depend not only on the local bed slope but also on the magnitude and rate of local sea-level change. Changes in local sea level depend upon redistribution of ice mass and both elastic and viscous deformations of the solid Earth, where determining the viscous deformation requires accounting for the full history of ice and ocean loading. In the case of a steady state ice sheet entering into a rapid retreat, viscous effects can be largely neglected for the first several centuries.

We have focused here on ice sheet-wide changes in mass, taking place on millennial timescales. Of course, localized mass loss can occur on shorter timescales. For a given mass loss, the local sea-level fall associated with rapid melting will increase as the spatial scale decreases. However, given the existence of an elastic lithosphere, the contribution from deformational effects will generally decrease as the spatial scale of the localized melting is reduced. Thus, the influence of sea-level stabilization in the case of century scale and localized melting is worthy of future, detailed study.

Our predictions have been based on a 1-D ice-sheet model with a simplified bedrock geometry. In future work, we will consider other factors that influence the evolution of the grounding line, such as lateral stresses, non-uniform bedrock gradients and variable basal conditions. Grounding-line migration in the ice-sheet model we have adopted depends on the Schoof [2007a] flux parameteriza-

tion, and this should be tested using higher-resolution and higher-order ice-sheet models. We also plan to investigate the adequacy of linear or bilinear spatial interpolation in passing fields between the sea level and the ice-sheet models. More generally, it will be important to assess the extent to which the sea-level stabilization mechanism discussed herein remains important in the context of more realistic treatments of marine-based outlet glaciers and tidewater glacier environments. We also plan to extend the coupled model to consider the evolution of ice sheets throughout glacial cycles, and in particular since the Last Glacial Maximum. This application may be used, for example, to investigate inter-hemispheric teleconnections between ice sheets [Denton et al., 1986], the timing of ice sheet growth and collapse, and the potential for the sea-level mechanism to stabilize the West Antarctic Ice Sheet during interglaciations and terminations.

Chapter 6

A 3-D coupled ice sheet - sea level model applied to Antarctica through the last 40 ky

In this chapter, we present results from a three-dimensional ice sheet-shelf model of Antarctica, coupled to a gravitationally self-consistent global sea-level model that incorporates (Maxwell) viscoelastic deformation of the solid Earth. The coupled model captures complex post-glacial changes in sea level associated with the gravitational, deformational and rotational effects of the evolving surface mass (ice plus ocean) load over the global ocean, including at the grounding lines of marine-based ice. The simulations are initiated at 40 ka and we focus on ice distributions and sea levels from the Last Glacial Maximum to present. Our results extend and confirm the key conclusions of our earlier work using a simplified, 1-D ice-sheet model, by demonstrating that the sea-level coupling has a significant stabilizing influence on marine ice-sheet grounding lines. The feedback of sea-level changes into the ice-sheet model acts to slow down the retreat and advance of the grounding line relative to simulations in which the full coupling is not incorporated. Differences in ice thickness between these simulations can reach $\sim$1 km close to the grounding line. Finally, we perform preliminary comparisons of our results to relative sea level (RSL) histories and GPS-derived present-day uplift rates at sites near the margins of Antarctica. We find that the coupling

A version of this chapter was published with David Pollard and Jerry X. Mitrovica in the journal Earth and Planetary Science Letters, vol. 384, pp. 88-99, 2013.

improves fits to uplift rates in several regions, and that the RSL predictions of the coupled model yield a fit to the observations that is comparable to recent, uncoupled simulations in which the underlying Earth model was varied to obtain a best-fit to the RSL histories.

6.1 Introduction

Under the backdrop of a progressively warming world, there has been a renewed and comprehensive effort to improve our understanding of the key processes that drove the evolution of the Antarctic Ice Sheet (AIS) from ice age conditions to the present day. This effort has been supported by a broad and growing suite of observational constraints, which include geological records of variations in grounding-line position, ice-sheet surface elevation and relative sea level [see Briggs et al., 2013; Briggs and Tarasov, 2013; Whitehouse et al., 2012a,b, for recent compilations], as well as land and space based measurements of ongoing regional gravity changes [e.g., Velicogna, 2006; King et al., 2013], crustal deformation [e.g. Thomas et al., 2011] and ice outflux velocity [e.g., Larour et al., 2005].

This database has been complemented by ice-sheet modeling studies that have investigated changes in AIS volume over a wide range of time intervals. As an example, Pollard and DeConto [2009] used a combined ice sheet - ice shelf model to track the evolution of the AIS over the past 5 Ma. Their simulation captured trends in both the time scale of ice age cyclicity and the relative duration of glacial and interglacial states inferred from sedimentary records [Naish et al., 2009]. Recently, Whitehouse et al. [2012a] and Briggs et al. [2013] have used numerical ice-sheet models tuned to fit a wide suite of geological and glaciological constraints on AIS extent and thickness, focusing on the history since the Last Glacial Maximum (LGM). Whitehouse et al. [2012a] adopted this history in a model of glacial isostatic adjustment (GIA) to derive a preferred mantle viscosity profile on the basis of fit to relative sea-level (RSL) histories and present-day uplift rates. King

et al. [2013], in concert with Shepherd et al. [2012]'s mass balance inter-comparison effort, used the latter models to correct GRACE gravity data for GIA and concluded that ongoing mass loss from the AIS is a factor of 2-3 smaller than previous estimates. This is consistent with an earlier estimate based on present-day crustal uplift rates from the Antarctic [Thomas et al., 2011] and a GIA correction to GRACE gravity data based on an independent reconstruction of the post-LGM AIS history [Ivins et al., 2013].

One of the main challenges in modeling the evolution of the AIS is accurately capturing the dynamics of the grounding line in marine sectors of the ice sheet. These sectors, which rest on bedrock that lies below the local height of the sea surface, gain mass through surface accumulation, flow outwards and lose about the equivalent amount of mass via flux across the grounding line into floating ice shelves. As discussed in Chapter 5, this mass flux is highly sensitive to the thickness of ice at the grounding line, which is, in turn, proportional to the local water depth. Thus, a feedback is thought to be active in these regions: If the ice-sheet grounding line retreats into deeper water in the presence of reverse bed slopes, the loss of ice across the grounding line increases, leading to further retreat. Conversely, if the ice-sheet grounding line advances into shallower water, flux of ice across the grounding line decreases and the grounding line continues to advance. Weertman [1974] first proposed this feedback, now known as the marine ice sheet instability hypothesis, using a simple, 1-D marine ice-sheet model in steady state, and his now-classic conclusion has been shown to hold in subsequent studies using more detailed numerical models [e.g., Dupont, 2005; Schoof, 2007a; Goldberg et al., 2009; Katz and Worster, 2010; Gudmundsson et al., 2012; Gudmundsson, 2013].

Since the flux of ice across the grounding line is sensitive to the water depth, accurately modeling the dynamics of the grounding line requires a physical model of sea-level change at these locations. Weertman [1974] did not consider sea-level changes, while more recent analyses of marine ice-sheet

dynamics [Thomas and Bentley, 1978; Schoof, 2007a; Wilchinsky, 2009] have assumed that ice-mass changes are accompanied by a globally uniform sea-surface height change. The numerical ice-sheet models for the AIS described above [Pollard and DeConto, 2009; Whitehouse et al., 2012a] were performed using various approximate numerical treatments of sea-level change at the grounding line. The Pollard and DeConto [2009] ice-sheet simulation, for example, used a simple model of post-glacial bedrock uplift, together with eustatic sea-surface height change inferred from oxygen isotope records, to define sea-level change at the grounding line. Whitehouse et al. [2012a] adopted a similar treatment of bedrock uplift, but their sea-surface height changes were adopted from a temporally coarse discretization of a GIA calculation based on an independently derived ice history and Earth model [Peltier, 2004]. Several studies including Whitehouse et al. [2012b], Briggs et al. [2013] and Stocchi et al. [2013] have used GIA models that include gravitational sea-level physics, but driven by Antarctic ice histories from previous runs of independent ice-sheet models.

In Chapters 4 and 5, we showed that a self-consistent coupling between ice-sheet and sea-level models - that is, a coupling that incorporates sea-level changes computed using the modeled ice-sheet evolution - can have a profound influence on the dynamics of a marine ice sheet [Gomez et al., 2010a, 2012]. This work suggests that previous, approximate treatments of sea-level change in the vicinity of the ice-sheet grounding line may introduce significant inaccuracies into the computed ice-sheet evolution.

As discussed in Chapter 2, gravitational, deformational and rotational effects associated with changes in the distribution of grounded ice lead to markedly non-uniform spatial patterns of sea-level change, and sea level will fall in the vicinity of a rapidly retreating ice sheet and it will rise in the vicinity of a rapidly advancing ice sheet. In Chapter 4, we extended Weertman [1974]'s equilibrium ice-sheet stability model to include gravitationally self-consistent sea-level change, and demonstrated that the sea-level effect provides a feedback that partially counteracts the marine

instability of a reversed bed slope[Gomez et al., 2010a]. In Chapter 5, we extended this work using a 1-D dynamic ice-sheet model with simplified geometry to show that the sea-level coupling tends to slow down and, in some cases, halt grounding-line migration. These results highlighted the two components of sea-level change that accompany grounding line migration: (1) An instantaneous change associated with gravitational effects and elastic deformation of the Earth due to the ongoing changes in ice-sheet geometry; and (2) a longer timescale sea-level signal associated with viscous deformation of the Earth due to the full history of ice and ocean load changes. Both of these components of post-glacial sea-level change will be important in accurately modeling the stability and evolution of the Antarctic Ice Sheet during the last glacial cycle and into the future.

In this study, we extend the coupled ice sheet - sea level model in Chapter 5 to three spatial dimensions in the ice-sheet model to consider more realistic ice sheet and bedrock configurations. As a first application of the coupled (3-D) model, we investigate the evolution of the AIS under realistic climate forcings over the last 40 ky. A central aim of this chapter is to demonstrate the effects of coupling marine ice-sheet and sea-level changes relative to previous approximations for the treatment of sea level in ice sheet models. Our results show that these effects are significant and highlight the importance of self-consistent coupling in future work.

We begin in Section 6.2 by describing the coupled ice sheet - sea level model. In Section 6.3.1, we present results of simulations using the coupled model, and compare these results to simulations in which the sea-level coupling is not included. The contributions to the ice-sheet evolution from various physical effects (bedrock uplift, sea-surface fluctuations) associated with the sea-level coupling are also considered in Section 6.3.1. In Section 6.4 we perform a preliminary comparison of our results to available RSL histories and present-day GPS uplift rates. Conclusions are provided in Section 6.5.

6.2 Model Setup

In this section we outline the method by which we fully couple a 3-D Antarctic Ice Sheet-Shelf model and a global model of static post-glacial sea-level change. The details of the models for both ice-sheet evolution and sea-level change have been described in detail elsewhere [e.g., Pollard and DeConto, 2012b; Kendall et al., 2005]. Nevertheless, we will summarize the major elements of these models here, with a particular emphasis on the details of the coupling procedure.

6.2.1 Ice-Sheet Model

We adopt the hybrid ice sheet-shelf model described in detail in Pollard and DeConto [2012b], and applied in Pollard and DeConto [2009, 2012a]. The treatment of ice dynamics is a heuristic combination of the scaled Shallow Ice Approximation (SIA) and Shallow Shelf Approximation (SSA) equations for shearing and longitudinal stretching flow, respectively. The relative contributions of SSA and SIA flow at each point are not prescribed or parameterized, but arise from the model's iterative flow solution (except at points with stiff beds, much stiffer than in grounded streaming regions, where SSA flow would be negligible and is neglected for computational efficiency). A parameterization relating ice velocity across the grounding line to local ice thickness [Schoof, 2007a] is imposed as an internal boundary-layer condition, so that grounding-line migration is simulated accurately without the need for very fine ($\sim$100 m) resolution [Schoof, 2007a; Gladstone et al., 2013; Pattyn et al., 2012]. These two measures are necessary to make the long integrations of this study computationally feasible. The model performs reasonably well in idealized inter-comparisons [Pattyn et al., 2012, 2013], although with somewhat larger differences on smaller space and time scales [Drouet et al., 2013; Pattyn and Durand, 2013].

The ice-sheet model includes a simple treatment of the response of the bedrock to evolving ice and ocean loads. Deformation of the Earth is calculated as a point-by-point, time-lagged astheno-

spheric relaxation towards isostatic equilibrium and incorporates a modulation of the response by an elastic lithosphere. This treatment of bedrock deformation has been used in previous applications [Pollard and DeConto, 2009, 2012a]. Here, it is used only in runs labeled "uncoupled", to distinguish from coupled runs using the new Earth/sea-level model. Compared to the new Earth/sea-level model, the old bedrock treatment has several limitations. First, it includes uniform rather than gravitationally self-consistent ocean load and sea-surface height changes. Second, it models the bedrock response at all spatial scales with a single, a priori prescribed decay time (3 ky), and it does not capture the full, multi-normal mode response of complex viscoelastic Earth models [Peltier, 2004]. The latter incorporates a family of viscoelastic relaxation modes, with decay times that vary across these modes and as a function of the spatial scale of the loading. The limitations of the standard approach are avoided in the fully coupled simulations described below.

We apply the ice-sheet model to the evolution of Antarctica from 40 ka to the present, focusing on the last deglacial retreat of the past 20 ky. A polar stereographic grid is used, with relatively coarse, 40 km grid resolution that permits the numerous long runs described in this chapter; previous tests at 20 km and 10 km show that the results are not sensitive to this change in resolution [Pollard and DeConto, 2012b,a]. This insensitivity extends to the mass flows of major ice streams, which are still coarsely captured by the 40 km grid, as discussed in Pollard and DeConto [2012b]. There are 10 unevenly spaced vertical layers, with standard treatments of ice temperature advection and vertical diffusion. Basal sliding coefficients under modern grounded regions are prescribed from a previous run using an inverse procedure that penalizes misfit to modern observed surface ice elevations [Pollard and DeConto, 2012a]. Basal sliding coefficients in regions of modern ocean or floating ice are set to a uniform value, either 10^{-5} or 10^{-6} m a^{-1} Pa^{-2}, which represent highly deformable "slippery" sediment. All runs below use 10^{-5} m a^{-1} Pa^{-2} unless otherwise stated. There is no explicit basal hydrology in the model.

Surface mass balance is computed from observation-based datasets of modern climatological Antarctic precipitation and temperature (ALBMAP, Le Brocq et al. [2010]; with accumulation from van de Berg et al. [2006]). Simple uniform perturbations for past climates are made in proportion to deep-sea-core δ^{18}O variations, with a minor contribution due to austral insolation variations [Pollard and DeConto, 2009, 2012a]. Simple lapse-rate corrections are made for elevation differences from modern, and a basic positive-degree-day scheme is used for melt [Pollard and DeConto, 2012a]. A simple two-value pattern of geothermal heat flux is prescribed with 54.6 mW m^2 under East Antarctica and 70 mW m^2 under West Antarctica.

Calving at the edges of floating ice shelves is based on divergence of the ice velocity field as described in Pollard and DeConto [2012b]. Sub-ice-shelf oceanic melting uses a simple parameterization, Eq. (17) of Pollard and DeConto [2012b], with a quadratic dependence on the temperature difference between "outer" ocean water and the ice-shelf base. However, in the present study the ocean temperature is taken from archived results of a coupled atmosphere-ocean General Circulation Model (A-OGCM) simulation of the last 22 ky [Liu et al., 2009]. Specifically, each ice grid point is assigned the value of the nearest OGCM cell at 437 m depth. For times between 20 ka and the present, we adopt the temperature at the corresponding time in the A-OGCM archive. For times before 20 ka, we use the A-OGCM temperature at the time in the 20-to-0 ka range that has the same deep-sea-core δ^{18}O value (a similar approach was adopted by Raymo and Mitrovica [2012], who used δ^{18}O values to prescribe pre-LGM ice distributions).

6.2.2 Sea-Level Model

Our simulations implement the theory and algorithms described in Kendall et al. [2005] and reviewed in Chapter 2 to compute gravitationally self-consistent variations in sea level following changes in the distribution of surface (grounded ice plus ocean) loading. The calculations incor-

porate the time-varying deformation of a rotating, Maxwell viscoelastic Earth model with depth dependent Earth structure, where the latter is comprised of an elastic lithosphere and a viscoelastic mantle. The sea-level algorithm accurately treats the inundation of water into marine sectors freed of grounded ice via a time-dependent tracking of shoreline geometry. The governing "sea-level equation" is solved using a pseudo-spectral numerical scheme described in Chapter 2 with all calculations performed up to spherical harmonic degree and order 512.

The sea-level theory requires as input, a model for viscoelastic Earth structure and a time history of ice loading. In regard to the former, we adopt the elastic and density structure of the Earth prescribed in the seismic model PREM [Dziewonski and Anderson, 1981]. The viscosity of the Earth's mantle is uncertain [Mitrovica, 1996]. The goal of this study is not to explore, in detail, the sensitivity to this uncertainty (we leave this for future work), but rather to highlight the impact of the physics introduced by coupling ice and sea-level models. To that end, we present results based on the same viscosity model as was adopted in the calculations in Chapters 2, 4 and 5. As discussed, the model has been shown to satisfy a wide spectrum of data related to glacial isostatic adjustment [e.g., Lambeck et al., 1998; Mitrovica and Forte, 2004] and is characterized by an elastic lithospheric thickness of 120 km and upper and lower mantle viscosities of 5×10^{20} Pa s and 5×10^{21} Pa s, respectively.

In the coupled simulation, changes in the distribution of grounded ice in Antarctica are passed to the sea-level model by the ice-sheet model. However, sea level in the vicinity of the AIS is impacted by changes in ice loading both locally and globally. Thus, in the results presented here, we adopt the ICE5G model [Peltier, 2004] to prescribe the space-time geometry of ice complexes outside of the AIS over the last 40 ky. ICE-5G is provided at spherical harmonic degree 256 resolution and we interpolate the ice grids in order to be consistent with the truncation of spherical harmonic degree 512 adopted in the sea-level calculations.

6.2.3 Coupling of Ice-Sheet and Sea-Level Models

Recall from Chapter 2 that the static sea-level theory assumes that the sea surface lies on a gravitational equipotential, and sea level (as discussed above) is defined globally as the difference in radial positions of the sea-surface equipotential and the solid surface. In oceanic regions, sea level is synonymous with ocean bathymetry, whereas over land, sea level is the negative of land elevation or topography.

To begin a coupled model simulation, the ice sheet model is initialized to its state at 40 ka in a previous long-term Pleistocene run of the uncoupled model [similar to the run in Pollard and DeConto, 2009]. The initial time 40 ka is chosen because (i) it allows a sufficient length of time for model adjustment between Antarctic LGM and subsequent retreat (∼20 to 10 ka) which is the focus of this paper, and (ii) it lies in a period of relative stability of the AIS glacial-interglacial cycle, with the ice sheet and bedrock reasonably close to equilibrium, as assumed for the initial state by the sea-level model.

Next, the ice-sheet model is run forward with a time step of 1 year for a period of ΔT (henceforth, the coupling interval). ΔT is typically chosen as 200 years. The ice model passes snapshots of ice cover at the beginning and end of the coupling interval to the sea-level model, which then computes the change in sea level across this interval. This change is passed back to the ice-sheet model, which uses it to update the bedrock elevation (a simple operation, because the vertical coordinate in the ice model is relative to the sea-surface gravitational equipotential, so "sea level" in the sea-level model is "$-1\times$ bedrock elevation" in the ice model). The ice-sheet model is then run through the next ΔT interval and the process is repeated. In simulations shown here, the coupled model was run for 40 ky, ending at the present.

Changes in sea level are passed from the sea-level model to the ice-sheet model, and vice versa for changes in the ice load. Near Antarctica, the spatial grid resolution of both models is similar

($\sim$ 40 km), and simple bilinear interpolation is used in passing the fields. Although the bedrock elevation has small-scale structure (mountain ranges, etc.), these features are close to invariant, and the changes in bedrock elevation computed by the sea-level model are relatively smooth. Indeed, simulations in which the resolution of the sea-level model was decreased by truncating the sea-level solver at spherical harmonic degree 256 did not alter the results significantly. We also tested the sensitivity of the coupled model to changes in the coupling interval and found that the results were insensitive to a reduction in this interval by a factor of 4.

The coupled model requires a map of bedrock topography both globally (for the sea-level model) and in the vicinity of the Antarctic Ice Sheet (for the ice-sheet model) at the start of the simulation. Since the topography at 40 ka is unknown at the outset, we employ an iterative method to solve for it. Specifically, we begin by making a guess for the initial topography (from a previous uncoupled Pleistocene run mentioned above) and running the coupled model forward to the present. We then take the difference between the predicted present-day topography and the observed topography (ETOPO globally, and ALBMAPv1 under the AIS), use this difference to correct the initial guess for topography at 40 ka, and run the coupled model again to the present. The process is repeated until the predicted present-day topography converges to the observed topography within a prescribed tolerance [Kendall et al., 2005].

6.3 Results

6.3.1 Coupled Ice Sheet - Sea Level Model Results

The coupled ice sheet - sea level model predicts changes in Antarctic ice distribution and global sea level throughout the 40 ky simulation. Figures 6.1A-D show snapshots of the ice distribution at times intended to sample phases of: maximum glacial extent (20 ka), periods of active deglaciation (15 ka, 10 ka), and a period of relatively stable geometry (5 ka). Figure 6.1 also shows the associated

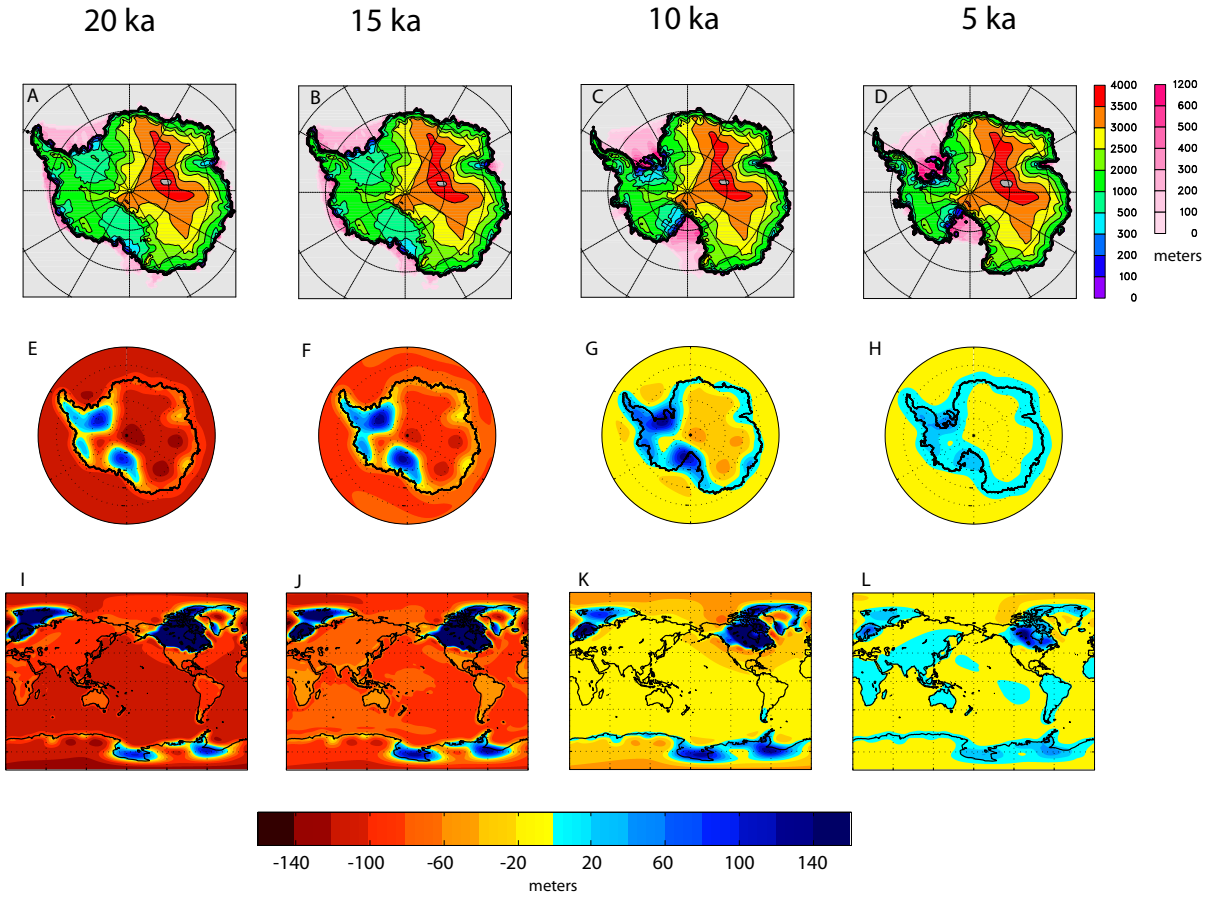

Figure 6.1: Evolution of the coupled ice sheet - sea level model since LGM. (A-D) Ice thickness in meters in Antarctica, at times specified above each frame. Grounded ice-surface elevation and floating ice thickness are shown by the color scales on the right. (E-L) Sea level relative to the modern (in meters) computed in the coupled simulation, plotted over Antarctica (E-H) and globally (I-L). Scale for relative sea-level variations is given at bottom.

relative sea-level variation for each of the time slices (i.e., sea level at each time relative to the present day) for the Antarctic (Figs. 6.1E-H) and the globe (Figs. 6.1I-L). Note that this is the total sea-level change due to both the modeled AIS and the evolution of Northern Hemisphere ice sheets prescribed from the ICE5G reconstruction [Peltier, 2004]. The solid blue line in Figure 6.2 is a time series of the volume of grounded ice in Antarctica over the full 40 ky of this simulation.

A grasp of the physics governing post-glacial sea-level change is essential in understanding how

sea-level changes impact ice sheet dynamics. We summarize the main elements of post-glacial sea-level change here; in Chapter 2.4 we provided a more detailed discussion using the results of an illustrative suite of post-glacial sea-level calculations.

The physics associated with global scale sea-level variations (Figs. 6.1I-L) is relatively straightforward. Regions once covered by ice (or excess ice) experience a large amplitude uplift of the crust and a pronounced, monotonic sea-level fall. Surrounding these regions are the peripheral bulges, where post-LGM crustal subsidence contributes a component of sea-level rise. For time windows that include periods of active deglaciation (Figs. 6.1I-K), the signal in both of the aforementioned regions is modified by several processes, notably a global-scale sea-level rise due to the addition of melt water to the oceans and a sea-level fall related to the diminished gravitational attraction of the ice sheets. For time windows after the main phase of deglaciation (Figs.!6.1K-L), the sea-level rise at the periphery of the ice centers is dominated by subsidence of the solid surface. Away from these near-field regions, and during the deglaciation phase, sea-level rise is dominated by the addition of meltwater to the oceans and the gravitationally driven migration of water from the near-field regions (Figs. 6.1I-K). Equatorial regions are characterized by $\sim$120 m, $\sim$60 m and $\sim$10 m of sea-level rise over the last 20 ky, 15 ky and 10 ky, respectively. Once most global ice-sheet retreat ceases, the predicted far-field sea-level change reflects the combined effects of a minor amount of sea-level rise associated with the residual addition of melt water to the oceans, solid surface uplift (and sea-level fall) over continents due to ongoing ocean-loading effects, and a broad migration of water toward the subsiding peripheral bulges (Figs. 6.1K-L).

The general physics of GIA in the Antarctic, which has been the focus of significant research [e.g., Ivins and James, 2005; Simon et al., 2010; Whitehouse et al., 2012b; Ivins et al., 2013], is also evident in our predictions of relative sea-level change over the region, which show significant geographic variability (Figs. 6.1E-H). The main centers of deglaciation, over the West Antarctic,

are characterized by large amplitude, monotonic sea-level fall. During the deglaciation phase, the East Antarctic, and a strip of land roughly half way between the Ross and Weddell Seas in the West, experience a sea-level rise (Figs. 6.1E, F). This rise is a complex combination of a number of processes, including subsidence of the bulges at the periphery of the melting centers (which contributes a sea-level rise), a drawdown of the sea surface as the gravitational attraction toward the WAIS decreases (sea-level fall), a sea-level rise associated with meltwater entering the ocean, and ocean loading effects along the margins of the continent, which tilt the solid surface upward onshore (sea-level fall) and downward offshore (sea-level rise). The ocean loading and peripheral bulge effects give rise to the relatively large geographic gradients in the sea-level predictions along the coastline of the East Antarctic. These effects are particularly dominant at the end of, and after, the main deglaciation phase (Fig. 6.1G and particularly 6.1H).

6.3.2 Comparison of Uncoupled and Coupled Model Simulations

In this section, we compare the timing and extent of ice-sheet retreat over the deglaciation phase predicted by the coupled ice sheet - sea level model (Fig. 6.1) and the unmodified Pollard and DeConto [2012b] ice-sheet model (henceforth, the "uncoupled model"). As discussed in Section 6.2.1, there are two main differences between the coupled and uncoupled models in regard to their treatment of sea-level change at the grounding line: (1) the coupled model incorporates a more sophisticated treatment of deformation of the solid Earth that captures the full, multi-normal mode response of a viscoelastic planet, whereas the uncoupled model adopts an adjustment with a single exponential decay time that is prescribed and fixed for all runs. In addition, elastic effects in the uncoupled model are only included through a flexural filtering of the viscous response to account for the presence of a lithosphere; (2) the uncoupled model assumes that the shape of the sea surface is fixed, and the height of this surface shifts up and down to account for changes in global ice volume. In

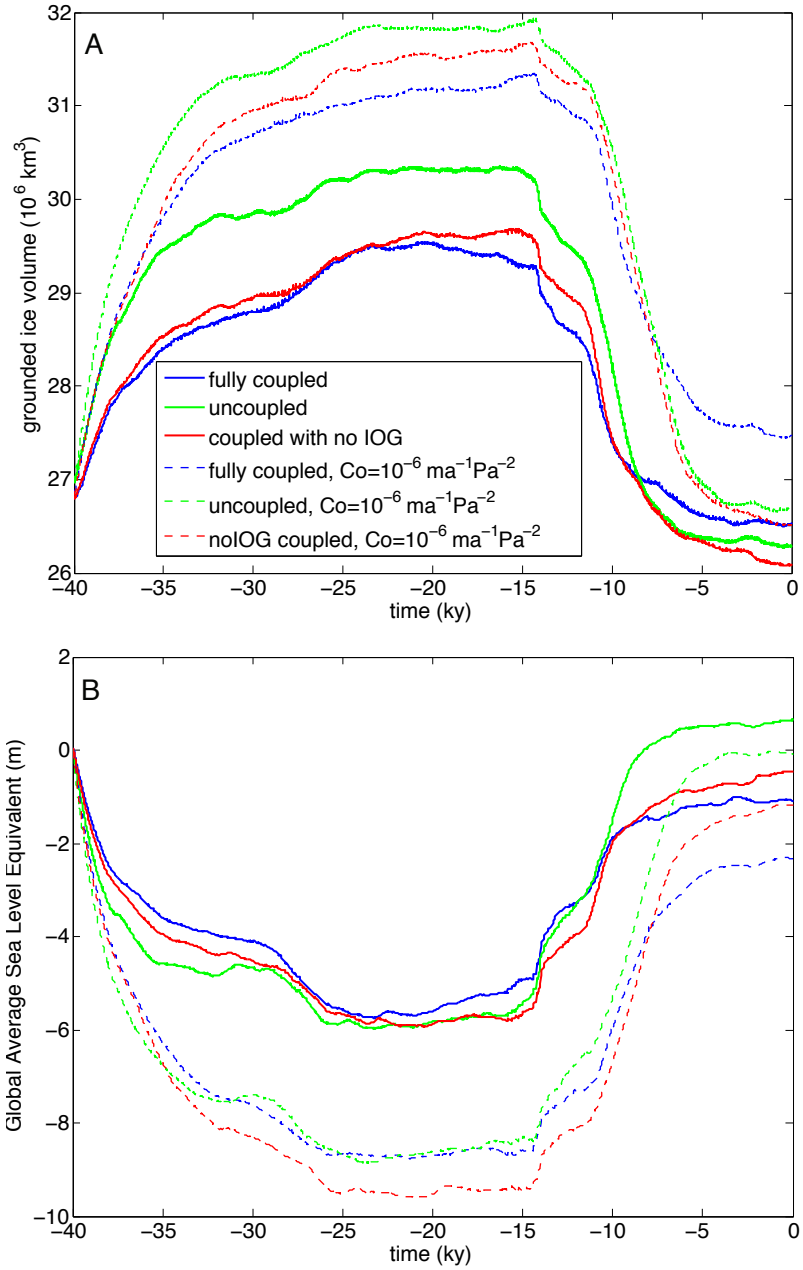

Figure 6.2: Changes in Antarctic grounded ice volume as a function of time over the last 40 ky. (A) Time series of total grounded Antarctic ice volume (in 10^6 km^3). (B) Time series of equivalent global mean (eustatic) sea-level change relative to the start of the simulation at 40 ka (in meters), calculated by taking the volume of grounded ice above floatation thickness, multiplying by the ratio of ice and water densities, and dividing by the area of the modern ocean. Note that this quantity does not have an exact 1-to-1 relationship with the total grounded volume plotted in (A). Solid curves show simulations with the fully coupled ice sheet - sea level model (blue curve), the uncoupled model (green curve), and the coupled model with an approximate treatment of sea-surface height changes (red curve, "noIOG"). The dashed curves are analogous with the solid, but with basal sliding coefficients in modern oceanic regions reduced from $C_o = 10^{-5}$ to $C_o = 10^{-6}$ m a^{-1} Pa^{-2}.

contrast, the coupled model incorporates gravitationally self-consistent perturbations in the shape of the sea-surface equipotential associated with both the redistributions of the surface mass (ice plus ocean) load and viscoelastic deformation of the solid Earth. The model invokes conservation of mass to constrain any geographically uniform shift in the height of the equipotential.

Figure 6.3 shows five snapshots in time ranging from 15 ka to present for the coupled (Figs. 6.3A-E) and uncoupled (Figs. 6.3F-J) simulations. The remaining frames show differences in the extent (Figs. 6.3K-O) and thickness (Figs. 6.3P-T) of grounded ice between the two simulations. The AIS volume through time for the uncoupled simulation is shown by the solid green line in Figure 6.2, which can be compared with the corresponding result for the coupled simulation (solid blue line).

The sea-level coupling acts to slow down the advance of the WAIS toward and during maximum ice conditions, and the result is a smaller WAIS during this phase (Fig. 6.2). The coupling also slows the subsequent retreat of the WAIS, relative to the uncoupled simulation, for a time period extending from the LGM to ∼6 ka (Fig. 6.2). This general behavior confirms, for these 3-D ice-sheet simulations, our earlier conclusions based on both an equilibrium marine ice-sheet stability theory [Gomez et al., 2010a] and 1-D ice-sheet simulations [Gomez et al., 2012]; namely, that the sea-level coupling is a negative feedback for grounding-line migration, and acts to stabilize the volume of a marine-based ice sheet.

These effects are also seen in the differences in the extent and thickness of grounded ice between the two simulations. At 15 ka, the uncoupled simulation predicts more extensive ice cover than the coupled model simulation along the coastline of the Antarctic (Fig. 6.3K), with the difference in thickness reaching ∼1 km (Fig. 6.3P). As time progresses, the less stable ice sheet in the uncoupled simulation retreats more quickly than in the coupled case, and by 8 ka, the coupled simulation predicts more extensive and thicker (by ∼500 m) ice cover in both the Ross and Ronne grounding zones (Fig. 6.3N, 6.3S). We conclude on the basis of these results that the self-stabilization mecha-

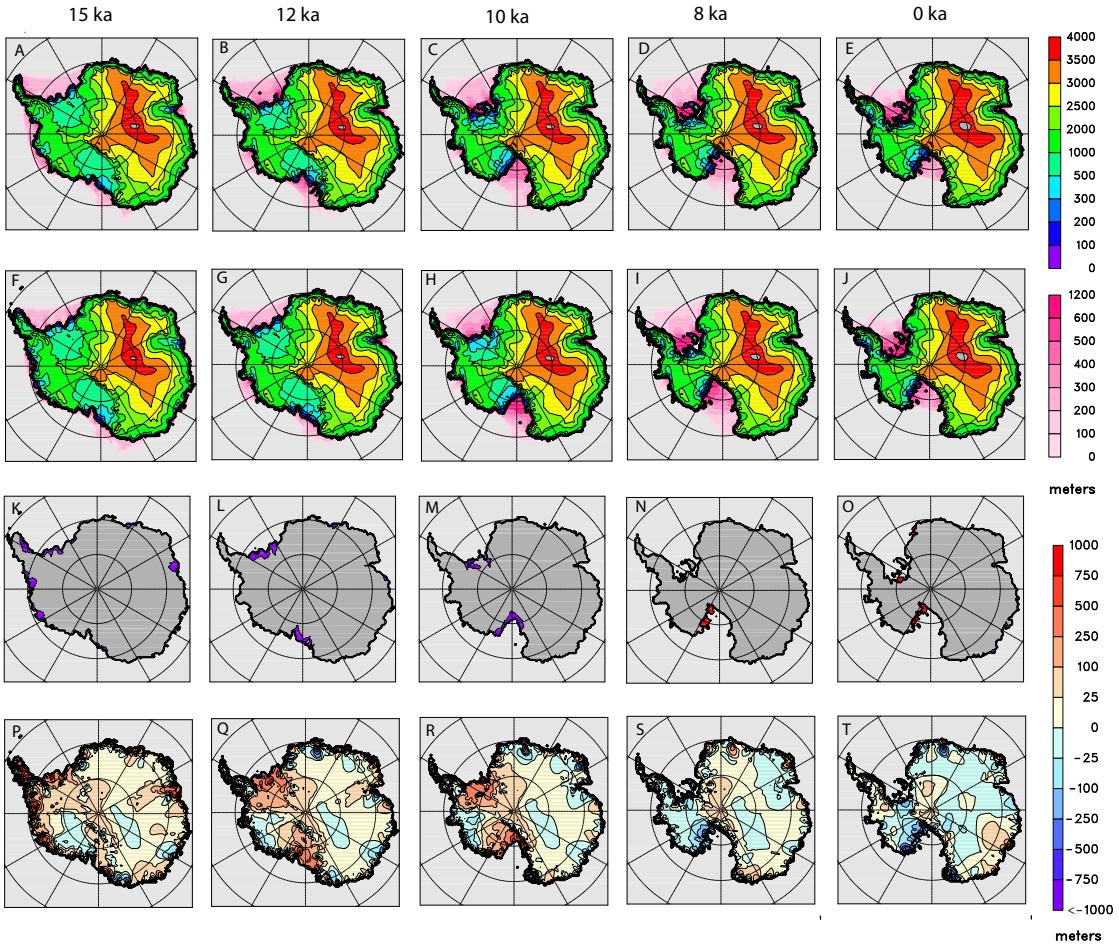

Figure 6.3: Comparison of ice distributions over the last 15 ky predicted using coupled and uncoupled models. (A-J) Snapshots in time (label at top) of grounded ice-surface elevation and floating ice thickness in meters, as indicated by the upper and middle color scales on the right, respectively. (A-E) Using the coupled model. (F-J) Using the uncoupled model. (K-O) Differences in grounded ice extent between the coupled and uncoupled model results. Areas covered by grounded ice in the uncoupled model but not in the coupled model are shown in purple, while the reverse are shown in red. (P-T) Differences in grounded ice thickness in meters (uncoupled minus coupled models), as indicated by the color scale on the lower right.

nism (i.e., the feedback of sea-level changes into ice-sheet stability) identified in earlier work [Gomez et al., 2010a, 2012, Chapters 4 and 5] is a universal property of grounded sectors of marine-based ice sheets.

As noted above, the differences between the uncoupled and coupled model runs are due to the treatments of the perturbation in both surfaces that bound sea level: The sea surface and the solid surface. We must emphasize that these treatments are not independent. Solid surface deformation is driven by ice and ocean load changes, and the latter is clearly a function of the treatment of the sea-surface height. Nevertheless, in the following, we attempt to isolate and identify the effects of the sea-surface height treatment, by performing an additional coupled run with ice-ocean gravitational attraction turned off (called "noIOG" below, for no Ice Ocean Gravity). Further details on the implementation of this approximation are provided in Appendix A.

Figures 6.4A-E show the ice distribution over the last 10 ky of the coupled simulation (i.e., as in Fig. 6.3C-E). In contrast, Figures 6.4F-J show snapshots from the noIOG simulation, in which the sea-surface height changes in the coupled model are replaced by a geographically uniform shift that represents only the globally averaged sea-level change associated with the time-varying global ice volume budget. The simulation includes solid Earth deformation driven by both the changing ice load and the geographically uniform ocean-load change. The final row in Figure 6.4 shows differences in ice extent from the fully coupled model. The time series of ice volume for the noIOG simulation is given in Figure 6.2 (solid red line).

The approximate treatment of the sea-surface height variation weakens the stabilizing influence of sea-level changes at the grounding line since it ignores the gravitational effects of the changing ice load. These gravitational effects are most prominent during rapid ice load changes. From 10 to 7 ka in Figure 6.4, while the ice sheet is rapidly melting, the coupled (gravitationally self-consistent) simulation predicts a drawdown of the sea surface at grounding lines in the West

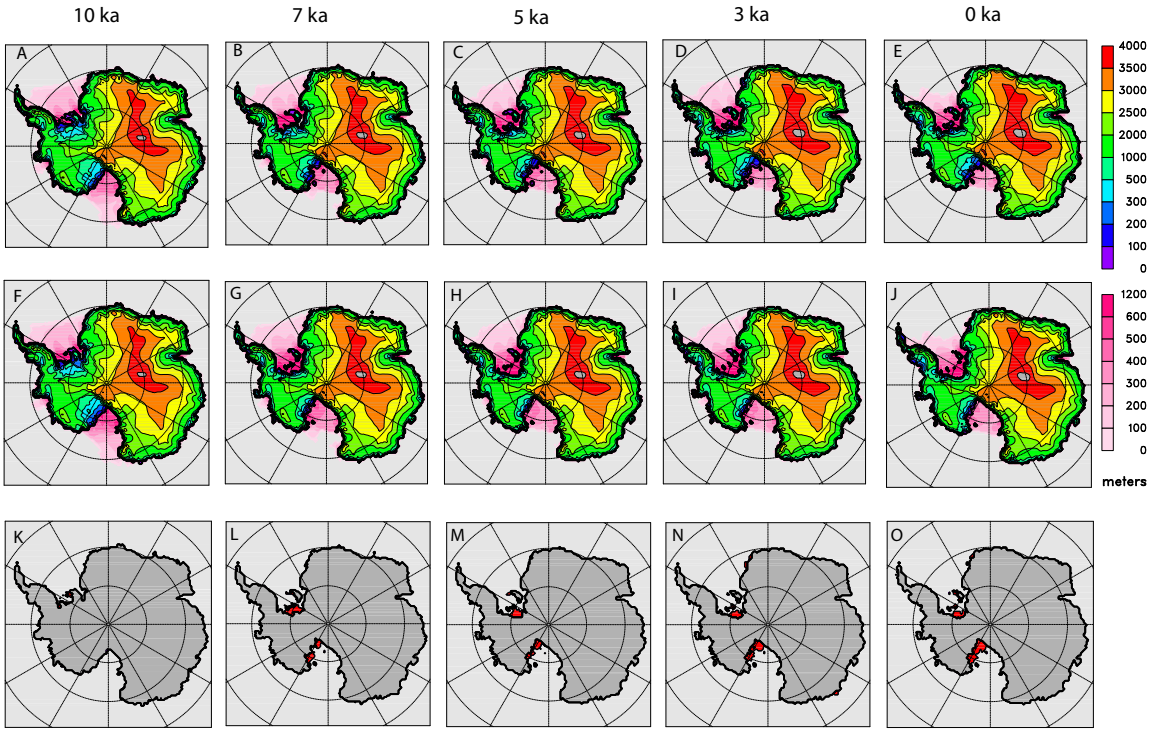

Figure 6.4: Impact of the treatment of sea-surface height changes on ice distribution. (A-J) Snapshots in time (labels at top) of grounded ice surface elevation and floating ice thickness in meters, as indicated by the upper and lower color scales on the right, respectively. (A-E) Using the standard coupled model. (F-J) Using the coupled model with an approximate treatment of sea-surface height changes ("noIOG"). (K-O) Differences in grounded ice extent between the two simulations. Areas covered by grounded ice in the standard coupled model but not in the noIOG model are shown in red (the reverse does nor occur).

Antarctic, thereby reducing ice flux and slowing grounding-line retreat in this region. This component of the stabilization accounts for the large differences in the two simulations over this 3 ky time period (Figs. 6.4K-L; Fig. 6.2). As the deglaciation slows, the perturbation to the sea-surface height in the fully coupled model is reduced, and differences between the two simulations remain relatively stationary (Figs. 6.4M-O).

6.3.3 Sliding Coefficients and Total Volume Change

The slipperiness of the bedrock beneath the AIS exerts a considerable control on the total volume of ice at LGM. A sticky bed inhibits the flow of ice, and therefore the volume of grounded ice should increase as the slipperiness of the bed is reduced. In our simulations, slipperiness of the bed is represented by the basal sliding coefficient in a Weertman-type law relating sliding velocity to basal shear stress. As discussed in Section 6.2.1, basal sliding coefficients under the grounded areas of the modern AIS have been deduced in an inverse procedure constrained by observed surface ice elevations [Pollard and DeConto, 2012a]. However, basal sliding coefficients in modern oceanic regions (floating ice shelves and continental shelves), over which the grounding line migrates during periods of glacial expansion, are much less constrained [Pollard and DeConto, 2012b].

The coupled simulations described thus far were performed using a sliding coefficient in modern oceanic regions of 10^{-5} m a^{-1} Pa^{-2}. This value is representative of deformable sediment as deduced by the inversion procedure for grounded ice streaming areas of the Siple Coast. In Figures 6.5A-E we show time slices for a coupled simulation in which the sliding coefficient in modern oceanic regions is decreased by an order of magnitude, to 10^{-6} m a^{-1} Pa^{-2}. This is still relatively slippery, compared to hard-bedrock values of 10^{-10} m $a^{-1}Pa^{-2}$ [Pollard and DeConto, 2012a]. The dashed blue line in Figure 6.2 is the time series of Antarctic ice volume for this simulation. Figures 6.5A-E can be compared to Figures 6.3A-E, and the dashed blue line to the solid blue in Figure 6.2, to consider the

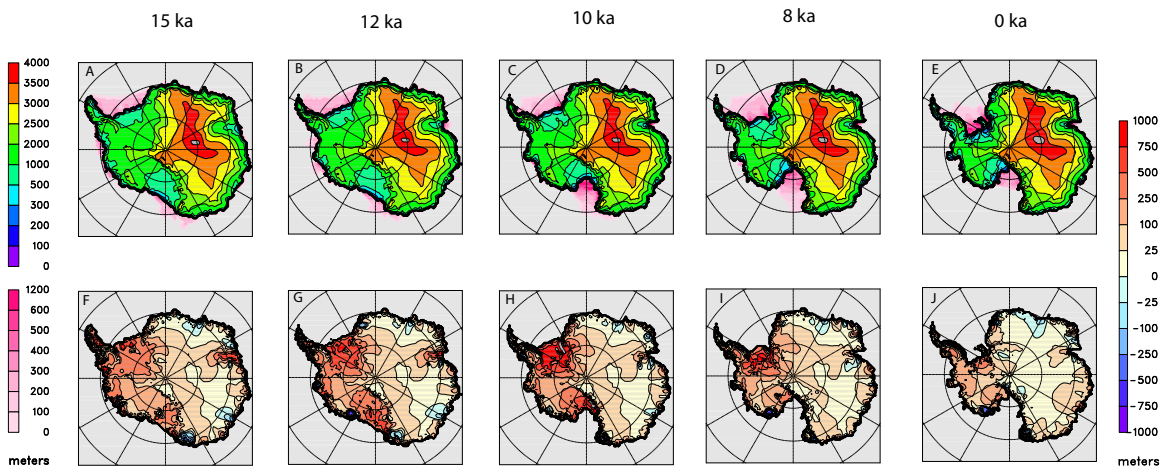

Figure 6.5: Impact of decreased basal sliding on ice distribution and volume. (A-E) Snapshots in time (label at top) of grounded ice-surface elevation and floating ice thickness in meters, shown by the upper and lower color scales on the left, respectively, using the coupled model with basal sliding coefficients in modern oceanic regions reduced to 10^{-6} m a^{-1} Pa^{-2} (from the standard coupled model value of 10^{-5} m a^{-1} Pa^{-2}). Color scales are as in Figs. 6.1, 6.3 and 6.4. (F-J) Differences in grounded ice thickness from the standard coupled model (shown in Figs. 6.3A-E) in meters (i.e., less slippery minus slippery bed simulations), as indicated in the color scale on the right.

impact of decreasing the slipperiness of the bed outside the present-day grounding line. The less-slippery bed simulation is characterized by significantly more ice throughout the 40 ky simulation, ending in a modern state with somewhat greater volume than observed. Finally, Figures 6.5F-J show the difference in ice thickness between the two simulations. During the deglaciation, in the time window from 12 to 10 ka, this difference can exceed 1 km over the present day location of the Weddell and Ross Seas.

Figure 6.2 also shows time series of Antarctic ice volume in the case of an uncoupled run (dashed green line) and the noIOG run (dashed red line) with the smaller sliding coefficient. As was the case for the solid lines, the dashed lines indicate that the noIOG simulation (i.e., the model run in which gravitational effect on the sea surface is removed) provides an intermediate level of stabilization between the coupled and uncoupled runs. A comparison of the solid lines and the dashed lines shows that the importance of this gravitational effect (the difference between the red and blue lines) relative to the approximate treatment of solid Earth deformation (difference between the green and red lines) depends on the details of the ice distribution, which in turn depends on the adopted sliding coefficient (among other factors).

6.4 Preliminary Comparison to Relative Sea Level and Modern Uplift Rate Data

Our coupled model simulation is driven by the physics incorporated into the ice-sheet and sea-level models and it has not been tuned to fit geological and geodetic constraints on glacial isostatic adjustment. (We note that in running the coupled model, we have used parameter settings from previous versions of both the sea-level and uncoupled ice-sheet components). The model can therefore be tested, a-posteriori, by comparing the results to local observations related to glacial isostatic adjustment.

In this section, we present a preliminary comparison of our predictions of site-specific relative

sea-level (RSL) histories (Fig. 6.6) and present-day uplift rates (Fig. 6.7) to relevant observational data sets [Roberts et al., 2011; Thomas et al., 2011; Briggs and Tarasov, 2013]. The comparison shown in each of these figures involves the standard coupled model, the coupled model with a sliding coefficient of 10^{-6} m $a^{-1}Pa^{-2}$ in modern oceanic regions, and the uncoupled model.

The three model simulations provide comparable fits to the RSL histories in the Antarctic region (Fig. 6.6). The existing RSL data set does not appear to robustly discriminate between the coupled and uncoupled simulations. While we have adopted a single Earth model to highlight the ice sheet-sea level coupling in this study, the fits obtained from our coupled simulations are comparable to the fit achieved in recent uncoupled model simulations where the Earth model was varied to obtain a best fit to the relative sea-level records [Whitehouse et al., 2012a,b].

Figure 6.7 summarizes the analysis of uplift rates in the Antarctic region estimated from GPS surveying and corrected for elastic uplift associated with recent melting [Thomas et al., 2011; Whitehouse et al., 2012b]. In this case, the standard coupled simulation provides a statistically improved fit over both the coupled simulation with a stickier bed within modern oceanic regions and the uncoupled simulation (see rms fits provided in Figs. 6.7G-I). In particular, the latter two simulations predict uplift rates at a significant number of sites that are well above the observed rates. In the Antarctic Peninsula and inland of the Ronne Ice Shelf, predicted uplift rates are progressively greater as one moves from the coupled model, to the uncoupled model and, finally, to the coupled model with stickier bed. This trend leads to progressively greater misfits between the modeled and observed uplift rates in this region. At sites northwest and northeast of the Ross Ice Shelf, the uncoupled model predicts significantly greater uplift rates, and is characterized by greater misfits to the observed rates, as compared to either of the coupled model runs. Note that fits to RSL and uplift rate data will be sensitive to the adopted Earth model. A preliminary consideration of this sensitivity is presented in the final remarks in Chapter 7 (Fig. 7.1).

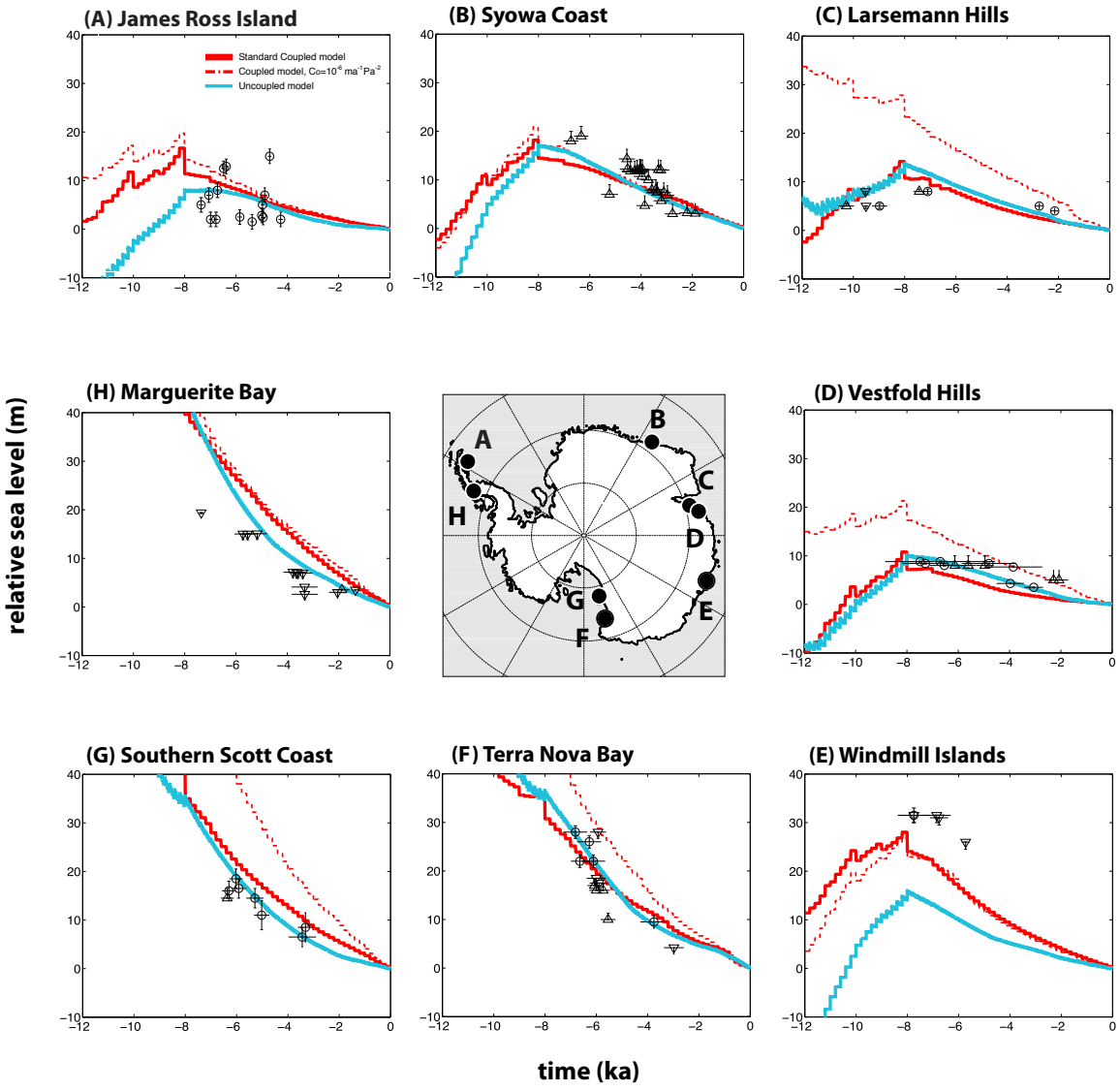

Figure 6.6: Comparison of RSL predictions generated from model simulations with observational constraints. Curves on each frame show RSL predictions at a given site (as labeled; location shown in middle frame) based on the coupled model (thick red lines), the coupled model with basal sliding coefficients in modern oceanic areas reduced to 10^{-6} m a^{-1} Pa^{-2} (thin dashed red lines), and the uncoupled model (blue lines). Black markers and error bars show field data from the compilation of Briggs and Tarasov [2013], except for James Ross Island, where the data are from Hjort et al. [1997] as discussed in Roberts et al. [2011]. Circular markers represent two-way constraints on sea level, and upward and downward pointing triangular markers represent one-way lower and upper bounds on sea level, respectively. For the one-way markers, error bars in the non-bounded direction are indeterminate.

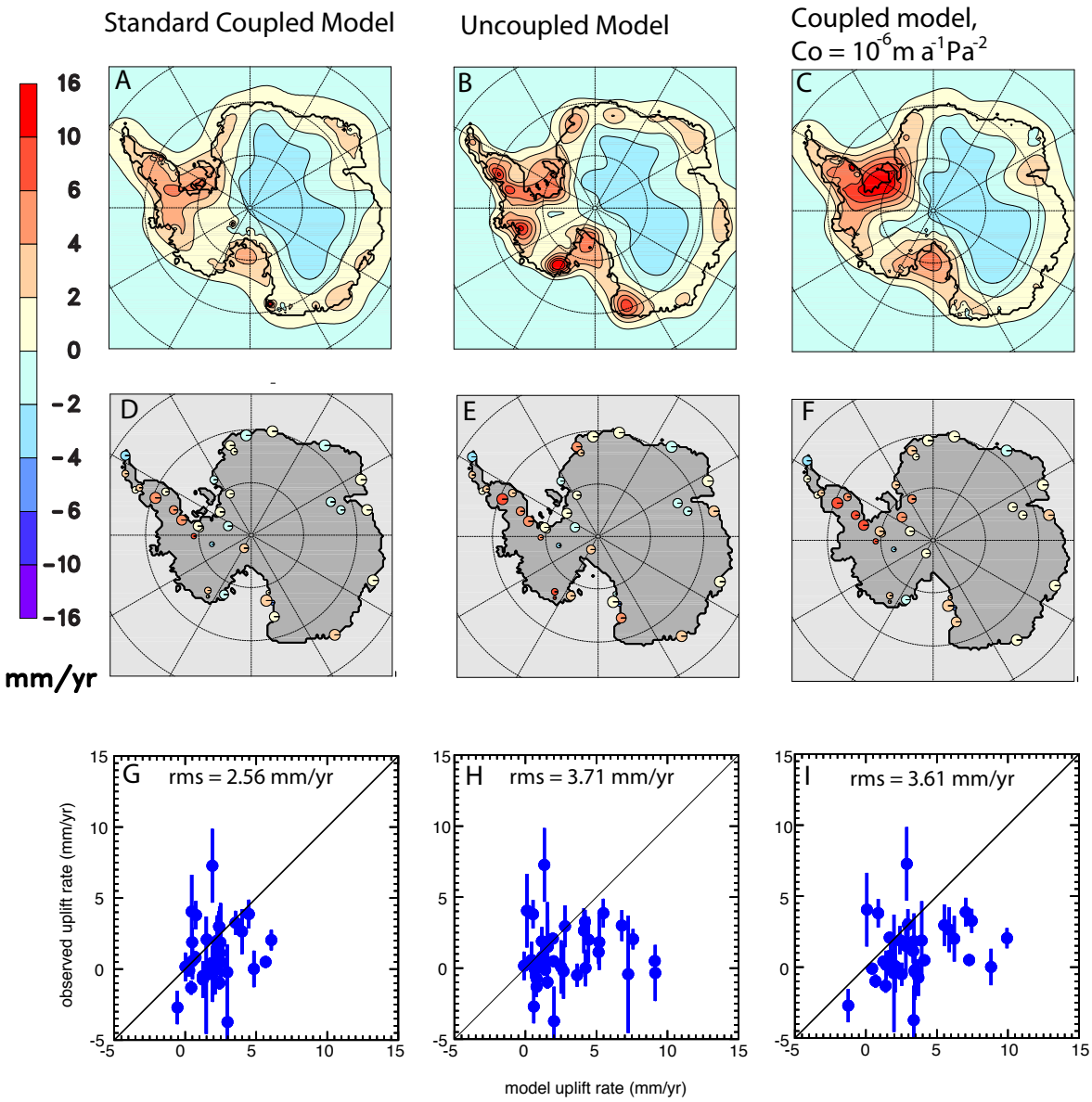

Figure 6.7: Comparison of model predicted and geodetically observed uplift rates. The latter are based on GPS measurements obtained at exposed bedrock sites, corrected for elastic uplift due to modern ice-mass flux (Thomas et al., 2011 main text and supplement; tabulated in Whitehouse et al., 2012b, see their Table S2). (A-C) Maps of model predicted uplift rates over Antarctica with color scale indicated on the left. (D-F) Misfit between modeled and observed uplift rates, following the color scale on the left, at the locations of the GPS sites. The size of the circles is proportional to the accuracy of the GPS estimate. (G-I) Scatter plots showing predicted versus observed uplift rates. Vertical bars show one-sigma observational uncertainties and rms fits are as indicated on the plots. Columns in the figure are distinguished on the basis of the simulation: (A, D, G) Coupled model. (B, E, H) Uncoupled model. (C, F, I) Coupled model with basal sliding coefficients in modern oceanic areas reduced to 10^{-6} m a^{-1} Pa^{-2}.

6.5 Conclusions

In earlier work based on steady state [Gomez et al., 2010a, Chapter 4] and 1-D [Gomez et al., 2012, Chapter 5] ice sheet models we showed that sea-level variations driven by local and regional ice-mass changes act to self-stabilize marine ice-sheet grounding lines. In this study, we have extended this work by coupling a 3-D ice sheet-shelf model with a gravitationally self-consistent treatment of post-glacial sea-level change, and have demonstrated that the sea-level stabilization is a universal property of marine-based ice sheets. Sea-level trends arising from the evolution of the 3-D ice-sheet model reflect the complex nature of the gravitational, deformational and rotational processes driving post-glacial sea-level change, and this complexity is, in turn, reflected in the detailed, site-specific impact of the sea-level coupling. The incorporation of the sea-level coupling can perturb ice thicknesses at sites close to AIS grounding lines by up to $\sim$1 km (Fig. 6.3), and reduce the integrated excess ice volume at LGM by $\sim 25\%$ (Fig. 6.2).

The contribution from Antarctica to globally averaged sea-level rise since the LGM is a matter of active debate. Recent GIA and ice-sheet modeling studies suggest that this contribution is $\sim$7-9 m in units of equivalent globally uniform sea-level change [Whitehouse et al., 2012a; King et al., 2013; Ivins et al., 2013], significantly lower than previous estimates that were closer to 20 m [e.g., Peltier, 2004]. Our calculations support the newer estimates, although our simulations indicate that the excess ice volume may be sensitive to the slipperiness of bed outside present-day grounding lines (Fig. 6.2). In any event, the lower estimates of AIS volume at LGM, if robust, have implications not only for climate simulations at this time, but also for the potential contribution of the AIS to subsequent, critical events in ice-age climate, such as Meltwater Pulse 1A.

We have focused on the impact of gravitationally self-consistent sea-surface height perturbations on the evolution of the 3-D Antarctic Ice Sheet model. A comparison of the uncoupled versus noIOG

simulations in Figure 6.2 (i.e., green lines versus associated red lines) provides a measure of the effect of approximating the full multi-normal mode response of the viscoelastic Earth model with a single decay time and elastic lithospheric flexure. Earlier studies have explored the sensitivity of ice-sheet models to the adopted bedrock response model [Le Meur and Huybrechts, 1996, 2001; van den Berg et al., 2008]. In accordance with these studies, we advocate the adoption of a full viscoelastic response, because in this case, the decay times of the normal modes, and their dependence on the spatial scale of the load, follows naturally from the adopted viscoelastic structure rather than from an ad-hoc tuning of a single decay time. This is particularly important given that the time-dependent evolution of an ice sheet involves a broad range of spatial scales (e.g., Fig. 6.1).

We considered only a single viscoelastic Earth model in the simulations described above. As discussed above, in Figure 7.1, we present results from a preliminary sensitivity analysis in which we vary the parameters defining the Earth model (e.g., lithospheric thickness, upper and lower mantle viscosities) across plausible ranges. Seismic tomography indicates slower than average wave speeds in the asthenosphere beneath the WAIS, suggesting the presence of a low viscosity zone in this region, as well as a thinner lithosphere, relative to mantle below the EAIS [e.g., Morelli and Danesi, 2004; Kaufmann et al., 2005]. Accordingly, in future work, we will also consider the impact of this level of 3-D Earth structure, and other regional rheological complexities [Ivins et al., 2011; Nield et al., 2012], on the coupled model simulations.

The potential importance of the sea-level feedback described here indicates that it would be useful to reassess AIS stability during other time periods. To this end, our future work will consider, following Pollard and DeConto [2009], the evolution of the AIS over the entire Plio-Pleistocene time period, as well as the response of the ice sheet to ongoing and future climate warming scenarios. In addition, it would be worthwhile to investigate the stability of marine sectors of Northern Hemisphere ice sheets during the last glacial cycle of the ice age.

Chapter 7

Final Remarks

The work in this thesis highlights the importance of taking an integrated view of ice sheet, sea level, and solid Earth interactions. In Chapter 2, I presented a generalized theory for computing changes in sea level and solid Earth deformation following variations in the distribution of grounded ice cover and characterized the physical effects that contribute to patterns of sea-level change that arise on different timescales. This discussion emphasizes that the unique sea-level "fingerprints" that arise from different ice mass changes can be used as a tool to investigate a broad range of problems related to ice-age climate. As an example, in Chapter 3, I used the sea-level patterns that arise from a recent model for the retreat of North American ice cover during Meltwater Pulse 1A to revisit the possible role of this retreat in the meltwater pulse. In Chapter 3 and throughout this thesis, I showed that accurate modeling of both the distribution of ice through time and the associated sea-level changes are important for the analysis and interpretation of relative sea-level records and glacial isostatic adjustment data.

In the remaining chapters, I coupled the generalized sea-level theory to a series of increasingly complex and realistic ice-sheet models, to determine the impact that sea-level changes at the grounding line have on marine ice sheet stability and dynamics. In Chapter 4, I incorporated gravitationally self-consistent sea-level changes into the canonical model of equilibrium (time-independent)

marine ice sheet stability [Weertman, 1974] and showed that these sea-level changes have a stabilizing influence on marine ice sheets. This work demonstrated that the so-called Marine Ice Sheet Stability Hypothesis, which posits that grounded marine ice-sheets resting on reverse bed slopes are inherently unstable, is not universally valid. In Chapter 5, I extended this equilibrium analysis to consider the influence of sea-level changes on the timescale of ice sheet retreat by coupling a global sea-level model to a one-dimensional, dynamic ice-sheet model. I demonstrated that the sea-level fall in the vicinity of a retreating ice sheet acts to slow down, and in some cases, halt grounding-line migration. Finally, after having explored the physics of the coupling using simplified ice sheet and bedrock geometries, in Chapter 6, I coupled a realistic Antarctic ice sheet - shelf model [Pollard and DeConto, 2012b] to a gravitationally self-consistent global sea-level model. I applied the coupled model to simulated the retreat of the AIS through the last deglaciation. A comparison of simulations with and without the sea-level coupling reinforced the conclusions of Chapters 4 and 5 in a more realistic setting, and showed that the sea-level feedback is universal and that it has a significant impact on rate and extent of ice-sheet retreat and advance. I conclude that the influence of sea-level changes on marine ice-sheet stability and dynamics should be accounted for in models of marine ice-sheet evolution.

In Chapter 6, I adopted a single model to describe radial Earth structure. However, internal Earth structure is characterized by significant lateral variability. Figure 7.1A shows seismic tomographic images at 80, 120, 160 and 200 km depths beneath Antarctica. While the East Antarctic sits on a stable craton characterized by a thick lithosphere, the West Antarctic is underlain by a large continental rift system with a thinned lithosphere on top of a thin zone of hot, low viscosity material [Morelli and Danesi, 2004; Kaufmann et al., 2005]. Such large lateral differences in Earth structure across the Antarctic continent suggests that an exploration of the sensitivity of results presented in Chapter 6 to variations in Earth model parameters is warranted. Figure 7.1B-E shows

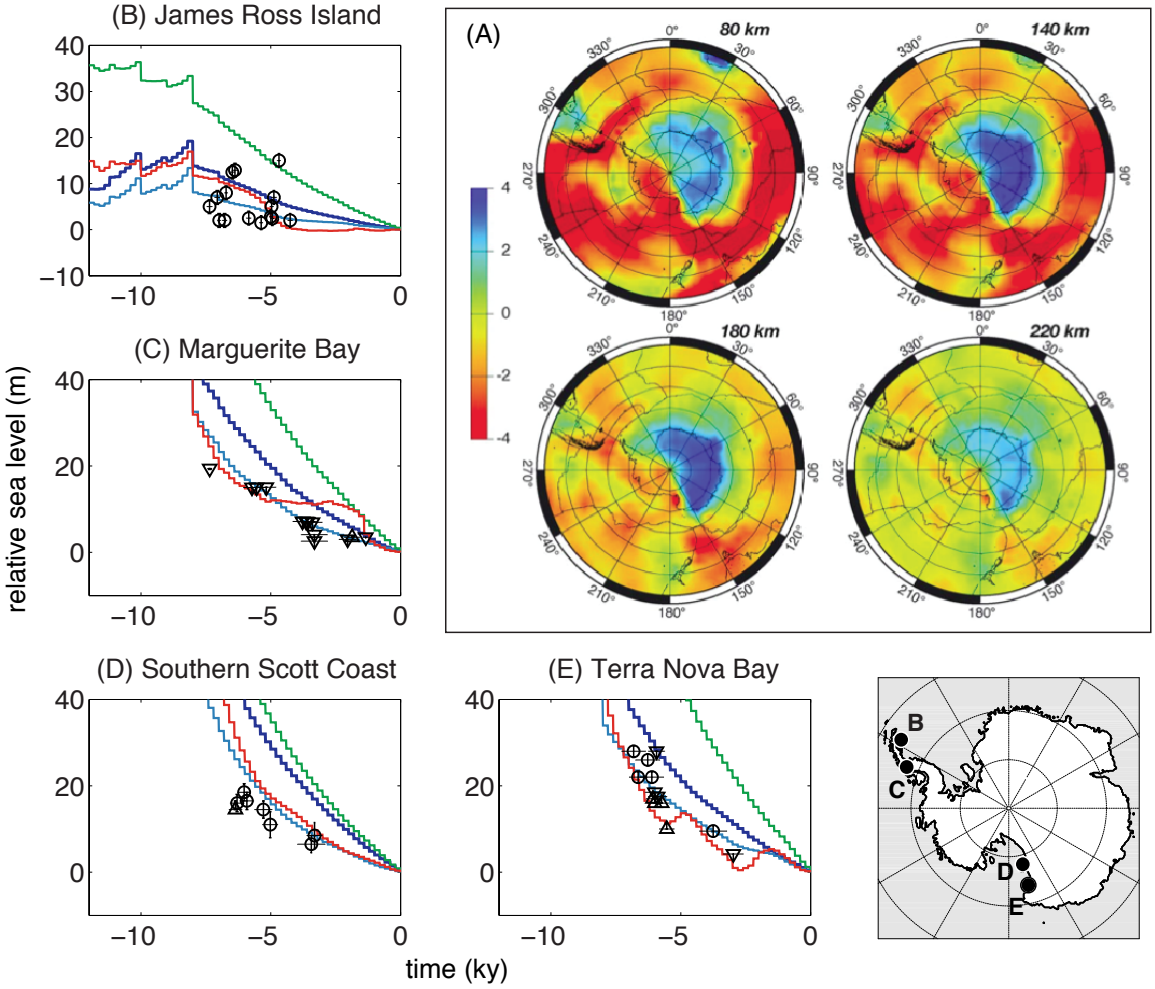

Figure 7.1: Comparison of RSL predictions generated from coupled model simulations with observational constraints for a range of Earth model parameters. (A) Plots taken directly from Morelli and Danesi [2004]'s Figure 2 showing Earth structure beneath Antarctica. Percent variations in shear wave velocity are plotted at 80 km, 140 km, 180 km and 220 km depths as labeled. (B-E) Curves show RSL predictions at a given site (as labeled; location shown on the map at bottom right) based on the coupled model with basal sliding coefficients in modern oceanic areas set to 10^{-6} m a^{-1} Pa^{-2} and Earth models characterized by lithospheric thickness and upper and lower viscosities set to: 120 km, 5×10^{20} Pa s and 5×10^{21} Pa s (dark blue lines); 50 km, 5×10^{20} Pa s and 5×10^{21} Pa s (green lines); 120 km, 2×10^{20} Pa s and 5×10^{21} Pa s (light blue lines); and 50 km, 5×10^{20} Pa s and 5×10^{21} Pa s, respectively with a low viscosity zone of 10^{19} Pa s inserted below the thin lithosphere down to 200 km depth (red lines). As in Figure 6.6, black markers and error bars show field data from the compilation of Briggs and Tarasov [2013], except for James Ross Island, where the data are from Hjort et al. [1997] as discussed in Roberts et al. [2011].

the results of a preliminary investigation of this sensitivity. In each plot, relative sea-level data and predictions based on the standard Earth model from Chapter 6 (blue lines) are compared to: A model with a thinned lithosphere of 50 km (green lines); a model with a less viscous upper mantle of 2×10^{20} Pa s (light blue lines); and a model with a 50 km thick lithosphere underlain by a low viscosity zone of 10^{19} Pa s extending down to 200 km depth (red lines). The last of these models is similar to the Earth structure depicted beneath the WAIS in Figure 7.1A. The results are clearly sensitive to viscosity in the upper mantle, and those that adopt either a low viscosity whole upper mantle, or a thin low viscosity zone at the base of the lithosphere, show improved fits to the relative sea-level data in the West Antarctic. (Note that curves over the East Antarctic were not shown in Figure 7.1 since a very low viscosity model may not be appropriate there.)

Varying the viscoelastic Earth model parameters impacts relative sea-level predictions by: 1) altering the timing and geometry of load-induced Earth deformation (and thus sea level); and 2) perturbing, via the sea-level feedback, the timing and extent of the ice-sheet retreat. A coupled ice sheet - sea level model that captures the full and complex interaction between ice distribution and Earth deformation is necessary to rigorously explore this connectivity. In future work, I will couple a 3-D sea-level model to an ice-sheet model to investigate the impact of these lateral variations in Earth structure over the Antarctic continent on ice-sheet and sea-level changes.

In Chapter 3, we discussed the issue of constraining the contributions from various ice sheets to sea-level rise during the last deglaciation. In particular, global sea-level records indicate that the Antarctic may have contributed significantly to Meltwater Pulse 1A, a large pulse of meltwater release that punctuated the deglaciation [Clark et al., 2002; Bassett, 2005]. This would imply that the AIS was significantly larger at LGM than at present. To the contrary, recent GIA and ice-sheet modeling studies [e.g., Whitehouse et al., 2012a; King et al., 2013; Ivins et al., 2013, Chapter 6] indicate that Antarctica likely contributed only ∼5-9 meters in units of equivalent globally uniform

sea-level rise during the last deglaciation. However, none of the latter studies employed Earth models that accurately reflect the lateral variability in viscoelastic structure underneath Antarctica. For example, the Whitehouse et al. [2012a] and King et al. [2013] studies identified a preferred Earth model with an upper mantle viscosity of 1×10^{21} Pa s on the basis of fits to sea-level data. This inference is higher than all GIA inferences of upper mantle viscosity over the last 15 years, and much higher than would be implied by the shear wave heterogeneity in Figure 7.1A.

The simulations in Figure 7.1B-E were performed with sliding coefficient of 10^{-6} m a^{-1} Pa^{-2}. As discussed in Chapter 6, this higher friction allows for increased ice volume at LGM equivalent to ~ 2 meters of global average sea-level relative to the standard coupled simulations in Chapter 6 (Figure 6.2). While predicted relative sea-level curves based on the standard Earth model misfit the observations (the blue lines in Figure 7.1B-E lie above the data), the simulations with reduced upper mantle viscosity (light blue lines) and a shallow low viscosity zone below a thin lithosphere (red lines) show better fits to the relative sea-level data. These preliminary results suggest that a larger LGM Antarctic ice volume may be plausible if paired with more realistic Earth structure, and this motivates an important direction for future work.

The importance of the interactions between marine ice-sheet dynamics and sea-level variations suggests that a coupled ice sheet - sea level model will be an important tool for exploring a suite of other ice-age climate problems. For example, in future work I will investigate AIS stability and evolution during other time periods, including the Pliocene Epoch when temperatures were warmer than today, and over the next century in response to climate warming scenarios. In addition, the coupled model can be adopted to investigate the stability of marine sectors of Northern Hemisphere ice sheets and the potential for inter-hemispheric teleconnections between ice sheets [e.g., Denton et al., 1986]. Finally, to date I have focussed on ice-sheet retreat, but the results in Figure 6.2 clearly demonstrate that the sea-level feedback also acts to dampen the advance of the grounding

line. Since there is a lag in the response of the Earth to ice sheet changes, there is a possibility for hysteretic behavior to arise. I plan to explore whether such behavior could be a possible alternative explanation for observed periodic, rapid fluctuations in ice extent during Dansgaard-Oeschger events.

Appendix A

Sea-Level Theory for no-IOG Calculations

In the main text, we perform simulations with the coupled ice sheet - sea level model in which we turn off the effects of ice-ocean gravitational attraction. We call these simulations "noIOG" for "no ice-ocean gravity". The purpose of these simulations is to isolate and assess the impact on the results of adopting an approximate treatment of sea-surface height deformation in the sea-level model. The "noIOG" simulations accounts for changes in elevation of the solid Earth in the same way as the fully coupled model, but assumes that the sea surface height rises and lowers uniformly as global ice volumes decrease and increase (as in the uncoupled model).

In the "noIOG" runs, the change in topography is given by the following modified version of equation 2.43 in Section 2.2.2:

$$\begin{aligned}\Delta R(\theta,\psi,t_j) = &-\sum_{l,m} T_l E_l \left[\rho_l \Delta I_{lm}(t_j) + \rho_W \Delta S^{eus}_{lm}(t_j)\right] Y_{lm}(\theta,\psi) \\ &-\sum_{l,m} T_l \sum_{n=0}^{j-1} \beta(l,t_n,t_j) \left[\rho_I \delta I_{lm}(t_n) + \rho_W \delta S^{eus}_{lm}(t_n)\right] Y_{lm}(\theta,\psi) \\ &-\Delta S^{eus}(t_j),\end{aligned} \tag{A.1}$$

where we zero out the Love numbers associated with deformation of the sea surface equipotential,

such that equations 2.38 and 2.39 in Section 2.2.2 become:

$$E_l = -h_l \tag{A.2}$$

and

$$\beta(l, t_n, t_j) = \sum_{k=1}^{K} \frac{-r_k^l}{s_k^l} \left[1 - e^{-s_k^l (t_j - t_n)}\right]. \tag{A.3}$$

$\Delta S^{eus}(t_j)$ is the global average, or "eustatic" sea-level change from the start of the simulation to time t_j. It is identical to the change in sea surface height adopted in uncoupled simulations. That is,

$$\Delta S^{eus}(t_j) = -\frac{\rho_I}{\rho_W} \frac{\Delta I_{00}^{gaf}(t_j)}{C_{00}(t_j)} C(\theta, \psi, t_j), \tag{A.4}$$

where ΔI_{00}^{gaf} is the (0,0) spherical harmonic component of the change in ice grounded above floatation, and C is the ocean function, as defined in Section 2.2, equation 2.4. $\Delta S_{lm}^{eus}(t_j)$ and $\delta S_{lm}^{eus}(t_j)$ represent spherical harmonic decompositions of the eustatic sea-level change from the start of the simulation to time t_j and over the time increment from t_{j-1} to t_j, respectively. All other variables and parameters are as defined in Section 2.2.

References

Andrews, J. T., Erlenkeuser, H., Tedesco, K., Aksu, A. E., Jull, A. J. T., 1994. Late Quaternary (Stage 2 and 3) Meltwater and Heinrich Events, Northwest Labrador Sea. Quat. Res. 41, 26–34.

Barber, D. C., Dyke, A., Hillaire-Marcel, C., Jennings, A. E., Andrews, J. T., Kerwin, M. W., Bilodeau, G., McNeely, R., Southon, J., Morehead, M. D., Gagnon, J. M., 1999. Forcing of the cold event of 8,200 years ago by catastrophic drainage of Laurentide lakes. Nature 400, 344–348.

Bard, E., Hamelin, B., Delanghe-Sabatier, D., 2010. Deglacial Meltwater Pulse 1B and Younger Dryas Sea Levels Revisited with Boreholes at Tahiti. Science 327, 1235–1237.

Bassett, S. E., 2005. Ice Sheet and Solid Earth Influences on Far-Field Sea-Level Histories. Science 309, 925–928.

Briggs, R., Pollard, D., Tarasov, L., 2013. A glacial systems model configured for large ensemble analysis of Antarctic deglaciation. The Cryosphere Discussions 7, 1533–1589.

Briggs, R. D., Tarasov, L., 2013. How to evaluate model-derived deglaciation chronologies: a case study using Antarctica. Quaternary Science Reviews 63, 109–127.

Carlson, A. E., 2009. Geochemical constraints on the Laurentide Ice Sheet contribution to Meltwater Pulse 1A. Quaternary Science Reviews 28, 1625–1630.

Clark, J. A., Lingle, C. S., 1977. Future sea-level changes due to West Antarctic ice sheet fluctuations. Nature 269, 206–209.

Clark, J. A., Primus, J. A., 1987. Sea-level changes resulting from future retreat of ice sheets: an effect of CO_2 warming of the climate. In: Tooley, M. J. (Ed.), Sea-level changes. The Institute of British Geographers Special Publications Series, pp. 356–370.

Clark, P. U., Mitrovica, J. X., Milne, G. A., Tamisiea, M. E., 2002. Sea-level fingerprinting as a direct test for the source of global meltwater pulse IA. Science 295, 2438–2441.

Conrad, C. P., Hager, B. H., 1997. Spatial variations in the rate of sea level rise caused by the presentday melting of glaciers and ice sheets. Geophysical Research Letters 24, 1503–1506.

Dahlen, F. A., 1976. The passive influence of the oceans upon the rotation of the Earth. Geophysical Journal International 46, 363–406.

Denton, G. H., Hughes, T. J., Karlén, W., 1986. Global ice-sheet system interlocked by sea level. Quaternary Research 26, 3–26.

Deschamps, P., Durand, N., Bard, E., Hamelin, B., Camoin, G., Thomas, A. L., Henderson, G. M., Okuno, J., Yokoyama, Y., 2012. Ice-sheet collapse and sea-level rise at the Bolling warming 14,600 years ago. Nature 483, 559–564.

Drouet, A. S., Docquier, D., Durand, G., Hindmarsh, R., Pattyn, F., Gagliardini, O., Zwinger, T., 2013. Grounding line transient response in marine ice sheet models. The Cryosphere 7, 395–406.

Dupont, T. K., 2005. Assessment of the importance of ice-shelf buttressing to ice-sheet flow. Geophysical Research Letters 32, L04503.

Dziewonski, A. M., Anderson, D. L., 1981. Preliminary reference Earth model. Physics of the earth and planetary interiors 25, 297–356.

Fairbanks, R. G., 1989. A 17,000-year glacio-eustatic sea level record: influence of glacial melting rates on the Younger Dryas event and deep-ocean circulation. Nature 342, 637–642.

Fairbanks, R. G., Charles, C. D., Wright, J. D., 1992. Origin of Global Meltwater Pulses. In: Radiocarbon after four decades. Springer New York, New York, NY, pp. 473–500.

Farrell, W. E., Clark, J. A., 1976. On postglacial sea level. Geophysical Journal of the Royal Astronomical Society 46, 647–667.

Gagliardini, O., Durand, G., Zwinger, T., Hindmarsh, R., Le Meur, E., 2010. Coupling of iceshelf melting and buttressing is a key process in icesheets dynamics. Geophysical Research Letters 37, L14501.

Gladstone, R. M., Payne, A. J., Cornford, S. L., 2013. Resolution requirements for grounding-line modelling: sensitivity to basal drag and ice-shelf buttressing. Annals of glaciology 53, 97–105.

Goldberg, D., Holland, D. M., Schoof, C., 2009. Grounding line movement and ice shelf buttressing in marine ice sheets. Journal of Geophysical Research 114, F04026.

Gomez, N., Mitrovica, J. X., Huybers, P., Clark, P. U., 2010a. Sea level as a stabilizing factor for marine-ice-sheet grounding lines. Nature Geoscience 3, 850–853.

Gomez, N., Mitrovica, J. X., Tamisiea, M. E., Clark, P. U., 2010b. A new projection of sea level change in response to collapse of marine sectors of the Antarctic Ice Sheet. Geophysical Journal International 180, 623–634.

Gomez, N., Pollard, D., Mitrovica, J. X., 2013. A 3-D coupled ice sheet - sea level model applied to Antarctica over the last 40 ky. Earth and Planetary Science Letters (in press).

Gomez, N., Pollard, D., Mitrovica, J. X., Huybers, P., Clark, P. U., 2012. Evolution of a coupled marine ice sheet–sea level model. Journal of Geophysical Research 117, F01013.

Gregoire, L. J., Payne, A. J., Valdes, P. J., 2012. Deglacial rapid sea level rises caused by ice-sheet saddle collapses. Nature 487, 219–222.

Gudmundsson, G. H., 2013. Ice-shelf buttressing and the stability of marine ice sheets. The Cryosphere 7, 647–655.

Gudmundsson, G. H., Krug, J., Durand, G., Favier, L., Gagliardini, O., 2012. The stability of grounding lines on retrograde slopes. The Cryosphere Discussions 6, 2597–2619.

Hanebuth, T., Stattegger, K., Grootes, P. M., 2000. Rapid flooding of the Sunda Shelf: a late-glacial sea-level record. Science 288, 1033–1035.

Hindmarsh, R. C., Le Meur, E., 2001. Dynamical processes involved in the retreat of marine ice sheets. Journal of Glaciology 47, 271–282.

Hjort, C., Ingólfsson, Ó., Möller, P., Lirio, J. M., 1997. Holocene glacial history and sea-level changes on James Ross Island, Antarctic Peninsula. Journal of Quaternary Science 12, 259–273.

Ivins, E. R., James, T. S., 2005. Antarctic glacial isostatic adjustment: a new assessment. Antarctic Science 17, 541–553.

Ivins, E. R., James, T. S., Wahr, J., Schrama, O., Ernst, J., Landerer, F. W., Simon, K. M., 2013. Antarctic contribution to sea level rise observed by GRACE with improved GIA correction. Journal of Geophysical Research: Solid Earth 118, 1–16.

Ivins, E. R., Watkins, M. M., Yuan, D. N., Dietrich, R., Casassa, G., Rülke, A., 2011. Onland ice loss and glacial isostatic adjustment at the Drake Passage: 2003–2009. Journal of Geophysical Research: Oceans 116, B02403.

Jenkins, A., Doake, C. S. M., 1991. Ice-ocean interaction on Ronne Ice Shelf, Antarctica. Journal of Geophysical Research 96, 791.

Johnston, P., 1993. The effect of spatially non-uniform water loads on prediction of sea-level change. Geophysical Journal International 114, 615–634.

Katz, R. F., Worster, M. G., 2010. Stability of ice-sheet grounding lines. Proceedings of the Royal Society A: Mathematical, Physical and Engineering Sciences 466, 1597–1620.

Kaufmann, G., Wu, P., Ivins, E. R., 2005. Lateral viscosity variations beneath Antarctica and their implications on regional rebound motions and seismotectonics. Journal of Geodynamics 39, 165–181.

Keigwin, L. D., Jones, G. A., 2010. Deglacial climatic oscillations in the Gulf of California. Paleoceanography 5, 1009–1023.

Kendall, R. A., Mitrovica, J. X., Milne, G. A., 2005. On post-glacial sea level - II. Numerical formulation and comparative results on spherically symmetric models. Geophysical Journal International 161, 679–706.

Kendall, R. A., Mitrovica, J. X., Milne, G. A., Törnqvist, T. E., Li, Y., 2008. The sea-level fingerprint of the 8.2 ka climate event. Geology 36, 423.

Kennett, J. P., Shackleton, N. J., 1975. Laurentide Ice Sheet Meltwater Recorded in Gulf of Mexico Deep-Sea Cores. Science 188, 147–150.

King, M. A., Bingham, R. J., Moore, P., Whitehouse, P. L., Bentley, M. J., Milne, G. A., 2013. Lower satellite-gravimetry estimates of Antarctic sea-level contribution. Nature 491, 586–589.

Kopp, R. E., Mitrovica, J. X., Griffies, S. M., Yin, J., Hay, C. C., Stouffer, R. J., 2010. The impact of Greenland melt on local sea levels: a partially coupled analysis of dynamic and static equilibrium effects in idealized water-hosing experiments. Climatic Change 103, 619–625.

Lambeck, K., Smither, C., Johnston, P., 1998. Sea-level change, glacial rebound and mantle viscosity fornorthern Europe. Geophysical Journal International 134, 102–144.

Larour, E., Rignot, E., Joughin, I., Aubry, D., 2005. Rheology of the Ronne Ice Shelf, Antarctica, inferred from satellite radar interferometry data using an inverse control method. Geophysical Research Letters 32, L05503.

Latychev, K., Mitrovica, J. X., Tromp, J., Tamisiea, M. E., Komatitsch, D., Christara, C. C., 2005. Glacial isostatic adjustment on 3-D Earth models: a finite-volume formulation. Geophysical Journal International 161, 421–444.

Le Brocq, A. M., Payne, A. J., Vieli, A., 2010. An improved Antarctic dataset for high resolution numerical ice sheet models (ALBMAP v1). Earth System Science Data Discussions 3, 195–230.

Le Meur, E., Huybrechts, P., 1996. A comparison of different ways of dealing with isostasy: examples from modeling the Antarctic ice sheet during the last glacial cycle. Annals of Glaciology, 23, pp 309-317 23, 309–317.

Le Meur, E., Huybrechts, P., 2001. A model computation of the temporal changes of surface gravity and geoidal signal induced by the evolving Greenland ice sheet. Geophysical Journal of the Royal Astronomical Society 145, 835–849.

Lenton, T. M., Held, H., Kriegler, E., Hall, J. W., Lucht, W., Rahmstorf, S., Schellnhuber, H. J., 2008. Tipping elements in the Earth's climate system. Proceedings of the National Academy of Sciences 105, 1786–1793.

Leventer, A., Williams, D. F., Kennett, J. P., 1982. Dynamics of the Laurentide ice sheet during the last deglaciation: evidence from the Gulf of Mexico. Earth and Planetary Science Letters 59, 11–17.

Liu, Z., Otto-Bliesner, B. L., He, F., Brady, E. C., Tomas, R., Clark, P. U., Carlson, A. E., Lynch-Stieglitz, J., Curry, W., Brook, E., Erickson, D., Jacob, R., Kutzbach, J., Cheng, J., 2009. Transient Simulation of Last Deglaciation with a New Mechanism for Bolling-Allerod Warming. Science 325, 310–314.

MacAyeal, D. R., Scambos, T. A., Hulbe, C. L., Fahnestock, M. A., 2003. Catastrophic ice-shelf break-up by an ice-shelf-fragment-capsize mechanism. Journal of Glaciology 49, 22–36.

Martinec, Z., 2000. Spectral–finite element approach to threedimensional viscoelastic relaxation in a spherical earth. Geophysical Journal International 142, 117–141.

Mercer, J. H., 1978. West Antarctic ice sheet and CO2 greenhouse effect: a threat of disaster. Nature 271, 321–325.

Milne, G. A., 1998. Refining models of the glacial isostatic adjustment process. Ph.D. thesis, National Library of Canada.

Milne, G. A., Mitrovica, J. X., 1996. Postglacial sealevel change on a rotating Earth: first results from a gravitationally selfconsistent sealevel equation. Geophysical Journal of the Royal Astronomical Society 126, F13–F20.

Milne, G. A., Mitrovica, J. X., 1998. Postglacial sea-level change on a rotating Earth. Geophysical Journal International 133, 1–19.

Milne, G. A., Mitrovica, J. X., Davis, J. L., 1999. Near-field hydro-isostasy: the implementation of a revised sea-level equation. Geophysical Journal International 139, 464–482.

Mitrovica, J. X., 1996. Haskell [1935] revisited. Journal of Geophysical Research 101, 555.

Mitrovica, J. X., 2003. Recent controversies in predicting post-glacial sea-level change. Quaternary Science Reviews 22, 127–133.

Mitrovica, J. X., Forte, A. M., 2004. A new inference of mantle viscosity based upon joint inversion of convection and glacial isostatic adjustment data. Earth and Planetary Science Letters 225, 177–189.

Mitrovica, J. X., Gomez, N., Morrow, E., Hay, C., Latychev, K., Tamisiea, M. E., 2011. On the robustness of predictions of sea level fingerprints. Geophysical Journal International 187, 729–742.

Mitrovica, J. X., Milne, G. A., 2002. On the origin of late Holocene sea-level highstands within equatorial ocean basins. Quaternary Science Reviews 21, 2179–2190.

Mitrovica, J. X., Milne, G. A., 2003. On postglacial sea level: I. General theory. Geophysical Journal International 154, 253–267.

Mitrovica, J. X., Peltier, W. R., 1991. On postglacial geoid subsidence over the equatorial oceans. Journal of Geophysical Research 96, 20053–20071.

Mitrovica, J. X., Tamisiea, M. E., Davis, J. L., Milne, G. A., 2001. Recent mass balance of polar ice sheets inferred from patterns of global sea-level change. Nature 409, 1026–1029.

Mitrovica, J. X., Wahr, J., Matsuyama, I., Paulson, A., 2005. The rotational stability of an ice-age earth. Geophysical Journal International 161, 491–506.

Morelli, A., Danesi, S., 2004. Seismological imaging of the Antarctic continental lithosphere: a review. Global and Planetary Change 42, 155–165.

Mound, J. E., 1998. True Polar Wander as a Mechanism for Second-Order Sea-Level Variations. Science 279, 534–537.

Naish, T., Powell, R., Levy, R., Wilson, G., Scherer, R., Talarico, F., Krissek, L., Niessen, F., Pompilio, M., Wilson, T., Carter, L., DeConto, R., Huybers, P., McKay, R., Pollard, D., Ross, J., Winter, D., Barrett, P., Browne, G., Cody, R., Cowan, E., Crampton, J., Dunbar, G., Dunbar, N., Florindo, F., Gebhardt, C., Graham, I., Hannah, M., Hansaraj, D., Harwood, D., Helling, D., Henrys, S., Hinnov, L., Kuhn, G., Kyle, P., Läufer, A., Maffioli, P., Magens, D., Mandernack, K., McIntosh, W., Millan, C., Morin, R., Ohneiser, C., Paulsen, T., Persico, D., Raine, I., Reed, J., Riesselman, C., Sagnotti, L., Schmitt, D., Sjunneskog, C., Strong, P., Taviani, M., Vogel, S., Wilch, T., Williams, T., 2009. Obliquity-paced Pliocene West Antarctic ice sheet oscillations. Nature 458, 322–328.

Nakada, M., Lambeck, K., 1989. Late Pleistocene and Holocene sea-level change in the Australian region and mantle rheology. Geophysical Journal International 96, 497–517.

Nakiboglu, S. M., Lambeck, K., 1991. Secular Sea-Level Change. In: Sabadini, R., Lambeck, K., Boschi, E. (Eds.), Glacial Isostasy, Sea Level and Mantle Rheology NATO ASI Series. Springer Netherlands, Dordrecht, pp. 237–258.

Nield, G. A., Whitehouse, P. L., King, M. A., Clarke, P. J., Bentley, M. J., 2012. Increased ice loading in the Antarctic Peninsula since the 1850s and its effect on glacial isostatic adjustment. Geophysical Research Letters 39, L17504.

Oppenheimer, M., 1998. Global warming and the stability of the West Antarctic Ice Sheet. Nature 393, 325–332.

Pattyn, F., Durand, G., 2013. Why marine ice sheet model predictions may diverge in estimating future sea level rise. Geophysical Research Letters 40, 4316–4320.

Pattyn, F., Perichon, L., Durand, G., Favier, L., Gagliardini, O., Hindmarsh, R. C. A., Zwinger, T., Albrecht, T., Cornford, S., Docquier, D., Fürst, J. J., Goldberg, D., Gudmundsson, G. H., Humbert, A., Hütten, M., Huybrechts, P., Jouvet, G., Kleiner, T., Larour, E., Martin, D., Morlighem, M., Payne, A. J., Pollard, D., Rückamp, M., Rybak, O., Seroussi, H., Thoma, M., Wilkens, N., 2013. Grounding-line migration in plan-view marine ice-sheet models: results of the ice2sea MISMIP3d intercomparison. Journal of Glaciology 59, 410–422.

Pattyn, F., Schoof, C., Perichon, L., Hindmarsh, R. C. A., Bueler, E., de Fleurian, B., Durand, G., Gagliardini, O., Gladstone, R., Goldberg, D., Gudmundsson, G. H., Lee, V., Nick, F. M., Payne, A. J., Pollard, D., Rybak, O., Saito, F., Vieli, A., 2012. Results of the Marine Ice Sheet Model Intercomparison Project, MISMIP. The Cryosphere Discussions 6, 267–308.

Peltier, W. R., 1974. The impulse response of a Maxwell Earth. Reviews of Geophysics 12, 649.

Peltier, W. R., 1994. Ice age paleotopography. Science 265, 195–201.

Peltier, W. R., 1998. Postglacial variations in the level of the sea: Implications for climate dynamics and solid-Earth geophysics. Reviews of Geophysics 36, 603.

Peltier, W. R., 2004. Global glacial isostasy and the surface of the ice-age Earth: The ICE-5G (VM2) model and GRACE. Annual Review of Earth and Planetary Sciences 32, 111–149.

Peltier, W. R., 2007. Glacial-Isostatic Adjustment-II. The Inverse Problem. Geophysical Journal of the Royal Astronomical Society 46, 669–705.

Plag, H. P., Juettner, H. U., 2001. Inversion of global tide gauge data for present-day ice load changes. In: Yamanouchi, T. (Ed.), Proceed. Second Int. Symp. on Environmental research in the Arctic and Fifth Ny-Ålesund Scientific Seminar. Memoirs of the National Institute of Polar research, pp. 301–317.

Pollard, D., DeConto, R. M., 2007. A coupled ice-sheet/ice-shelf/sediment model applied to a marine-margin flow line: Frorced and unforced varitations. Glacial Sedimentary Processes and Products, Int. Assoc. of Sedimentol. Spec. Publ. 39, 37–52.

Pollard, D., DeConto, R. M., 2009. Modelling West Antarctic ice sheet growth and collapse through the past five million years. Nature 458, 329–332.

Pollard, D., DeConto, R. M., 2012a. A simple inverse method for the distribution of basal sliding coefficients under ice sheets, applied to Antarctica. The Cryosphere Discussions 6, 1405–1444.

Pollard, D., DeConto, R. M., 2012b. Description of a hybrid ice sheet-shelf model, and application to Antarctica. Geoscientific Model Development 5, 1273–1295.

Raymo, M. E., Mitrovica, J. X., 2012. Collapse of polar ice sheets during the stage 11 interglacial. Nature 483, 453–456.

Rignot, E., 2002. Rapid Bottom Melting Widespread near Antarctic Ice Sheet Grounding Lines. Science 296, 2020–2023.

Rignot, E., 2006. Changes in ice dynamics and mass balance of the Antarctic ice sheet. Philosophical Transactions of the Royal Society A: Mathematical, Physical and Engineering Sciences 364, 1637–1655.

Roberts, S. J., Hodgson, D. A., Sterken, M., Whitehouse, P. L., Verleyen, E., Vyverman, W., Sabbe, K., Balbo, A., Bentley, M. J., Moreton, S. G., 2011. Geological constraints on glacio-isostatic adjustment models of relative sea-level change during deglaciation of Prince Gustav Channel, Antarctic Peninsula. Quaternary Science Reviews 30, 3603–3617.

Scambos, T. A., Bohlander, J. A., Shuman, C. A., Skvarca, P., 2004. Glacier acceleration and thinning after ice shelf collapse in the Larsen B embayment, Antarctica. Geophysical Research Letters 31, L18402.

Schoof, C., 2007a. Ice sheet grounding line dynamics: Steady states, stability, and hysteresis. Journal of Geophysical Research 112, F03S28.

Schoof, C., 2007b. Marine ice-sheet dynamics. Part 1. The case of rapid sliding. Journal of Fluid Mechanics 573, 27.

Shepherd, A., 2001. Inland Thinning of Pine Island Glacier, West Antarctica. Science 291, 862–864.

Shepherd, A., Ivins, E. R., A, G., Barletta, V. R., Bentley, M. J., Bettadpur, S., Briggs, K. H., Bromwich, D. H., Forsberg, R., Galin, N., Horwath, M., Jacobs, S., Joughin, I., King, M. A., Lenaerts, J. T. M., Li, J., Ligtenberg, S. R. M., Luckman, A., Luthcke, S. B., McMillan, M., Meister, R., Milne, G., Mouginot, J., Muir, A., Nicolas, J. P., Paden, J., Payne, A. J., Pritchard, H., Rignot, E., Rott, H., Sorensen, L. S., Scambos, T. A., Scheuchl, B., Schrama, E. J. O., Smith, B., Sundal, A. V., van Angelen, J. H., van de Berg, W. J., Van den Broeke, M. R., Vaughan, D. G., Velicogna, I., Wahr, J., Whitehouse, P. L., Wingham, D. J., Yi, D., Young, D., Zwally, H. J., 2012. A Reconciled Estimate of Ice-Sheet Mass Balance. Science 338, 1183–1189.

Simon, K. M., James, T. S., Ivins, E. R., 2010. Ocean loading effects on the prediction of Antarctic glacial isostatic uplift and gravity rates. Journal of Geodesy 84, 305–317.

Smith, J. B., Schneider, S. H., Oppenheimer, M., Yohe, G. W., Hare, W., Mastrandrea, M. D., Patwardhan, A., Burton, I., Corfee-Morlot, J., Magadza, C. H., 2009. Assessing dangerous climate change through an update of the Intergovernmental Panel on Climate Change (IPCC) "reasons for concern". Proceedings of the National Academy of Sciences 106, 4133–4137.

Solomon, S., Quin, D., Manning, M., Chen, Z., Marquis, M., Averyt, K. B., Tignor, M., Miller, H. L. (Eds.), 2007. Climate change 2007-the physical science basis: Working group I contribution to the fourth assessment report of the IPCC. Cambridge University Press, Geneva.

Stocchi, P., Escutia, C., Houben, A. J. P., Vermeersen, B. L. A., Bijl, P. K., Brinkhuis, H., DeConto, R. M., Galeotti, S., Passchier, S., Pollard, D., Brinkhuis, H., Escutia, C., Klaus, A., Fehr, A., Williams, T., Bendle, J. A. P., Bijl, P. K., Bohaty, S. M., Carr, S. A., Dunbar, R. B., Flores, J. A., Gonzàlez, J. J., Hayden, T. G., Iwai, M., Jimenez-Espejo, F. J., Katsuki, K., Kong, G. S., McKay, R. M., Nakai, M., Olney, M. P., Passchier, S., Pekar, S. F., Pross, J., Riesselman, C., Röhl, U., Sakai, T., Shrivastava, P. K., Stickley, C. E., Sugisaki, S., Tauxe, L., Tuo, S., van de

Flierdt, T., Welsh, K., Yamane, M., 2013. Relative sea-level rise around East Antarctica during Oligocene glaciation. Nature Geoscience 6, 380–384.

Tamisiea, M. E., 2011. Ongoing glacial isostatic contributions to observations of sea level change. Geophysical Journal International 186, 1036–1044.

Tamisiea, M. E., Mitrovica, J. X., Milne, G. A., Davis, J. L., 2001. Global geoid and sea level changes due to presentday ice mass fluctuations. Journal of Geophysical Research: Oceans 106, 30849–30863.

Thomas, I. D., King, M. A., Bentley, M. J., Whitehouse, P. L., Penna, N. T., Williams, S. D., Riva, R. E., Lavallee, D. A., Clarke, P. J., King, E. C., 2011. Widespread low rates of Antarctic glacial isostatic adjustment revealed by GPS observations. Geophysical Research Letters 38, L22302.

Thomas, R., 2004. Accelerated Sea-Level Rise from West Antarctica. Science 306, 255–258.

Thomas, R., Bentley, C. R., 1978. A model for Holocene retreat of the West Antarctic Ice Sheet. Quaternary Research 10, 150–170.

Törnqvist, T. E., Hijma, M. P., 2012. Links between early Holocene ice-sheet decay, sea-level rise and abrupt climate change. Nature Geoscience 5, 601–606.

van de Berg, W. J., Van den Broeke, M. R., Reijmer, C. H., van Meijgaard, E., 2006. Reassessment of the Antarctic surface mass balance using calibrated output of a regional atmospheric climate model. Journal of Geophysical Research: Oceans 111, D11104.

van den Berg, J., van de Wal, R. S. W., Milne, G. A., Oerlemans, J., 2008. Effect of isostasy on dynamical ice sheet modeling: A case study for Eurasia. Journal of Geophysical Research 113, B05412.

Vaughan, D. G., 2008. West Antarctic ice sheet collapse–the fall and rise of a paradigm. Climatic Change 91, 65–79.

Velicogna, I., 2006. Measurements of Time-Variable Gravity Show Mass Loss in Antarctica. Science 311, 1754–1756.

Weaver, A. J., 2003. Meltwater Pulse 1A from Antarctica as a Trigger of the Bolling-Allerod Warm Interval. Science 299, 1709–1713.

Weertman, J., 1974. Stability of the junction of an ice sheet and an ice shelf. Journal of Glaciology 13, 3–11.

Whitehouse, P. L., Bentley, M. J., Le Brocq, A. M., 2012a. Quaternary Science Reviews. Quaternary Science Reviews 32, 1–24.

Whitehouse, P. L., Bentley, M. J., Milne, G. A., King, M. A., Thomas, I. D., 2012b. A new glacial isostatic adjustment model for Antarctica: calibrated and tested using observations of relative sea-level change and present-day uplift rates. Geophysical Journal International 190, 1464–1482.

Wilchinsky, A. V., 2009. Linear stability analysis of an ice sheet interacting with the ocean. Journal of Glaciology 55, 13–20.

Wingham, D. J., Wallis, D. W., Shepherd, A., 2009. Spatial and temporal evolution of Pine Island Glacier thinning, 1995–2006. Geophysical Research Letters 36, L17501.

Woodward, R. S., 1888. On the form and position of mean sea level. United States Geological Survey Bulletin 48, 87–170.

Wu, P., van der Wal, W., 2003. Postglacial sealevels on a spherical, self-gravitating viscoelastic earth: effects of lateral viscosity variations in the upper mantle on the inference of viscosity contrasts in the lower mantle. Earth and Planetary Science Letters 211, 57–68.

Zhong, S., Paulson, A., Wahr, J., 2003. Three-dimensional finite-element modelling of Earth's viscoelastic deformation: effects of lateral variations in lithospheric thickness. Geophysical Journal International 155, 679–695.